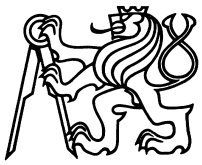

Czech Technical University in Prague
Faculty of Nuclear Sciences and Physical Engineering

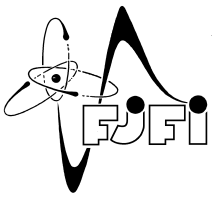

Morphic effect and anisotropic magnetoelectric coupling in $EuTiO_3$

Morfický efekt a anizotropní magnetoelektrická vazba v $EuTiO_3$

Master's Degree Project

Author: **Bc. Dalibor Repček**

Supervisor: **RNDr. Stanislav Kamba, CSc.**

Consultant: **Mgr. Filip Kadlec, Dr., RNDr. Jan Prokleška, Ph.D.**

Language advisor: **RNDr. Stanislav Kamba, CSc.**

Academic year: 2018/2019

ČESKÉ VYSOKÉ UČENÍ TECHNICKÉ V PRAZE
FAKULTA JADERNÁ A FYZIKÁLNĚ INŽENÝRSKÁ
Katedra inženýrství pevných látek

ZADÁNÍ DIPLOMOVÉ PRÁCE

Student: **Bc. Dalibor Repček**

Studijní program: **Aplikace přírodních věd**

Obor: **Inženýrství pevných látek**

Akademický rok: **2018/2019**

Název práce: (česky) **Morfický efekt a anizotropní magnetoelektrická vazba v $EuTiO_3$**

Název práce: (anglicky) **Morphic effect and anisotropic magnetoelectric coupling in $EuTiO_3$**

Pokyny pro vypracování:

Diplomová práce je zaměřena na studium dielektrické anizotropie vyvolané vnějším magnetickým polem v incipientně feroelektrickém antiferomagnetu $EuTiO_3$. Tento materiál vykazuje pod Néelovou teplotou (T_N = 5,3 K) 7% změnu dielektrické permitivity s magnetickým polem. Tato změna by měla být závislá na směru magnetického pole a právě tuto anizotropii budeme studovat. Dielektrická měření provedeme při frekvencích 1 Hz až 100 kHz při teplotách 0,3 K až 300 K a při magnetických polích do 10 T (kolmo a paralelně s vnějším elektrickým polem). Dále provedeme měření anizotropní magnetostrikce při polích do 7 T a teplotách do 2 K. Měření budou doplněna infračervenými spektry fononů při nízkých teplotách a terahertzovým měřením do 2 K s magnetickým polem do 7 T. Z naměřených dat bychom měli určit složky tenzoru spinové korelační funkce, závislost feromagnetické rezonance na magnetickém poli a parametry měkkého fononu rozštěpeného v magnetickém poli. Experimenty budou realizovány na zařízení PPMS ve společné magnetické laboratoři Fyzikálního ústavu a MFF UK. THz a infračervená měření budou provedena ve Fyzikálním ústavu.

Při řešení postupujte podle následujících bodů.

I. Rešeršní/teoretická část
   1) Multiferoika a typy magnetoelektrických vazeb
   2) Rešerše publikované literatury o $EuTiO_3$
   3) Experimentální metody: Kapacitní dilatometrie, magnetoelektrická měření, radiofrekvenční, terahertzová a infračervená spektroskopie.
   4) Metodika zpracování dat

II. Experimentální část
    1) Popis experimentálního zařízení
    2) Realizace experimentů, popis vzorků
    3) Zpracování dat
    4) Výsledky a jejich diskuze

Doporučená literatura:

[1] S. Dong, J.-M. Liu, S.-W. Cheong, and Z. Ren: Adv. Phys. **64** (2015) 519-626.
[2] S. Skiadopoulou: Spin and Lattice Excitations in Multiferroics, Disertační práce, FZÚ AV ČR a MFF UK v Praze, 2017.
[3] P. G. Reuvekamp, R. K. Kremer, J. Köhler, and A. Bussmann-Holder: Phys. Rev. B **90** (2014) 094420.
[4] K. Rubi and R. Mahendiran: Europhysics Lett. **118** (2017) 57008.
[5] A. Bussmann-Holder and J. Köhler: Journal of Physics and Chemistry of Solids **84** (2015) 2-12.
[6] J. Schiemer, L. J. Spalek, S. S. Saxena, C. Panagopoulos, T. Katsufuji, A. Bussmann-Holder, J. Köhler, and M. A. Carpenter: Phys. Rev. B **93** (2016) 054108.

Jméno a pracoviště vedoucího práce:
RNDr. Stanislav Kamba, CSc., Fyzikální ústav AV ČR, Praha

Jméno a pracoviště konzultanta:
Mgr. Filip Kadlec, Dr., Fyzikální ústav AV ČR, Praha
RNDr. Jan Prokleška, Ph.D., Matematicko-fyzikální fakulta UK, Praha

Datum zadání diplomové práce: 19. 10. 2018

Termín odevzdání diplomové práce: 6. 5. 2019

Doba platnosti zadání je dva roky od data zadání.

…… ……..
vedoucí katedry *děkan*

V Praze dne 19. 10. 2018

Acknowledgment:

I would like to show my greatest appreciation to my supervisor RNDr. Stanislav Kamba, CSc. for his thoroughness, willingness, helpfulness, patience and for providing a quality professional environment and at the same time creation of friendly working atmosphere. Also I would like to express my gratitude to my consultant Mgr. Filip Kadlec, Dr. as well as to his wife Ing. Christelle Kadlec, Dr. for their professional surveillance, great patience, helpfulness and and always positive and fiendly attitude. I want to thank Ing. Martin Kachlík, Ph.D. for the preparation of the $EuTiO_3$ ceramics and subsequently to all who somehow participated on the experimental part of this Thesis, namely to Mgr. Maxim Savinov, Ph.D., Veronica Goian, MSc., RNDr. Jan Prokleška, PhD., Mgr. Petr Proschek, Ing. Jan Drahokoupil, Ph.D. and Mgr. Fedir Borodavka, Ph.D.

Then my deepest appreciation goes to my parents for continual support of my education and growth. Special thanks also to other members of my close and wide family, who functioned as a solid moral support. I would like to thank all pedagogues and people from Department of solid state engineering of FNSPE, who contributed to my education and commented my research effort and thereby helped to improve this work. Finally, I owe a very important debt to my closest friends, who provided me by optimism and were pushing me to completion of this thesis.

Author's declaration:

I declare that this Master's Degree Project is entirely my own work and I have listed all the used sources in the bibliography.

Prague, May 6, 2019 Dalibor Repček

Název práce:

Morfický efekt a anizotropní magnetoelektrická vazba v $EuTiO_3$

Autor: Dalibor Repček

Obor: Inženýrství pevných látek

Druh práce: Diplomová práce

Vedoucí práce: RNDr. Stanislav Kamba, CSc., Fyzikální ústav AV ČR

Konzultant: Mgr. Filip Kadlec, Dr., Fyzikální ústav AV ČR,
RNDr. Jan Prokleška, Ph.D., Matematicko-fyzikální fakulta UK

Abstrakt: $EuTiO_3$ je incipientně feroelektrický antiferomagnet (pod T_N = 5.3 K), který se vyznačuje silnou magnetoelektrickou vazbou projevující se závislostí permitivity na vnějším magnetickém poli. Práce zkoumá anizotropii magnetoelektrické vazby $EuTiO_3$ keramik vzhledem k vzájemné orientaci elektrického a magnetického pole. Permitivita keramik je spektroskopicky zkoumána v radiofrekvenčním, terahertzovém (THz) a infračerveném oboru. Keramiky jsou též podrobeny dilatometrickým a magnetizačním měřením. Vzorky jsou za nízkých teplot (až 0.3 K) vystaveny silnému magnetickému poli (až do 15 T) orientovanému kolmo či paralelně k poli elektrickému. Práce vysvětluje anizotropii permitivity skrze morfické jevy, magnetostrikci a demagnetizační pole vzorků a porovnává předpovědi s naměřenými daty. Příčinou zdánlivé anizotropie permitivity ve slabém magnetickém poli je nakonec demagnetizační pole keramik. Anizotropie THz indexu lomu je způsobena feromagnetickou rezonancí v subTHz oblasti.

Klíčová slova: demagnetizační pole, dielektrická spektroskopie, $EuTiO_3$, fonony, infračervená spektroskopie, magnetoelektrická vazba, multiferoika, radiofrekvenční a terahertzová spektroskopie

Title:

Morphic effect and anisotropic magnetoelectric coupling in $EuTiO_3$

Author: Dalibor Repček

Abstract: $EuTiO_3$ is an incipient ferroelectric antiferromagnet (below T_N = 5.3 K), exhibiting a strong magnetoelectric coupling, characterised by the dependence of permittivity on an external magnetic field. This Thesis aims to examine the $EuTiO_3$ ceramics magnetoelectric-coupling anisotropy with respect to the mutual orienation of the electric and magnetic field. The ceramics are studied spectroscopically in a radio-frequency, terahertz, and infrared region. Moreover, the dilatometric and magnetization measurements are conducted. The samples are subjected to low temperatures down to 0.3 K and magnetic field of up to 15 T, oriented parallelly or perpendicularly to the electric field. The permittivity anisotropy is disccused in terms of the morphic effects, magnetostriction, and the demagnetizing field of the samples. The predictions are compared with the experimental data. The demagnetizing field is found to be the cause of the seeming $EuTiO_3$ permittivity anisotropy in a weak magnetic field. The THz refractive index anisotropy is induced by a ferromagnetic resonance in the subTHz region.

Key words: demagnetizing field, dielectric spectroscopy, $EuTiO_3$, infrared spectroscopy, magnetoelectric coupling, multiferroics, phonons, radio-frequency and terahertz spectroscopy

Contents

Introduction

Materials with internal electric or magnetic ordering, i.e. ferroelectrics, antiferroelectrics, ferromagnetics, antiferromagnets and ferrimagnetics, have always been of great interest in the field of material research, for example due to their non-linear behavior in the outer field or due to the unusually high value of electric or magnetic susceptibility around the temperature of the phase transition from disordered to ordered state. The question of the existence of a substance, that is characterized by electric and magnetic order at the same time, was answered positively at the end of the 1950's. First perovskite materials with this property were then examined. These materials were designated as multiferroics only at the beginning of 1990s by Hans Schmidt. [1] However, early enthusiasm in the field of multiferroics slowly passed away, mainly due to the only small number of multiferroic materials that were known, weak magnetoelectric coupling and also due to insufficiently developed experimental techniques for investigating these materials. At turn of the millennium, the interest in multifferoics has risen again with the discovery of new groups of multiferroic materials with strong magnetoelectric coupling and with the considerable improvement of measuring techniques, mainly those spectroscopic. [2]

Since both the electric and the magnetic arrangement exist in multiferrorics at the same time, a certain degree of interconnection and dependence can be expected between their electric and magnetic properties. Such a connection of electric and magnetic properties is called a magnetoelectric coupling. The stronger the magnetoelectric coupling, the more interesting material is from the application point of view. The possibility of influencing the magnetic order by an electric field could be advantageously used, for example, for reading and writing the bits in magnetic memories. The implementation of the multiferroics into these memories would allow the use of small voltage pulses instead of the relatively strong electric currents generating magnetic field, which would lead to a reduction in energy consumption and acceleration of both the writing and reading of the magnetic bits. Moreover, the conversion of purely magnetic memory with two-state bits into multiferroic memory with four-state bits would enable the increase of contemporary computer storage capacities. [2]

Except for the multiferroics, there are other materials that are characterized by a strong magnetoelectric coupling. One such a material is titanium-europium oxide ($EuTiO_3$). This material is not multiferroic. Although it is antiferromagnetic below the Néel temperature $T_N \sim 5$ K, the ferroelectric arrangement does not occur. Quantum fluctuations at low temperatures suppress the formation of the ferroelectric phase to such an extent that the temperature of the ferroelectric phase transition seems to be (hypothetically) negative. Such materials are called incipient ferroelectrics. However, $EuTiO_3$ is interesting just for its strong magnetoelectric coupling. This coupling is observed through the dependence of permittivity (substance response to the applied electric field) on the external magnetic field, specifically under and close above T_N. [3] More detail studies of magnetoelectric coupling i.e. changes of magnetization by electric field were investigated in the $EuTiO_3$ by Shvartsman et al. [4]

This Master's Degree Project is focused on possible anisotropic character of permittivity of $EuTiO_3$ ceramics in radio- and THz-frequency region with respect to mutual orientation of the electric and magnetic field. We try to capture this anisotropic magnetoelectric coupling experimentally and then to explain it based on the obtained data and several possible theoretical concepts. We operate with explanations built on the magnetostriction of a sample [5], the morphic effect [6]-[10] and the effect of the demagnetizing field of the sample itself.

The samples were subjected to spectroscopic measurements in the radio-frequency, terahertz and infrared region. Furthermore, the magnetization of the samples was measured and attempts were made to measure the magnetostriction. The radio-frequency measurements were performed in the frequency range 1 Hz-1 MHz, temperature range $0.3 - 297$ K and in the external homogeneous magnetic field up to 15 T, which was oriented perpendicular or parallel to the electric field. In the terahertz and infrared region, experiments were performed within the temperature interval $2 - 300$ K and $7 - 300$ K, respectively. In addition, terahertz experiments were realized in external homogeneous magnetic field up to 7 T. This field was also applied in two significant directions, either parallel or perpendicular to the electric component of the linearly polarized terahertz pulse. Magnetization and magnetostrictive measurements were performed in a commercially available Quantum Design Physical Property Measurement System (PPMS) that allowed the application of the homogeneous magnetic field up to 9 T in temperature range $2 - 297$ K. Magnetodielectric measurements were performed down to 0.3 K in magnetic field up to 15 T in 20 T magnet from Cryogenics company. The experimental part of the thesis was accompanied by difficulties with the quality of $EuTiO_3$ ceramics, especially with their enhanced conductivity. These difficulties were eventually significantly suppressed. Spectroscopic experiments were performed in the Institute of Physics of the CAS. Magnetodielectric, magnetostrictive and magnetization measurements were realized in a joint magnetic laboratory of the Institute of Physics and of the Faculty of Mathematics and Physics of the Charles University.

Finally, I would like to point out that the topic of this thesis is directly linked to my Bachelor's Degree Project. [11] This Master's Degree Project deepens the insight into the theoretical and experimental aspects of the subject, which was already partly included in the Bachelor's Degree Project. Therefore some subchapters are directly based on the sections of the previous thesis and are appropriately extended and modified.

Chapter 1

Theoretical background

1.1 Multiferroics

The term "ferroic" in the word multiferroic historically refers to the prefix "ferro-" in ferromagnetics. These materials are characterized by the parallel arrangement of the equivalent magnetic moments of the particles over a long distance, in other words, parallel orientation of these moments in the region of the macroscopic dimensions (so-called Weiss domains). The consequence is the existence of a non-zero magnetization vector $\boldsymbol{M}$ (within one Weiss domain) in the zero outer magnetic field $\boldsymbol{H}$. Then we talk about the spontaneous magnetization $\boldsymbol{M}^S$ in the direction of easy magnetizing axis of the substance. [12] The prefix "ferro-" was later used in analogy for so-called ferroelectrics, characterized by a long-distance parallel arrangement of electric dipole moments (and thus the existence of a non-zero spontaneous polarization vector $\boldsymbol{P}^S$), as well as for ferroelastic substances with spontaneous deformation $\overleftrightarrow{\kappa}^S$ (second order tensor quantity). It is worth noting the existence of the fourth ferrous arrangement in the so-called ferrotoroidic materials. These are substances with a spontaneous toroidal moment $\boldsymbol{T}^S$, which can be derived from the multipole expansion of the electrodynamic vector potential $\boldsymbol{A}(\boldsymbol{r})$. A typical example of a system possesing the non-zero toroidal moment is a magnetic vortex (an arrangement of spins breaking both spatial and time inversion) with a moment $\boldsymbol{T} = \sum_{\boldsymbol{i}} \boldsymbol{r_i} \times \boldsymbol{S_i}$, where $\boldsymbol{r_i}$ denotes the position of the i-th spin $\boldsymbol{S_i}$. [2], [13]

Ferroic materials are distinguishable through the characteristic dependence of the order parameter (i-th component of the magnetization M_i, i-th component of the electric polarization P_i, ij-th element of the deformation tensor κ_{ij}) on the corresponding outer field (i-th component of the magnetic field strength H_i, i-th component of the electric field strength E_i, ij-th element of the mechanical stress σ_{ij}). These curves are called hysteresis loops. The shape of the hysteresis loop is shown in Fig. 1.1. Together with the hysteresis loop, this figure shows the physical basis of the curve shape. Basically, hysteresis behaviour of all ferroics can be explained through a well-known model of changes in domain structure, which was originally invented for the ferromagnets during the magnetization process (further reading [12]).

Multiferroics, as we understand them according to the definition of H. Schmid from 1994, are those materials that are characterized by at least two different ferroic arrangements at the same time in one phase. [1] Although we can call multiferroic all substances with an arbitrary combination of ferroic arrangements, most often we refer to multiferroic materials in connection with the coexistence of electric and magnetic ferroic (in a more general sense, ferro-, ferri- and antiferro-) arrangements. This is because multiferroics with electric and magnetic arrangement can be very promising materials for application

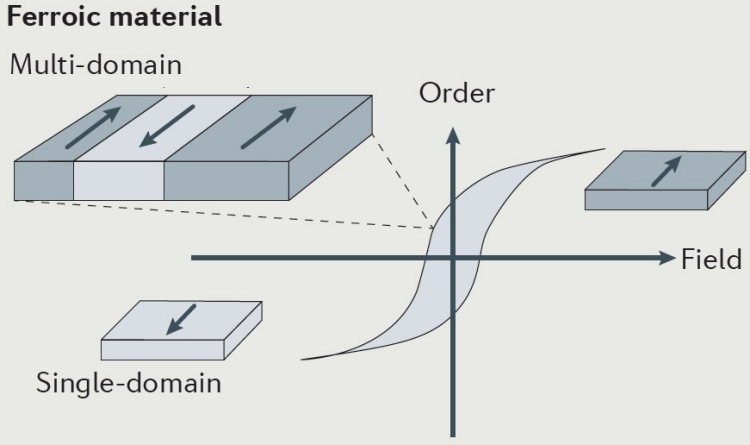

Figure 1.1: Shape of the hysteresis loop, which describes the dependence of the order parameter M_i, P_i, κ_{ij} on the corresponding field H_i, P_i, σ_{ij} for ferroic materials. In weak fields, the samples are in the poly-domain state, and in strong fields, the sample becomes a single-domain and therefore there is a saturation of the order parameter. (figure taken from [2])

and therefore are the most commonly studied materials. Without deeper insight into the issue, it is obvious that the order parameters are firmly bound to the properties of the crystal lattice, and therefore it is to be expected that the application of the external field will not only affect the order parameter corresponding to the applied field, but also more or less the other order parameters present in the material. This interdependence of different fields and order parameters is illustrated in Fig. 1.2. Such a cross-action between electric and magnetic fields and their order parameters (magnetization and polarization) is called *magnetoelectric coupling*, and the multiferroic material, in which the coupling exists, is called *magnetoelectric multiferroic*. [2]

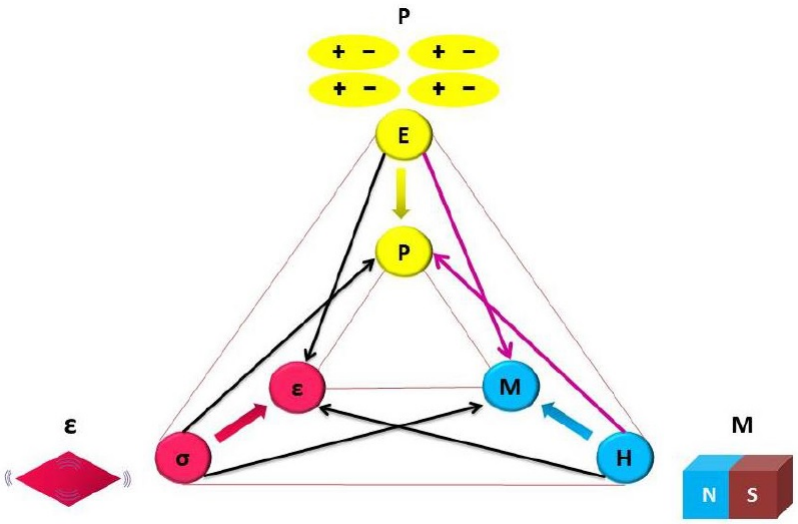

Figure 1.2: Schematic representation of the interconnection between the order parameters and the applied fields in multiferroics. (figure taken from [14])

Application of the magnetoelectric multiferroics is obvious. Their use can be expected wherever we need to influence the magnetic properties of substance by an electric field. Typically, it is in magnetic memory, where it would be possible to write and read magnetic bits using small electric potential pulses when using multiferoic memory disc. Nowadays, magnetic memory is controlled either by an external magnetic field (hard disk heads that are relatively slow) or by strong current pulses that generate a magnetic field. The second method is used in magnetic RAM memories, but these memories can not be miniaturized anymore, because they are heavily heated through Joule's heat due to electric resistance. By using the multiferroic components, the energy demands of the memories would significantly decrease and at the same time their operating frequencies would be significantly improved, as the relatively long preparing time of the recording or reading currents would be shortened. Computer memory could be improved by using multiferoics also from a different point of view, namely by extending the two-state magnetic bits to the four-state electromagnetic bits. [15] In the recent years, research of the multiferroic thin films, oxide heterostructures or also ferromagnetic domain walls that produce spontaneous polarization [16] and behave as multiferroics (although the material is not multiferroic in the bulk), significantly expanded. So the group of multiferroic materials was strongly broadened. [2]

1.1.1 Classification of multiferroics

In the first approximation, multiferroics can be divided into two groups or categories. The major difference between *type-I* and *type-II* multiferroics is hidden in the interconnection between the electric and the magnetic arrangement. [17] In type-I materials, the critical temperatures of both phase transitions may differ significantly (the phase transition temperature to the ferroelectric phase is usually higher than the critical temperature for the magnetic arrangement), and both types of arrangements are almost independent of each other. In type-II multiferroics, ferroelectricity is induced by a particular magnetic arrangement, and therefore both phase transitions are very close to each other or identical. [2], [13]

Type-I multiferroics are interesting for their high value of electric polarization and high critical temperatures (sometimes above the room temperature). Unfortunately, they are also known for their weak magnetoelectric coupling, which is directly related to the different critical temperatures of transitions to the states of electric and magnetic ordering. According to the formation mechanism of the ferroelectric phase, the type-I multiferroics are subdivided into four classes. 1) The ferroelectric arrangement in ABO_3 *perovskites* may be caused by the displacement of a central ion B with an empty *d*-shell out of the original center of symmetry, 2) may emerge due to the so-called *lone-pair* mechanism (Fig. 1.3-**a**), in which the A-ion (e.g. Bi or Pb) *s* electrons, which does not participate in the bonds with the surrounding atoms, are directionally ejected, or 3) may be caused by the so-called *charge-ordering* mechanism (Fig. 1.3-**c**), which occurs due to the presence of two charge-non-equivalent sublattices (e.g. Fe^{2+} ions in one sublattice, Fe^{3+} in the other), or 4) may appear *geometric ferroelectricity* mechanism (Fig. 1.3-**b**) as a result of the oxygen polyhedra tilting leading to changes in bond lengths and thus to the displacement of certain ions from their original equilibrium positions. [17]

Type-II multiferroics are characterized by direct induction of ferroelectric order through a magnetic arrangement. Therefore, these substances generally show a higher degree of magnetoelectric coupling than type-I. However, the absolute value of such spin-induced (spontaneous) electric polarization is generally from two to three orders of magnitude lower than the absolute value of spontaneous electric polarization in type-I multiferroics. Naturally, the phase transition temperatures of both arrangements in these materials are closer to each other than in type-I substances, and at the same time the transition temperature to the ferroelectric phase must be less than or equal to the transition temperature to the magnetic phase. The often disadvantage of these materials is the low temperature required for achieving

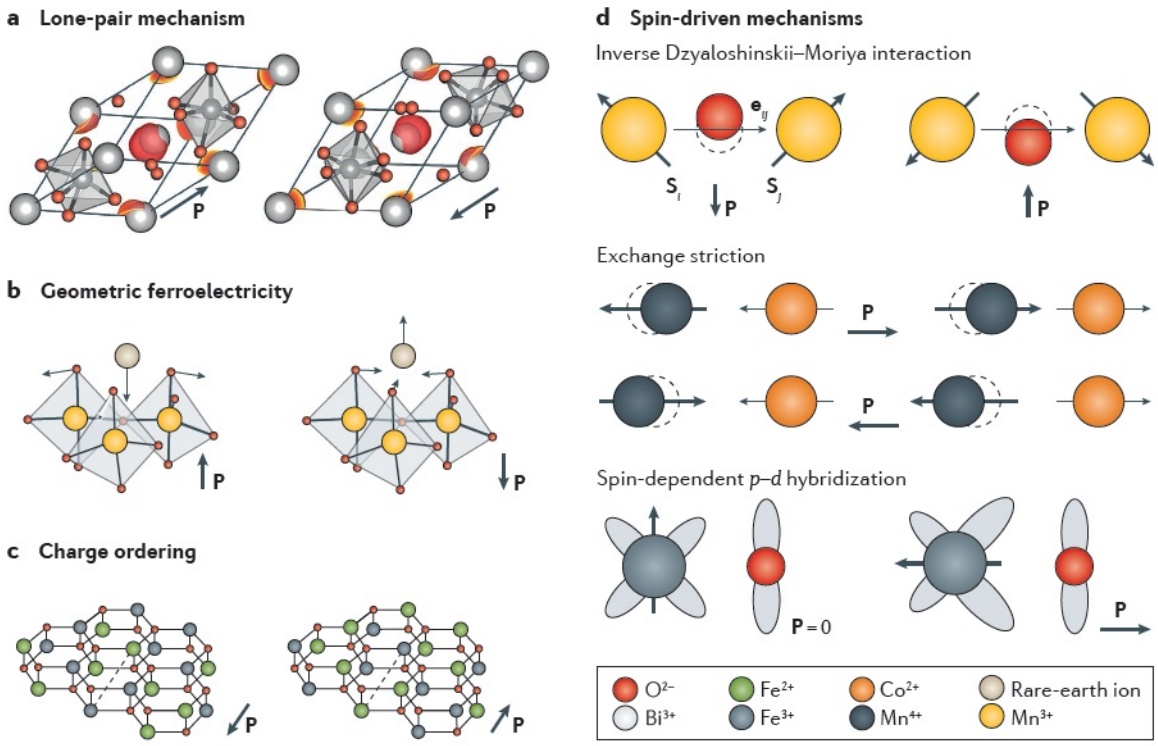

Figure 1.3: **Mechanisms leading to ferroelectricity: a** *Lone-pair* ferroelectricity in $BiFeO_3$. The two Bi^{3+} electrons shift towards the FeO_6 octahedra. **b** *Geometrically driven* ferroelectricity in hexagonal (h-)$RMnO_3$ emerges from a tilt and deformation of MnO_5 bipyramids, which displace the rare-earth ions R. **c** *Charge ordering* in $LuFe_2O_3$ creates alternating layers with Fe^{2+}/Fe^{3+} ratios of 2 : 1 and 1 : 2. This leads to a spontaneous polarization between the two layers. **d** Mechanisms of *spin-driven* ferroelectricity **upper:** *Inverse Dzyaloshinskii-Moriya interaction* causing a non-magnetic ion displacement as a consequence of relativistic correction of the super-exchange effect. $\boldsymbol{P} \propto \boldsymbol{e}_{ij} \times (\boldsymbol{S}_i \times \boldsymbol{S}_j)$ **middle:** *Exchange striction* causing a magnetic ion translation. $\boldsymbol{P} \propto \boldsymbol{R}_{ij} \cdot (\boldsymbol{S}_i \cdot \boldsymbol{S}_j)$ **bottom:** *Spin-dependent p-d hybridization*, i.e. spin-dependent electron hybridization between metal atoms and the ligand. $\boldsymbol{P} \propto (\boldsymbol{S}_i \cdot \boldsymbol{e}_{ij})^2 \cdot \boldsymbol{e}_{ij}$ (figure taken from [2])

the magnetic phase transition. Type-II multiferroics can be subdivided into two subgroups, *spiral* and *collinear* type-II multiferroics, according to the spin configuration (which is the basis for spontaneous polarization). In the case of spiral structures, the spontaneous polarization emerges as a consequence of a *spin-orbital coupling*, namely *inverse Dzyaloshinskii-Moriya interaction* (based on relativistic correction of the super-exchange effect) and spin-dependent electron hybridization between metal atom and the ligand (also called *spin-dependent p-d hybridization*). Inverse Dzyaloshinskii-Moriya interaction is based on non-magnetic ion displacement from originally 180° bond between the magnetic ions. The displacement has roots in relativistic correction of super-exchange effect, therefore the induced polarization P fulfills $\boldsymbol{P} \propto \boldsymbol{e}_{ij} \times (\boldsymbol{S}_i \times \boldsymbol{S}_j)$, where $\boldsymbol{S}_i$, $\boldsymbol{S}_j$ are neighbouring spins and $\boldsymbol{e}_{ij}$ is the directional unit vector connecting both spins. The induced polarization emerging as a consequence of the spin-dependent p-d hybridization is then governed by formula $\boldsymbol{P} \propto (\boldsymbol{S}_i \cdot \boldsymbol{e}_{ij})^2 \cdot \boldsymbol{e}_{ij}$, in which $\boldsymbol{S}_i$ marks the metal ion spin and $\boldsymbol{e}_{ij}$ denotes the unit vector defining the direction of the chemical bond. In the case of collinear structures, *spin-lattice coupling*, such as *exchange striction* (based on unequal interaction between parallel and antiparallel magnetic moments and consequent displacement of the magnetic ions), prevails. This

mechanism induces a polarization, which is proportional to $\boldsymbol{P} \propto \boldsymbol{R}_{ij} \cdot (\boldsymbol{S}_i \cdot \boldsymbol{S}_j)$. Here $\boldsymbol{R}_{ij}$ is the directional vector of an ion displacement and $\boldsymbol{S}_i$, $\boldsymbol{S}_j$ are neighbouring spins. All three mechanisms are shown in Fig. 1.3-**d**. [2], [13]

1.1.2 Magnetoelectric coupling

The term *magnetoelectric coupling*, which is already intuitively understood as a link between the magnetic and electric properties of the material, is closely related to multiferroic materials. However, it is worth pointing out that the existence of a magnetoelectric coupling is not in equivalence with the existence of the multiferroic arrangement in the material. However, in practice, all multiferroic materials are characterized by magnetoelectric coupling of a certain strength. From a historical point of view, it has always been an aim to search for such multiferroic materials that would exhibit the strongest magnetoelectric coupling. Study of this coupling is thus motivated by the study of multiferroic materials. [2] From the qualitative point of view, the ideal magnetoelectric coupling in multiferroic materials with ferroelectric and ferromagnetic order exhibits a hysteresis behaviour in the dependencies of $\boldsymbol{P}$ on $\boldsymbol{H}$ and $\boldsymbol{M}$ on $\boldsymbol{E}$ (see Fig. 1.4).

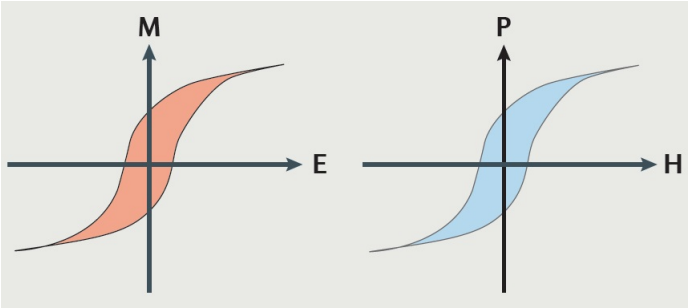

Figure 1.4: Hysteresis dependencies of the magnetization and polarization on the electric and magnetic field respectively. This behavior is a feature of multiferroic materials with an ideal magnetoelectric coupling. (figure taken from [2])

Based on the Landau phenomenological theory of phase transitions, several first terms of the free-energy density of the magnetoelectric multiferroic can be put into form [18]

$$F(\boldsymbol{E},\boldsymbol{H}) = F_0 - P_i^S E_i - M_i^S H_i - \frac{\varepsilon_0 \varepsilon_{ij}}{2} E_i E_j - \frac{\mu_0 \mu_{ij}}{2} H_i H_j - \alpha_{ij} E_i H_j - \frac{\beta_{ijk}}{2} E_i H_j H_k - \frac{\gamma_{ijk}}{2} E_i E_j H_k - \frac{\delta_{ijkl}}{2} E_i E_j H_k H_l, \tag{1.1}$$

where F_0 denotes the density of free energy, which is independent of the electric and magnetic field, P_i^S and M_i^S are i-th components of spontaneous polarization and magnetization, ε_0 and μ_0 mark the permittivity and permeability of vacuum, ε_{ij} and μ_{ij} are the relative permittivity (independent of magnetic field) and permeability (independent of the electric field), α_{ij} denotes the linear magnetoelectric coefficient, β_{ijk} and γ_{ijk} quadratic magnetoelectric coefficients, and finally δ_{ijkl} biquadratic magnetoelectric coefficient. The components of total polarization P_i and magnetization M_i in the material are derived

from the free energy by derivatives [18]

$$P_i = -\frac{\partial F}{\partial E_i} = P_i^S + \varepsilon_0 \varepsilon_{ij} E_j + \alpha_{ij} H_j + \frac{\beta_{ijk}}{2} H_j H_k + \gamma_{ijk} E_j H_k + \delta_{ijkl} E_j H_k H_l,$$
$$M_i = -\frac{\partial F}{\partial H_i} = M_i^S + \mu_0 \mu_{ij} H_j + \alpha_{ji} E_j + \beta_{jik} E_j H_k + \frac{\gamma_{jki}}{2} E_j E_k + \delta_{jkli} H_j E_k E_l. \tag{1.2}$$

From the phenomenological description of the material, we can extract the information that even in non-multiferroic materials, even in non-ferroic materials or in materials that are in the "para-" phase ($\boldsymbol{P}^S = \boldsymbol{0}$ and $\boldsymbol{M}^S = \boldsymbol{0}$), a magnetoelectric coupling can be present, because both the total polarization $\boldsymbol{P}$ and the total magnetization $\boldsymbol{M}$ depend on both electric and magnetic fields. The magnetoelectric coupling strength is fully determined by the coefficients α_{ij}, β_{ijk}, γ_{ijk} and δ_{ijkl}. Moreover, it is clear that the coefficient of linear magnetoelectric coupling α_{ij} plays a significantly larger role in the total strength of the coupling than the higher order coefficients. Nevertheless, it can be shown that the coefficient α_{ij} is non-zero only in systems with broken spatial and time inversion (i.e. in most multiferroics). The coefficient α_{ij} must satisfy the inequality [18]

$$\alpha_{ij}^2 \leq \varepsilon_0 \mu_0 \varepsilon_{ij} \mu_{ij}, \tag{1.3}$$

from which it follows that the largest *linear magnetoelectric coupling* can exist in multiferroic materials, since their permittivity ε_{ij} and permeability μ_{ij} reach the values of a higher order of magnitude (mainly in the vicinity of the phase transition) than the permittivity and permeability of the non-multiferroic materials. The quadratic and biquadratic coefficients of the coupling are not restricted by symmetry, they are always non-zero, but they have usually small values. $EuTiO_3$ is the exception. Its linear coefficients α_{ij} are zero from the symmetry considerations, but the ME coupling is still anomalously strong. It means, that the higher-order ME coefficents are very significant in $EuTiO_3$. [4]

If we understand the permittivity and permeability of the substance in a general way of meaning as coefficients of proportionality between $\boldsymbol{P}$ and $\boldsymbol{E}$ respectively $\boldsymbol{M}$ and $\boldsymbol{H}$, then the dependence of permittivity on the magnetic field and dependence of permeability on the electric field follows from the equations (1.2). Thus, the magnetoelectric coupling can be revealed in the dependence of the permittivity on the applied magnetic field. In the following text, the permittivity ε_{ij} will be understood as a quantity which includes the existence of a magnetoelectric coupling. [18]

1.2 Phonons

The dynamic behavior of the crystal lattice is described by elementary vibrational excitation (elastic waves or modes) called phonons. In the first approximation, the phonons behave as independent harmonic oscillators with frequency ω and quasi-momentum $\boldsymbol{p} = \hbar \boldsymbol{q}$, where $\hbar$ is a reduced Planck constant and $\boldsymbol{q}$ is a phonon wave vector. The phonons are thus quasi-particles. [19] If there are n phonons with the frequency ω in the material, then their total energy is equal to

$$E = \hbar\omega\left(\frac{1}{2} + n\right). \tag{1.4}$$

The phonons have zero spin, so they behave like bosons and in thermodynamic equilibrium they follow the Bose-Einstein statistics. The mean number of phonons $\overline{n}$ with frequency ω at temperature T

is then given by the relation

$$\overline{n} = \frac{1}{e^{\frac{\hbar\omega}{k_B T}} - 1}, \tag{1.5}$$

in which k_B represents Boltzmann's constant. [19] For a crystal whose primitive cell generally has p atoms, there are $3p$ phonon branches in a dispersion relation between the wave vector $\boldsymbol{q}$ and the frequency ω. Each branch is quasi-continuously occupied by individual oscillation modes. Specifically, dispersion relation contains 3 acoustic branches and $3p - 3$ optical branches. The oscillation modes are divided into longitudinal (oscillation direction corresponds to direction of propagation) and transverse (oscillation direction is perpendicular to direction of propagation), and therefore some acoustic and optical branches include longitudinal and other transverse phonons. [19]

The fonons can be excited, for example, thermally, by electromagnetic radiation, electrons or neutrons. In the infrared and Raman measurements, only those phonons can be excited, which lie almost in the center of the Brillouin zone. Thus, in each dispersion branch, only one phonon is excited. This is due to the absolute value of the photon momentum, which is several orders of magnitude smaller than the momentum of the phonon located at the boundary of the first Brillouin zone. Not all the phonons from the center of the Brillouin zone are, however, excited by electromagnetic radiation. The question of whether the phonon can be excited is answered by symmetrical considerations that are based on the group theory (see e.g. [20]). Some oscillations are so called *non-polar* and are active only in the *Raman* spectrum. Others are so-called *silent* and can not be excited neither in *infrared* (IR) nor in Raman spectra, but the silent modes are active in *hyper-Raman* spectra (Raman's scattering for the second harmonics). *Polar* phonons, which can be spectroscopically excited through IR radiation, then contribute to the frequency dependence of sample permittivity. IR spectroscopy is therefore an important tool for studying the frequencies of the phonons present in the material. In order to be the phonon polar (IR active), it must carry an electric dipole moment as the interaction of the photon with the substance is conducted directly through the electric dipole moment of the light wave. [19], [21]

An important one among the phonons is so-called soft mode, which is actually transverse optical oscillation. This low-frequency polar phonon most strongly contributes to the static permittivity (ε_s or $\varepsilon(0)$) of the material. It turns out, that the phase transition into the ferroelectric state accompanies the gradual softening (frequency decrease) of this mode with the decreasing temperature until the frequency becomes theoretically zero (we say that the soft mode is frozen) at the Curie temperature T_C of the phase transition. Under T_C, the soft mode with decreasing temperature again hardens (its frequency is growing). If the soft phonon is modeled as an anharmonic oscillation mode, then it can be derived that its frequency square follows the Cochran formula $\omega^2_{TO_j} = A(T - T_C)$ (where T is the temperature and A is a constant) and at the finite temperature T_C it freezes, which indicates transition from the paraelectric to the ferroelectric phase. [22], [23] Taking into account the Lyddane-Sachs-Teller relation [23], [24]

$$\varepsilon_S = \varepsilon_\infty \prod_{j=1}^{n} \frac{\omega^2_{LO_j}}{\omega^2_{TO_j}}, \tag{1.6}$$

where ε_∞ is the high-frequency permittivity above the phonon frequency region, ω_{LO_j} marks the temperature-independent frequency of the j-th longitudinal phonon, which belongs to the j-th transverse phonon with the frequency ω_{TO_j}, then it is clear that if the frequency of the i-th transverse phonon (i.e. our soft mode) decreases to zero as the temperature approaches to T_C, ε_S theoretically grows to infinity. This is in agreement with the Curie-Weiss law for ferroelectrics [23]

$$\varepsilon_S = \frac{C}{T - T_C}, \tag{1.7}$$

where C denotes the Curie constant, which can be considered as temperature-independent in the first approximation, and of the temperature-independent high-frequency permittivity ε_∞. In reality, however, the static permittivity value achieves at T_C only a significant maximum. [23]

Another instrument for the observation of phonons is Raman's vibrational spectroscopy, which is based on the principle of light scattering (absorption and simultaneous emission of light with the participation of the emitted or absorbed phonon). The soft mode is always infrared active in paraelectric and ferroelectric phase and Raman active only in ferroelectric phase, where the center of symmetry is lost. [23], [19]

The dependence of the phonon frequency on its wave vector $\boldsymbol{q}$ can be measured across the whole Brillouin zone using the inelastic neutron or X-ray scattering. [23], [19]

1.3 Magnons

Except the lattice vibrations - phonons, *spin waves* or *magnons* can also be observed in magnetic materials. Magnon can be imagined as an elementary magnetic excitation, it means a turn of an electron spin within a single atom in the opposite direction. As a result of the exchange between magnetic moments, such a turn is delocalized and propagates like a wave through the whole material. Like phonons, magnons are characterized by their energy and quasi-momentum. So the magnons are also quasi-particles, which we also divide into "acoustic-like" and "optic-like", and which are also governed by Bose-Einstein's statistics (1.5). [12] The magnetic Brillouin zone of ferromagnets is as large as the lattice Brillouin zone and typically contains only one magnon branch, namely the "acoustic-like" branch. The magnetic Brillouin zone of antiferromagnets or ferrimagnets may be several times smaller than the lattice one and thus it may contain "optic-like" magnon branches (magnetic Brillouin zone is folded on itself and thus the part of acoustic-like branch is converted into optic-like branch). Unlike phonons, magnons can be excited by the magnetic field of electromagnetic waves. In unmodulated magnetic structures, only magnons in the center of the Brillouin zone can be excited. Thus the ferromagnetic resonance (in microwave range) or antiferro- or ferrimagnetic resonance (in terahertz and infrared range) is observed. Such magnons subsequently change the magnetic moment of the material, and so contribute to its permeability μ. The magnons in multiferroic materials may become electrically active due to the magnetoelectric coupling, and therefore are called electromagnons. [25], [26]

1.4 Macroscopic quantities describing dielectrics

The dielectric is primarily characterized by its response to the applied electromagnetic field. This reaction describes complex dielectric permittivity, complex magnetic permeability and complex refractive index of the material. These quantities are dependent on the frequency of the applied electromagnetic field. Complex permittivity and complex permeability

$$\varepsilon(\omega) = \varepsilon_1(\omega) + i\varepsilon_2(\omega), \quad \mu(\omega) = \mu_1(\omega) + i\mu_2(\omega) \tag{1.8}$$

consist of permittivity ε_1, permeability μ_1, dielectric losses ε_2 and magnetic losses μ_2. These electromagnetic response characteristics are directly related to the complex refractive index

$$N(\omega) = n_1(\omega) + in_2(\omega), \tag{1.9}$$

the real part of which is the refractive index n_1 and the imaginary part is the coefficient of extinction n_2. [28] All the scalar complex quantities thus defined describe well the isotropic materials (materials with cubic symmetry). In the case of the description of materials with lower symmetry, all the quantities must be expanded to the tensors. All three above mentioned complex quantities are bound by a relation

$$N^2(\omega) = \varepsilon(\omega)\mu(\omega). \tag{1.10}$$

Simply, by multiplying complex permitivity with complex permeability and comparing the real and imaginary parts of both sides of the equation (1.10) we can derive formulas

$$n_1^2 - n_2^2 = \varepsilon_1\mu_1 - \varepsilon_2\mu_2, \quad 2n_1n_2 = \varepsilon_1\mu_2 + \varepsilon_2\mu_1. \tag{1.11}$$

When applied to non-magnetic materials (i.e. conventional paramagnetics) in which $\mu_1 = 1$ and $\mu_2 = 0$, [28] both formulas are considerably simplified, namely to a form

$$n_1^2 - n_2^2 = \varepsilon_1, \quad 2n_1n_2 = \varepsilon_2. \tag{1.12}$$

From the knowledge of the frequency dependence of the dielectric losses of the non-magnetic material, it is also possible to determine the frequency dependence of the real part of conductivity $\sigma_1(\omega)$ (or also $\sigma'(\omega)$) using the equation [23]

$$\sigma_1(\omega) = \varepsilon_0\varepsilon_2\omega. \tag{1.13}$$

At the end of this section it is necessary to add that in the solid state physics (and in spectroscopy in particular) it is casual to describe radiation as function of frequency (angular frequency), expressed in units Hz or eV, or in terms of the wavenumber

$$\nu = \frac{1}{\lambda}, \tag{1.14}$$

which represents the number of waves of the given radiation per unit length, typically per one centimeter, therefore units cm^{-1} are often used. This duality results in a terminological ambiguity, for example when the frequency of a photon (and also phonon frequency) is given in cm^{-1}.

1.5 Magnetostriction

Magnetostriction (or also *direct magnetoelastic effect*) is the terminus technicus used for the dependence of the interatomic distances in the magnetic material on its magnetization magnitude or magnetization direction. The relative change of the lattice parameter due to magnetostriction typically ranges between values 10^{-6} and 10^{-4}. The left part of Fig. 1.5 illustrates a qualitative change in the temperature dependence of the interatomic distances below the ferromagnetic phase transition temperature T_C of the nickel. This phenomenon is called *exchange magnetostriction* because it is a consequence of the dependence of the Heisenberg's exchange integral on the distance of atoms with non-zero magnetic moments. In the ordered state, exchange magnetostriction exhibits a weak linear dependence with magnetic field. This is called *forced isotropic magnetostriction*. Furthermore, under T_C, we see a split of the single exchange magnetostriction line. The two functional dependencies into which the exchange magnetostriction line is divided are indicated by symbols $\perp$ and $\parallel$. This marking corresponds to the external magnetic field applied to the sample in the direction perpendicular to or parallel to the direction of the sample size measurement. Magnetostriction appears to be anisotropic with respect to the external magnetic field. This is only partial true, as the total magnetostriction consists of an *isotropic* (volume) magnetostriction that occurs even with a zero outer magnetic field and an *anisotropic* magnetostriction that is sensitive

to the direction of the magnetic field. Isotropic magnetostriction originates from a quantum exchange effect (this is the above mentioned *exchange magnetostriction*) and appears also in the case of zero total magnetization of the material (each Weiss domain exhibits this type of magnetostriction separately). Anisotropic magnetostriction, on the other hand, is caused by the classical magnetic and electric interactions between atoms carrying non-zero magnetic moments. It is clear, that the strength of their interaction depends on the arrangement and directions of the magnetic moments in the lattice. The cause of the anisotropic magnetostriction is the internal change of the Weiss domain structure (rotation of the atomic magnetic moments) in the outer magnetic field. [5]

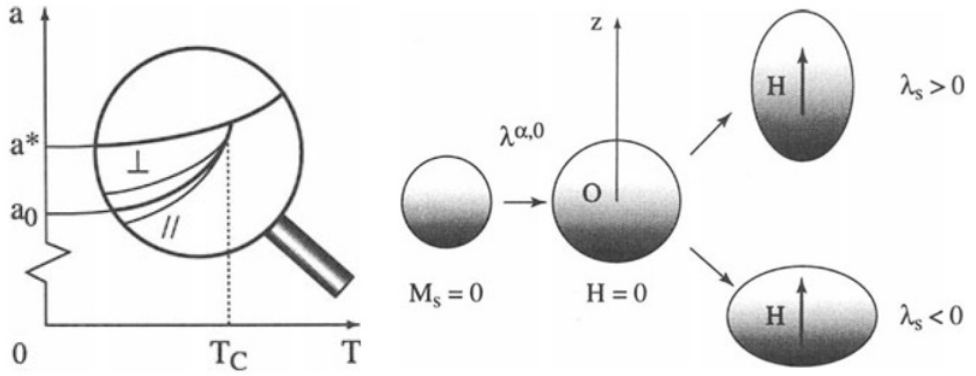

Figure 1.5: **Left:** The temperature dependence of the lattice parameter a in nickel. The substance undergoes the ferromagnetic phase transition at T_C and the magnetostriction appears. **Right:** An illustration of the qualitative difference between the isotropic magnetostriction represented by the coefficient $\lambda^{\alpha,0}$ and the anisotropic magnetostriction given by the coefficient λ_s. (figure taken from [5])

The difference between isotropic and anisotropic magnetostriction demonstrates the right part of Fig. 1.5. This captures the qualitative difference between discussed magnetostrictive contributions for isotropic material. We can see, that with the emergence of the macroscopic magnetic moment $\boldsymbol{M}$ in the Weiss domains below the phase transition temperature, the magnetostriction changes the volume of the sample even in the zero outer magnetic field $\boldsymbol{H}$. This change (*volume magnetostriction*) is not connected with the sample symmetry change (isotropic magnetostriction), and therefore can be characterized by the single coefficient $\lambda^{\alpha,0}$. However, after application the outer magnetic field, the sample is further deformed. This time we deal with a deformation that is not associated with volume changes, but only with a change in symmetry. According to the sign of the coefficient λ_s, which describes this deformation in the field direction, the spherical sample changes to an elongated or flattened ellipsoid whose linear dimensions are definitely dependent on the direction of the measurement. This is an anisotropic magnetostriction. Since anisotropic deformation does not cause a sample volume change, the isotropic sample must therefore satisfy equality $\lambda_s = \lambda_{\parallel} = -2\lambda_{\perp}$ ($\lambda_{\perp}$ stands for the magnetostriction in the direction perpendicular to the outer field). [5]

In an isotropic material, anisotropic magnetostriction is described by a single deformation parameter λ_s. In crystalline materials, in general, isotropic (volume) magnetostriction is described by one deformation parameter $\lambda^{\alpha,0}$. It is known from the theory, that this volume magnetostrictive parameter depends on mutual orientation of neighbouring spins $\boldsymbol{S_i}$ and $\boldsymbol{S_j}$ [5]

$$\lambda^{\alpha,0} = \frac{\delta V}{V_0} \sim \left\langle \boldsymbol{S_i} \cdot \boldsymbol{S_j} \right\rangle . \tag{1.15}$$

Here $\frac{\delta V}{V_0}$ marks volume magnetostriction and $\langle \boldsymbol{S_i} \cdot \boldsymbol{S_j} \rangle$ denotes so-called spin correlation function. On the other hand, anisotropic magnetostriction is described by two or more deformation coefficients. The number of these coefficients increases with the decreasing symmetry of the crystal lattice. Now let us introduce the co-ordinate system and mark the directional cosine of the i-th component of the sample total magnetization vector $\boldsymbol{M}$ (for magnetic isotropic matter, this direction is equivalent with the direction of external magnetic field) as α_i. The change of the linear dimension $\lambda = \frac{\delta l}{l}$ of the cubic single crystal measured in the direction defined by the directional cosines β_i, can be described by a formula [5]

$$\lambda = \frac{\delta l}{l} = \frac{1}{3}\lambda^{\alpha,0} + \lambda^{\gamma,2}\left[\frac{2}{3}\left(\alpha_3^2 - \frac{\alpha_1^2+\alpha_2^2}{2}\right)\left(\beta_3^2 - \frac{\beta_1^2+\beta_2^2}{2}\right) + \frac{1}{2}\left(\alpha_1^2-\alpha_2^2\right)\left(\beta_1^2-\beta_2^2\right)\right] + \\ +2\lambda^{\varepsilon,2}(\alpha_2\alpha_3\beta_2\beta_3 + \alpha_1\alpha_3\beta_1\beta_3) + \alpha_1\alpha_2\beta_1\beta_2). \tag{1.16}$$

It should be added, that the last relationship is, in fact, a mere approximation to the 1st order according to directional development. Nevertheless, higher order terms depending on the higher powers of directional cosines are negligible compared to terms of the 1st order. As we can see, anisotropic magnetostriction is described in the cubic single crystal using the 1st order approximation by two independent coefficients $\lambda^{\gamma,2}$ and $\lambda^{\varepsilon,2}$. The number p in the upper index of the coefficients λ indicates that these are the coefficients of the terms with the p-th power of directional cosines of the magnetization. Superscripts α, γ and ε refer to symmetry of magnetostriction deformation. The letter α belonging to the coefficient of isotropic magnetostriction marks conservation of the original symmetry before the magnetostriction, γ denotes the cubic symmetry reduction due to the deformation of the cubic cell along its edge and ε indicates the symmetry reduction through the shear deformation, that is, due to the change in angular ratios in the cube. [5]

Now let us move from single crystals towards the polycrystalline samples. It is obvious, that the magnetostriction will be a function of the temperature and will depend heavily on the magnitude of the applied magnetic field. Both of these external conditions influence the absolute value of the material magnetization or the directional arrangement of the atomic magnetic moments in the individual crystallites. For grains of size in the order of μm we can assume that each grain behaves as a separate Weiss domain. In a weak magnetic field, the magnetic moments of the individual crystals begin to tilt into the direction of easy magnetization. In the stronger field, the magnetization of individual grains begins to rotate out from the easy magnetization direction towards the direction of the applied magnetic field (at this stage magnetostriction changes most). Subsequently, the saturation state is achieved, where the magnetization of the polycrystal corresponds to the spontaneous magnetization in one single crystal. Further increase of the field causes only so-called paraprocess which, compared to the previous phenomena, affects the magnetization value very little. Therefore, in strong fields, we can declare magnetostriction constant with respect to the applied field. [12], [5]

For the description of the cubic polycrystalline material, the linear magnetostriction λ of the cubic single crystal (1.16) must be averaged over the angular orientation of all grains in the polycrystal. In the case of a sufficiently strong field for the magnetization to be saturated, and assuming a polycrystal with uniformly (and spatially sufficiently densely) distributed orientations of the grains, an anisotropic contribution to the magnetostriction in the direction parallel to the applied field ($\alpha_i = \beta_i$) can be expressed as [5]

$$\lambda_{\parallel}^{\mathrm{sat}} = \lambda^{\gamma,2}\left[\left\langle\beta_1^4\right\rangle + \left\langle\beta_2^4\right\rangle + \left\langle\beta_3^4\right\rangle - \frac{1}{3}\right] + 2\lambda^{\varepsilon,2}\left[\left\langle(\beta_2\beta_3)^2\right\rangle + \left\langle(\beta_1\beta_3)^2\right\rangle + \left\langle(\beta_1\beta_2)^2\right\rangle\right] = \frac{4}{15}\lambda^{\gamma,2} + \frac{2}{5}\lambda^{\varepsilon,2}. \tag{1.17}$$

Finally, it should be added that these magnetostrictive relations should be applied to a sample that was ideally isotropically demagnetized before the beginning of the outer field effect. This means that there is no preferred orientation of the Weiss domains below the magnetic phase transition temperature. If the preferred orientation exists, the magnetostriction is typically higher in certain directions, and in other directions the magnetostriction does not have to appear at all. [5]

1.6 Morphic effect

Application of an external force on the sample may lead to the lowering of its symmetry. The external force could be represented, for example, by an electric field, a stress (or strain), or by a magnetic field. All the effects caused by the lowering of the symmetry are called *morphic effects*. Stark and Zeeman shifts and splittings of electronic energy levels are examples of morphic effects in atomic structure. Within this thesis, morphic effects connected with lattice dynamics are crucial. These manifest themselves as changes in the selection rules for phonon activities in IR and Raman spectra, i.e. degenerated modes can split in electric (magnetic) field or even originally inactive modes become IR or Raman active. [6]

The whole microscopic theory of morphic effects is very complicated and far beyond the needs of this document. Next paragraphs are therefore restricted to a basic qualitative conclusions based on group theory considerations. Group theory enables to determine connection between the symmetry of a phonon mode, the type of external force, and the morphic effects expected. The mode properties can be more fundamentally expressed in terms of the crystal potential energy. For the precise microscopic theory of morphic effects and group theory treatment, please see [6]-[10].

As it was mentioned above (section Phonons), interaction of the electromagnetic radiation with the optical phonons involves phonons near the center of the Brillouin zone. Each of these phonons belongs to one phonon branch and is described by one of the irreducible representations (IRR) of the crystal point group. The IRR of the phonon then gives information about the degeneracy, polarization and activity of the mode in the spectra. [6]

Now, let us take into consideration homogeneous external magnetic field, which is not a *polar* pertrubation (as electric field) but an *axial* perturbation. On the one hand, magnetic field transforms as an axial vector under space group operations, but on the other hand, it transforms differently with respect to the *operation of time reversal*. In other words, time reversal symmetry is removed by the magnetic field. It is possible to show, that as a consequence of time reversal removal, the degenerate modes split. It can be also shown that all the modes with the same degree of degeneracy behave in the same way when a magnetic field is applied. In the first order approximation, doubly degenerate modes split linearly with the magnitude of the z component (z is the direction of the main symmetry axis) of the external magnetic field and symmetrically about the degenerate frequency ω_E. After the splitting, the corresponding phonons are left and right circularly polarized. The activities of real nondegenerate phonons are not affected by magnetic field, but their frequencies can shift. [8] The main disadvantage of the group theory is non-predictability of magnitude of above depicted effects. Group theory only says whether or not a particular effect is possible. To determine the strength of the particular effect, an independent theoretical (microscopic) approach is needed for each case. One of the earliest estimations (see [10] and references therein) determined the splitting of the mode frequencies in magnetic field in order of 0.1 cm^{-1}, but Raman experiments in [27] revealed splitting up to 30 cm^{-1} (at 6 T).

Not only external magnetic field, but also a nonzero magnetic moment destroys the time reversal symmetry. Then the system of crystal + magnetic field is described in the same way as an ordered ferromagnet. The degenerate modes may split, when the crystal undergoes the transition from the paramagnetic to magnetic state and the time reversal symmetry is destroyed. [10]

1.7 Demagnetizing field

The size and direction of the electric and magnetic fields inside the sample are determined by the external electric or magnetic field, by the physical properties of the material and by the shape of the sample. In this work, the effect of the sample shape on the total internal magnetic field is important, and therefore the discussion deal with the magnetic field only. Nevertheless, it is good to realize that all the physical quantities and relations below have their companions describing electric field. Next, let us point out that the given demagnetizing field theory assumes homogeneous and isotropic materials, which are a good approximation in case of ceramics we work with (see below for information about ceramics and experiments). Further, for the sake of simplicity, the explanation is limited to ellipsoid-shaped samples. All the facts contained in this section are taken from the book [29] (see also references in [29]).

The magnetically homogeneous ellipsoid-shaped material is always homogeneously magnetized when it is placed in the external homogeneous magnetic field $\boldsymbol{H}_0$. The resulting magnetization $\boldsymbol{M}_0$ and magnetic dipole moment $\boldsymbol{m}_V$ of this sample with volume V connects the equation $\boldsymbol{M}_0 = \frac{\boldsymbol{m}_V}{V}$. Thus magnetized sample creates its own dipole magnetic field, which again interacts with the sample itself. As a result, the so-called demagnetizing field $\boldsymbol{H}_d$ arises, which attenuates the magnetic field strength inside the sample according to the relation

$$\boldsymbol{H}_d = -\overleftrightarrow{N}\boldsymbol{M}_0. \tag{1.18}$$

In this equation, $\overleftrightarrow{N}$ represents a physical quantity called a *demagnetization (depolarization) factor*. Generally it is a second order tensor quantity. If we identify the coordinate axes with the main axes of the ellipsoid, then only the diagonal elements of the matrix $\overleftrightarrow{N}$ are non-zero. Let us denote them N_i, where i marks the direction x, y or z. Moreover, diagonal elements of $\overleftrightarrow{N}$ fulfill $N_x + N_y + N_z = 1$. It is apparent, that if the external magnetic field is applied in the direction of one of the main axes of the ellipsoid, then the direction of $\boldsymbol{H}_d$ is identical to the direction of $\boldsymbol{M}_0$ and thus identical to the direction of $\boldsymbol{H}_0$ (assuming the magnetically isotropic sample). The total magnetic field strength $\boldsymbol{H}$ and magnetic flux density $\boldsymbol{B}$ are then given by relation

$$\boldsymbol{H} = \boldsymbol{H}_0 + \boldsymbol{H}_d = \boldsymbol{H}_0 - \overleftrightarrow{N}\boldsymbol{M}_0, \qquad \boldsymbol{B} = \mu_0(\boldsymbol{H} + \boldsymbol{M}_0) = \mu_0[\boldsymbol{H}_0 + (1 - N_i)\boldsymbol{M}_0], \tag{1.19}$$

where μ_0 represents the permeability of the vacuum. Moreover, if we consider soft magnetic materials which are described by linear relation $\boldsymbol{M}_0 = \chi\boldsymbol{H}$ (here χ is the magnetic susceptibility of the material), then we can rewrite the equations (1.19) into the form

$$\boldsymbol{H} = \frac{1}{1 + N_i\chi}\boldsymbol{H}_0, \qquad \boldsymbol{B} = \frac{1 + \chi}{1 + N_i\chi}\boldsymbol{B}_0. \tag{1.20}$$

Now consider a very elongated ellipsoid of revolution (prolate spheroid) with the long axis in the z direction. In this case, the demagnetizing factors are approximately equal to $N_x = N_y \doteq \frac{1}{2}$ and $N_z \doteq 0$. If the external magnetic field is parallel to the z axis, then we can write

$$\boldsymbol{H}_d \doteq \boldsymbol{0}, \qquad \boldsymbol{H} \doteq \boldsymbol{H}_0, \qquad \boldsymbol{B} \doteq \mu_0(\boldsymbol{H}_0 + \boldsymbol{M}_0). \tag{1.21}$$

However, if the external magnetic field is parallel to the x or y axis, then the magnetic field inside the sample is subjected to equations

$$\boldsymbol{H}_d \doteq -\frac{1}{2}\boldsymbol{M}_0, \qquad \boldsymbol{H} \doteq \boldsymbol{H}_0 - \frac{1}{2}\boldsymbol{M}_0, \qquad \boldsymbol{B} \doteq \mu_0(\boldsymbol{H}_0 + \frac{1}{2}\boldsymbol{M}_0). \tag{1.22}$$

On the contrary, a very flattened ellipsoid (oblate spheroid) with the short axis in the z direction is characterized by $N_x = N_y \doteq 0$ and $N_z \doteq 1$. So if the field is perpendicular to the z axis, then the situation is described by equations (1.21). In the case of the external magnetic field parallel to the z axis, previous relations are transformed to the form

$$\boldsymbol{H}_d \doteq -\boldsymbol{M}_0, \qquad \boldsymbol{H} \doteq \boldsymbol{H}_0 - \boldsymbol{M}_0, \qquad \boldsymbol{B} \doteq \mu_0\boldsymbol{H}_0. \tag{1.23}$$

1.8 Structural and physical properties of $EuTiO_3$

1.8.1 Structural characterization

The titanium-europium oxide $EuTiO_3$ (or europium titanate) crystallizes at room temperature in a so-called perovskite structure named after a mineral $CaTiO_3$, whose structure was first described in 1839 by Mineralogist Gustav Rose, who called it Perovskite in honor of his Russian sponsor and mineralogist Lev Perovski. [30] The cubic perovskite structure is characterized by a space group $Pm\bar{3}m$, which is one of the space groups belonging to a point group O_h (cubic point group of an octahedron with a center of symmetry). The basis of the perovskite structure is always formed by the ions of the compound described by a general formula ABX_3. Talking about $EuTiO_3$, these ions are Eu^{2+} cation, Ti^{4+} cation and three O^{2-} anions. From the illustration of the perovskite structure (Fig. 1.6) could be seen that the tetravalent cation B occupies a position in the center of the unit cell, the divalent cation A occupies its corners and the anion is present at the centers of its faces. Thus, the oxygen anions form the corners of the octahedron. $BaTiO_3$, $NaNbO_3$, $KNbO_3$, $CaZrO_3$, $PbTiO_3$ or $SrTiO_3$ also crystallize in the perovskite structural type, but some of them can exhibit phase transition from cubic to lower symmetries. [31]

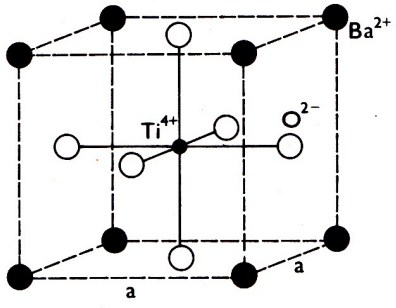

Figure 1.6: Structure of cubic $BaTiO_3$ - perovskite structural type. (figure taken from [31])

The latter, titanium-strontium oxide, is structurally related to titanium-europium oxide. Both the strontium and europium have the same valency of 2+ in these oxides, and both cations have a very similar ion radius, so $SrTiO_3$ and $EuTiO_3$ have practically same lattice parameters ($a \sim 3,91$ Å) at 300 K. [3], [32] In addition, $SrTiO_3$ is one of the most studied perovskites, and therefore the structural research of $EuTiO_3$ was based on the similarity with $SrTiO_3$ from the very beginning. $EuTiO_3$ was synthesized

already in 1953, [33] but attention was focused on it at the turn of the millennium, when its interesting magnetic and magnetoelectric properties were discovered. [3]

The group around A. Bussmann-Holder theoretically predicted in 2011 that $EuTiO_3$ would have to (similarly as the $SrTiO_3$) undergo a structural phase transition from cubic to tetragonal structure and really discovered this transition at 282 K through the measurement of specific heat. [34] Two independent structural papers confirmed this transition by X-ray powder diffraction and observed the splitting of cubic lattice parameter into two tetragonal lattice parameters. [35], [36] During the phase transition to a tetragonal structure with a space group $I4/mcm$ there is an antiphase rotation of the oxygen octahedra around the c axis, and therefore the low-temperature primitive tetragonal cell has a double size (Fig. 1.7). [35] According to A. M. Glazer's notation, who dealt with general cases of oxygen octahedron rotation and its influence on structure in the perovskite materials, the structural phase transition in $EuTiO_3$ can be labeled as $a^0a^0c^-$, indicating that there are no rotations along the axis a and b, and the octahedra are rotated in the antiphase way only around the c axis. [37]

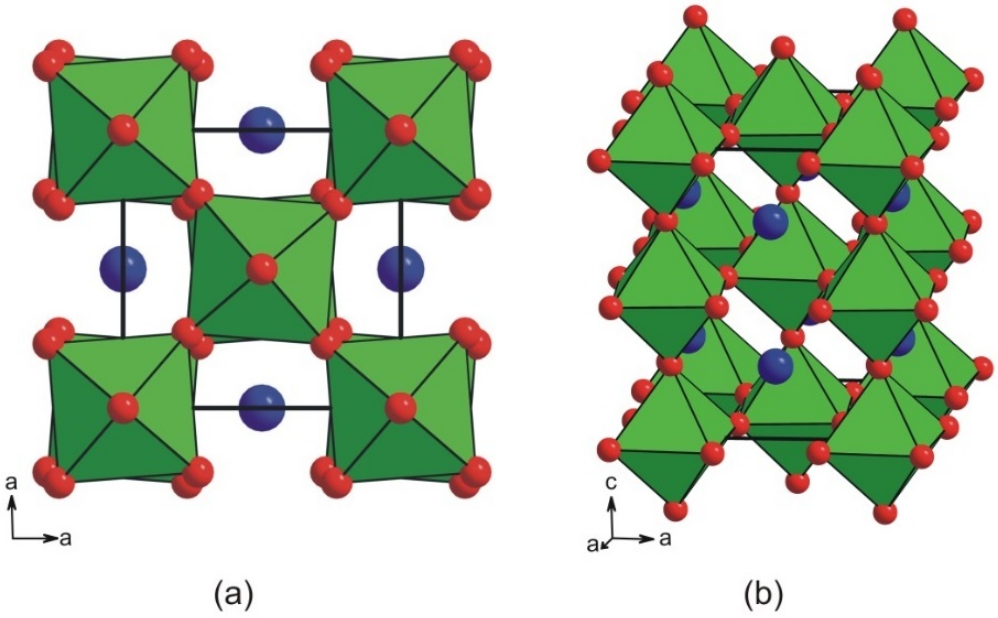

Figure 1.7: Illustration of the rotation of the oxygen octahedra in $EuTiO_3$. The octahedrons in the adjacent layers along the c direction rotate always in the opposite way (antiphase rotation along the c direction). Red balls indicate oxygen ions forming green octahedrons, and blue balls denote europium ions. Titanium ions are always located in the center of the octahedron. (figure kindly provided by J. Drahokoupil, and created according the experimental data gained by Goian V. et al. [36])

1.8.2 Electric and magnetic properties

The specifics of phase transition from cubic to tetragonal phase in $EuTiO_3$ can be highlighted in comparison with the phase transition in $BaTiO_3$. This material also undergoes a structural phase transition from group $Pm\bar{3}m$ to a tetragonal group. In this case, however, it is group $P4mm$. During this transition, there is no antiphase rotation of oxygen octahedrons (the volume of the primitive cell does not change),

but the Ti^{4+} ion is displaced from the center of the oxygen octahedron. Thus an electric dipole moment is generated. Due to mutual interactions, these dipoles in a certain area, which we call a domain, are aligned along the same c axis, and thus a ferroelectric arrangement emerges. The typical feature of the transition to the ferroelectric state is the maximum in the temperature dependence of the static permittivity $\varepsilon_1(0)$ (not necessary static permitivity, but the low frequency permittivity, i.e. at frequencies significantly lower than the phonon frequencies) at the ferroelectric phase transition temperature. [38]

$EuTiO_3$ has an antiferrodistortive phase transition similar to $SrTiO_3$. During this transition, the cubic structure changes to tetragonal, but it is due to the rotation of oxygen octahedra and not because of the metal ion displacement. Therefore there is no induced ferroelectric polarization. However, the permittivity for both materials is anomalously increased on cooling to helium temperatures because the internal structure is close to the ferroelectric phase transition. However, the transition does not occur because of the quantum fluctuations at low temperatures, which prevent this transition. [32] That is why both materials are called incipient ferroelectrics. In the case of $SrTiO_3$, this term is further expanded and so-called quantum paraelectricity is mentioned. The reason for the terminological difference is that the hypothetical temperature of the ferroelectric transition for $SrTiO_3$ is around 30 K, [32] whereas for $EuTiO_3$ this hypothetical temperature (determined from the Curie-Weiss extrapolation of the permittivity temperature dependence) is negative (−220 K). [3] According to Katsufuji and Takagi, [3] the increase of $\varepsilon_1(0)$ in $EuTiO_3$ is caused by the softening of the low-frequency transverse optical (TO) phonon.

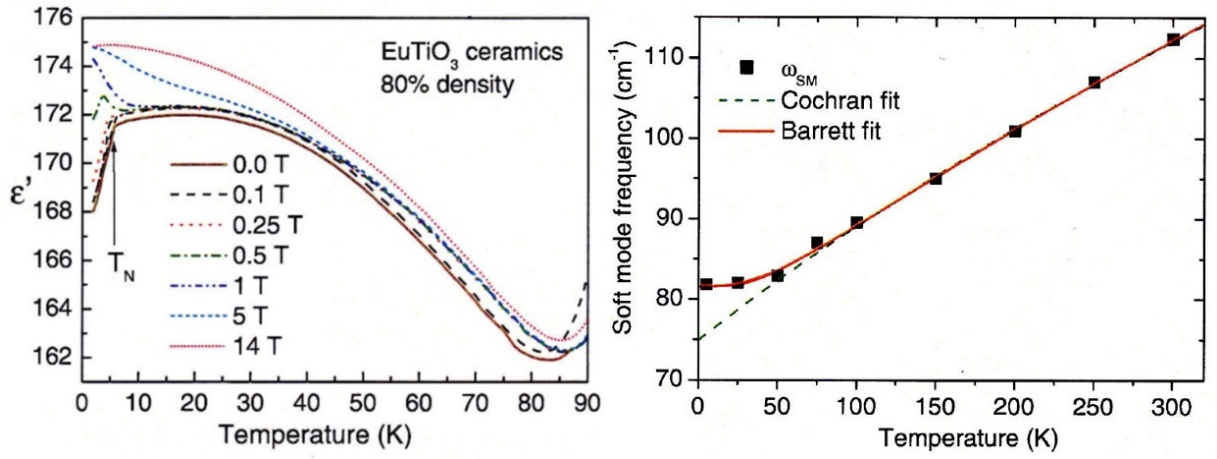

Figure 1.8: **Left:** Temperature dependence of $EuTiO_3$ ceramics permittivity, which was measured at 1 kHz and for several values of applied magnetic field. Néel temperature characterizing antiferromagnetic phase transition is denoted as T_N in the graph. **Right:** Temperature dependence of the soft phonon frequency ω_{SM}. The behaviour of ω_{SM} follows the Barrett formula for soft mode frequency influenced by quantum fluctuations. [24] (figure taken from [24])

Their claim about the phonon softening was verified by a group around S. Kamba from the Institute of Physics of the CAS. [24] The measurement results of this group are shown in Fig. 1.8. If we investigate the temperature dependence of permittivity measured in a zero magnetic field, we can see that the permittivity value increases with decreasing temperature until it begins to saturate below the temperature of ∼ 30 K, then decreases slightly and even sharply drops under the 5 K. This behaviour corresponds to the measured soft mode frequency dependence shown in the right part of the figure. The saturation of the softening apparently begins at ∼ 50 K. The decrease in permittivity under the T_N should be caused

by the increase in the soft mode frequency. However, this is not visible in Fig. 1.8, because the IR measurement was not performed below 5 K because of experimental limitations. [24]

Despite the similarities between $EuTiO_3$ and $SrTiO_3$ in terms of structure and electrical properties, both have a different magnetic arrangement. While $SrTiO_3$ behaves as a classical diamagnet, [32] paramagnetic $EuTiO_3$ undergoes the antiferromagnetic (AFM) phase transition at Néel temperature $T_N = 5.3$ K (the Eu^{2+} cation has seven unpaired electrons in the valency shell and these are subjected to the long-range arrangement). [39] Study of the polycrystalline sample structure by neutron diffraction shows the so-called type G AFM structure. In this arrangement each Eu^{2+} cation neighbours with the 6 closest Eu^{2+} with antiparallel spin and with the 12 other second closest Eu^{2+} with parallel spin (see Fig. 1.9). It was also found that at 1.3 K the magnetic moment in the $EuTiO_3$ increases with the external magnetic field linearly up to $\sim$ 1 T. Then the increase decelerates and subsequently magnetic moment achieves its practical maximum value 6.93 μ_B in 1.4 T field (μ_B stands for Bohr's magneton). This means that field necessary for the magnetization saturation is relatively weak (see also Fig. 1.12). [39]

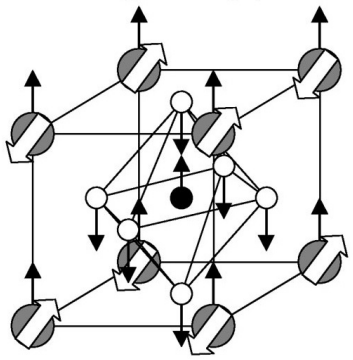

Figure 1.9: Crystal and magnetic structure of the $EuTiO_3$. Grey, white and black circles correspond to ions Eu^{2+}, Ti^{4+}, and O^{2-} respectively. Thick white arrows represent antiferromagnetic arrangement of Eu^{2+} spins. Thin black arrows are related to an ion motion of the soft phonon. (figure taken from [3])

1.8.3 Magnetoelectric coupling

Katsufuji and Takagi found, that under the T_N, the static (or low frequency) permittivity $\varepsilon_1(0)$ temperature dependence of $EuTiO_3$ is strongly bound to the size of the external magnetic field, [3] which is a proof of the great influence of the magnetic arrangement on the lattice vibrations and therefore a proof of the magnetoelectric coupling. A similar dependence, as was measured by the Japanese physicists, was obtained by the mentioned group around S. Kamba, and thus were the results confirmed (the Czech group used $EuTiO_3$ polycrystalline sample while the Japanese duo made measurements on the single crystal so that the absolute values of the permittivity differs, however the dependence on the temperature and also on the magnetic field was qualitatively very similar). [24] The experimental results of the Czech group are shown in Fig. 1.8. We see, that there is a sharp fall in $\varepsilon_1(0)$ under T_N, but also the $\varepsilon_1(0)$ under T_N increases with an increasing field size, so finally, in a sufficiently strong magnetic field, the trend changes and the $\varepsilon_1(0)$ continues to rise with the temperature decrease. The material then actually behaves (from the electrical point of view) as an incipient ferroelectric. [3]

Katsufuji and Takagi predicted the soft mode frequency dependence on the spin arrangement of the Eu^{2+} cations, because they expected a change in the hybridization of Eu^{2+} orbitals with respect to $2p$ or-

bitals of oxygen during the spin rearrangement. Accordingly, this spin-orbital coupling results in hardening of the soft phonon under T_N. The dependence of $\varepsilon_1(0)$ on the applied magnetic field is then an obvious consequence of this prediction, since the spins are reoriented after the field is applied, the outer magnetic field straightly affects the soft mode frequency (this was experimentally confirmed in paper [40]) and thus the $\varepsilon_1(0)$ value. Moreover, Japanese scientists [3] have progressed in theory also to a quantitative analysis. From a theoretical model assuming the interaction of Eu^{2+} with the closest and the second closest Eu^{2+} ions and at the same time assuming the cubic symmetry of the lattice, they were able to derive the relation

$$\varepsilon_1(T,H) = \varepsilon_{1_T}(T)\left(1 + \alpha\left\langle \boldsymbol{S_i}\cdot\boldsymbol{S_j}\right\rangle\right), \tag{1.24}$$

predicting the dependence of static permittivity $\varepsilon_1(0)$ of the $EuTiO_3$ on temperature T and magnetic field strength H. $\varepsilon_1(0)$ stands here out as a function of static permittivity without spin correlation $\varepsilon_{1_T}(T)$ (obtained by fitting the measured data and extrapolating the fit curve under T_N), binding parameter between spin correlation and static permittivity α (again obtained by fitting), and the spin correlation $\left\langle \boldsymbol{S_i}\cdot\boldsymbol{S_j}\right\rangle$, where $\boldsymbol{S_i}$ and $\boldsymbol{S_j}$ are the average spin sizes of the Eu^{2+} ions in neighbouring magnetic sublattices. [3] It is clear that $\left\langle \boldsymbol{S_i}\cdot\boldsymbol{S_j}\right\rangle$ depends on both T and H. Due to the thermal movement, the spins in the sublattices are not exactly antiparallel. The chaotic nature of their movement increases with increasing temperature and therefore the absolute value of the $\left\langle \boldsymbol{S_i}\cdot\boldsymbol{S_j}\right\rangle$ decreases. Exact calculations of the spin correlation function $\left\langle \boldsymbol{S_i}\cdot\boldsymbol{S_j}\right\rangle$, which were performed by Japanese scientists taking into account several simplifying assumptions, are shown in Figure 1.10.

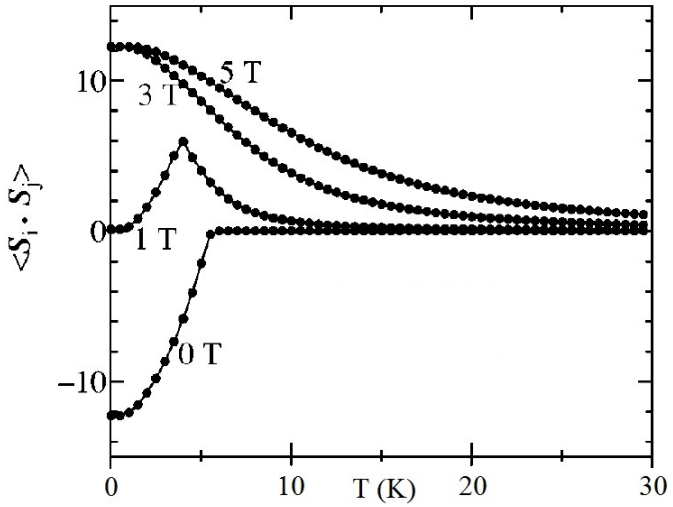

Figure 1.10: Theoretically calculated courses of the $\left\langle \boldsymbol{S_i}\cdot\boldsymbol{S_j}\right\rangle$ as a function of T and applied magnetic field. (figure taken from [3])

The presented theoretical model was subsequently eperimentally confirmed by the authors themselves. [3] Their measured data of the $\varepsilon_1(T,H)$ well agreed with the theoretical prediction not only for temperatures below, but also above T_N. Moreover, results in the previously discussed Fig. 1.8 are also in accordance with the introduced model. However, some time ago, experimental data were obtained at the Institute of Physics of the CAS, which showed the dependence of the 1 kHz permittivity (i.e. low frequency permittivity) of $EuTiO_3$ polycrystalline sample on the direction of the external magnetic field. [41] The data indicates differencies between the cases when permittivity was measured along

or perpendicular to the static magnetic field (results are presented in Fig. 1.11). At 2 K and 1 T, the difference of the relative permittivities between these directions was ~ 8, which is more than 2 % anisotropy for the investigated sample. From a structural point of view, in ideal polycrystals, all directions are equivalent, thus resulting anisotropy is induced by outer magnetic field. However, the dependence of the permittivity on the magnetic field orientation was not predicted by Katsufuji's and Takagi's model.

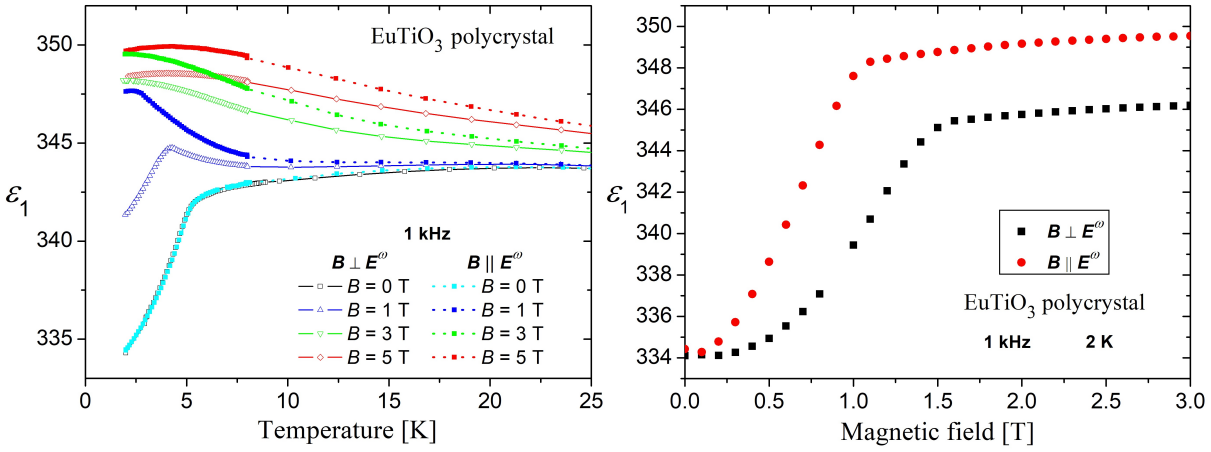

Figure 1.11: **Left:** Temperature dependence of the 1 kHz permittivity (ε_1) of the $EuTiO_3$ polycrystal. The permittivity was measured in external magnetic field of various absolute values B for both directions - parallel and perpendicular to the applied magnetic field. **Right:** The ε_1 dependence of the $EuTiO_3$ polycrystal on the B again for the same configurations. The frequency of the electric field $\boldsymbol{E}^{\omega}$ was 1 kHz and temperature 2 K. [41]

Let us discuss the temperature and field dependence of 1 kHz permittivity displayed on the left side of the figure 1.8. Obviously, for weak magnetic fields, those functions have a small maxima. However, they do not indicate a phase transition to the ferroelectric phase. In our case, the low temperature permittivity saturates due to the attenuation of the soft mode softening (Fig. 1.8-right). This attenuation occurs due to low temperature quantum fluctuations. The course of permittivity in the vicinity of the AFM phase transition (and also below it) is thus strongly influenced by the spin correlation function $\langle \boldsymbol{S_i} \cdot \boldsymbol{S_j} \rangle$ (see relation (1.24)). However, the magnetically independent component of the permittivity $\varepsilon_{1_T}(T)$ does not acquire the maximum and from this point of view, $EuTiO_3$ actually behaves as an incipient ferroelectric. [3], [24]

One of the goals of this Diploma thesis and partially of my previous Bachelor thesis [11] is to clarify the origin of the permittivity anisotropy, which should arise in the magnetic field. We have explored several options that directly or indirectly, more or less likely, influence the behaviour of permittivity. These physical effects are discussed in the following paragraphs.

1.8.4 Magnetostriction and magnetization

In 2014, an article [42] dealing with magnetostriction in $EuTiO_3$ ceramics was published. The experimental results contained in the article are shown in Figure 1.12. The left part shows sample contraction during temperature decrease in zero applied magnetic field. This contraction is caused mainly by volume (isotropic) magnetostriction and additionally by thermal expansion. It is also evident that magnetostrictive hysteresis does not occur in the ceramics, since measurements for zero magnetic field before and after

the field are overlapped, and it can be assumed that the ceramic is isotropically demagnetized once the field is switched off. [42]

In general, the magnetostriction is affected by the value of sample magnetization. The right part of Fig. 1.12 shows the absolute value of the magnetic moment per Eu atom. The maximum value of this quantity (given by the electron configuration of Eu^{2+} ions) is 7. [42] At first, we observe a linear increase with a magnetic field for all temperatures, but saturation occurs at higher magnetic fields. The convergence of the saturation is affected by the temperature. While at 2 K the curve breaks above 1 T, at 7 K (above the magnetic phase transition) saturation occurs very slowly at higher fields due to the considerable thermal disruption of the magnetic order. Mark that the $1 - 2$ T strong magnetic field needed to saturate magnetization in the AFM state is very weak compared to other materials. This indicates a weak exchange antiferromagnetic interaction between adjacent spins. This weak interaction is also expressed through a low temperature of the Neél phase transition ($T_N = 5.3$ K). Note that the mean magnetic moment values of the Eu atom correspond to the deformation of the sample in the left part of the Fig. 1.12. Mostly, the deformation of the ceramics varies at lower fields where the magnetization of the sample increases steeply. After magnetization saturation, the sample is deformed significantly less. [42]

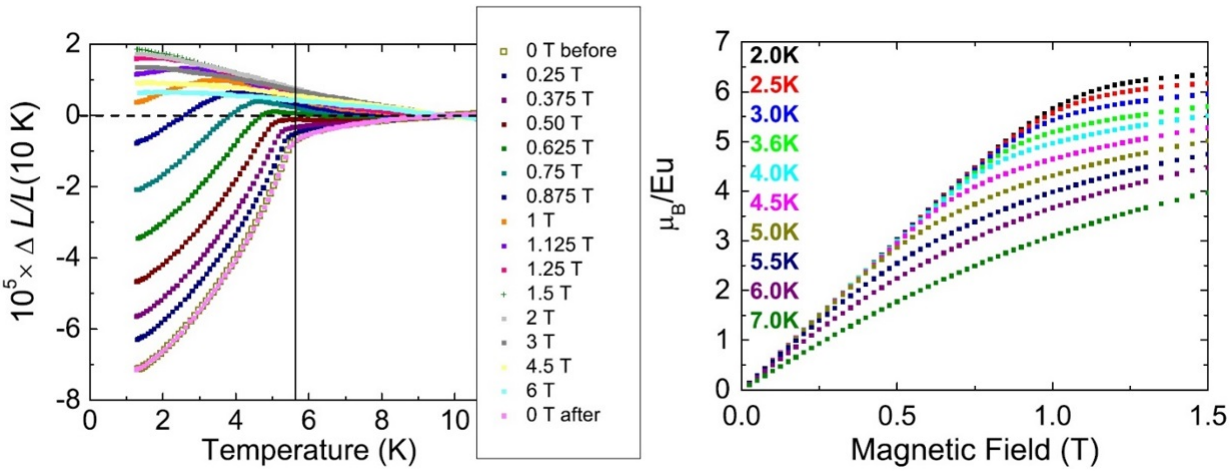

Figure 1.12: **Left:** Relative length change $\frac{\Delta L}{L}$ of the $EuTiO_3$ ceramics as a function of temperature and size of applied magnetic field. Reference length L, to which the extension is related, was measured at 10 K. **Right:** Temperature and field dependence of atomic magnetic moment. Absolute value of the moment is statistically related to one Eu atom and expressed in units of Bohr magneton μ_B. (figure taken from [42])

The first look at magnetostrictive data in Fig. 1.12 suggests their correlation with 1 kHz permittivity curves at temperatures below 10 K (Fig. 1.8 and 1.11). Dependencies show very similar courses and so the question naturally arises, whether these phenomena are mutually dependent. However, as it was described above, volume magnetostriction is governed by the same spin correlation function $\langle \boldsymbol{S_i} \cdot \boldsymbol{S_j} \rangle$ (see (1.15)) as permittivity in Katsafuji and Takagi's model, which is described by equation (1.24). Nevertheless, the magnetostrictive dependence of Fig. 1.12 differs slightly from the course of the spin-correlation function itself (Fig. 1.10). Magnetostriction is apparently not as symmetrical about the x axis as the spin-correlation function, but it reaches greater negative and smaller positive values. It should be noted that, apart from magnetostriction, thermal expansion also contributes to the sample size change. However, thermal expansion is usually very low in the materials below 10 K, also usually increases

only above 50 K and above 100 K is usually linear with temperature. The magnetostriction itself consists of two contributions (see equations (1.16) and (1.17)). The first of these contributions, namely the isotropic (volume) magnetostriction, depends on the spin correlation function linearly, whereas the anisotropic magnetostriction does not show such a simple dependence. It follows that the volume magnetostriction is predominant in $EuTiO_3$, but the anisotropic magnetostriction is not negligible. According to the general physical properties of magnetostriction (see section Magnetostriction), the anisotropic contribution to total magnetostriction is either positive or negative in a direction parallel to the external field and opposite in directions perpendicular to the external field. The contribution of anisotropic magnetostriction is most apparent in fields above 1.5 T, when the magnetization is already saturated (the $\langle \boldsymbol{S_i} \cdot \boldsymbol{S_j} \rangle$ function persists practically unchanged) and the volume contribution thus remains constant.

From the above it is clear that the analogy between the permittivity and the volume magnetostriction is purely random, since both variables depend directly on $\langle \boldsymbol{S_i} \cdot \boldsymbol{S_j} \rangle$ and are independent on each other. However, in principle, there may be a link between anisotropy in low frequency permittivity and anisotropic magnetostriction. The low frequency permittivity ε_1 is experimentaly determined from the equation

$$C = \frac{\varepsilon_0 \varepsilon_1 S}{d} \tag{1.25}$$

expressing a capacitance of a capacitor. Here ε_0 is the permittivity of the vacuum, S is the area of the capacitor plates and d is their distance defined by the linear dimension of the sample. With a significant change in the dimension d of the sample, the capacitance of the capacitor changes considerably and this capacitance difference could be misinterpreted as a change in permittivity (constant sample size during the low-frequency permittivity measurements is normally assumed). By including anisotropic magnetostriction, which has either positive or negative sign in direction parallel to the magnetic field and opposite sign in the perpendicular direction, the possible anisotropic nature of 1 kHz permittivity of the $EuTiO_3$ could be explained. The problem, however, is that the relative change of $EuTiO_3$ ceramics dimensions (according to experimental data in Fig. 1.12) varies in the order of ~ 0.001 %, whereas the detectable change in permittivity has to be at least ~ 1 %. Thus, magnetostriction probably does not cause the anisotropy in permittivity. Nevertheless, we started to measure magnetostriction of $EuTiO_3$ ceramics in order to obtain our own experimental data and compare them with the data contained in the article [42].

1.8.5 Morphic effect in the $EuTiO_3$ ceramics

The possible anisotropy of the permittivity of the $EuTiO_3$ ceramics (see Fig. 1.11) is expected to be induced by an application of external magnetic field due to morphic effect theoretically discussed in section 1.6. Therefore, let us now consider general facts in relation to $EuTiO_3$ ceramics.

$EuTiO_3$ ceramics are composed of tetragonal single crystalline grains. According to the factor-group analysis in tetragonal $I4/mcm$ phase, [36] 5 E_u and 3 A_{2u} symmetry phonons are expected in the IR spectra. Note, the E_u modes are double degenerated, because they are active in IR spectra polarized in tetragonal plane, while A_{2u} modes are polarized along the tetragonal axis. In magnetic field applied along tetragonal z axis, the E_u modes can split, while the A_{2u} mode frequencies can shift. After application of the magnetic field on single crystal, the permittivity of $EuTiO_3$ single crystal should change differently along and perpendicularly to magnetic field due influnce of morphic effect on phonon frequencies. Nevertheless, in our case, the $EuTiO_3$ sample is ceramics, so we cannot expect any macroscopic morphic effect.

As mentioned above, the external pertrubation affects phonons in three ways. Either it can lift phonon degeneration or affect the frequency of individual phonons or change phonon selection rules for scattering processes and infrared absorption. Consequently, the permittivity of the material is affected by the change of phonon properties (dependence of permittivity on phonon frequencies will be described below). However, the external magnetic field itself (or equivalently generation of non-zero magnetic moment) does not remove the possible center of symmetry of the system, and therefore all selection rules remain valid. It is worth noting that $EuTiO_3$ undergoes the AFM state transition at $T_N = 5.3$ K. Generally, AFM ordering may remove the center of symmetry. However, it is clear from the Fig. 1.11 that the permittivity does not exhibit anisotropy at zero external magnetic field and thus phonons are not affected (at least not detectably) by the transition to the AFM state itself. Therefore, the possible anisotropy of permittivity (seen in Fig. 1.11) is unlikely to be caused by the morphic effects.

Chapter 2

Methodics of the experiment and data evaluation

2.1 Basic spectroscopic relations

Incident electromagnetic radiation on the sample surface can either be reflected, absorbed, passed through a sample (transmitted), or diffuse scattered from the surface. However, in the case of well-polished samples, the diffuse scattering is negligible. Thus, the intensity of the incident beam I_0 is divided into the intensity of the reflected beam I_R, the intensity of the transmitted beam I_T and the intensity of the incident beam, which is absorbed I_A. The energy conservation law then gives

$$\frac{I_R}{I_0} + \frac{I_A}{I_0} + \frac{I_T}{I_0} = \tilde{R} + \tilde{A} + \tilde{T} = 1, \tag{2.1}$$

where $\tilde{R}$ is the "apparent" reflectivity, $\tilde{A}$ is "apparent" absorption, and $\tilde{T}$ is the "apparent" transmissivity of the sample. These quantities are called "apparent", because "true" companions of these quantities are defined under more specific conditions (for example reflectivity is defined for an infinitely thick sample for which there is no transmission). The magnitudes of these "apparent" and "true" quantities may be slightly different, but mentioned differencies are insignificant or negligible in our experimental conditions. [21]

With "true" reflectivity and transmissivity for dielectrics, other physical quantities, such as complex permittivity, permeability and refractive index, are connected. In the case of reflectivity measurement of a sufficiently thick sample, the transmission can be neglected. For an incident beam almost parallel to normal surface, the "true" reflectivity of the sample is governed by the formula [43]

$$R(\omega) = \left| \frac{\sqrt{\varepsilon(\omega)} - \sqrt{\mu(\omega)}}{\sqrt{\varepsilon(\omega)} + \sqrt{\mu(\omega)}} \right|^2 . \tag{2.2}$$

If the sample is non-magnetic, the previous relation can also be written in the form [21], [24]

$$R = \left| \frac{\sqrt{\varepsilon(\omega)} - 1}{\sqrt{\varepsilon(\omega)} + 1} \right|^2 = \frac{(n_1 - 1)^2 + n_2^2}{(n_1 + 1)^2 + n_2^2}. \tag{2.3}$$

For the "true" transmissivity of the sample in the form of a parallel plate of a thickness r it is easy to derive the formula [21]

$$T = \frac{I(r)}{I(0)} = e^{-Lr} \wedge L(\omega) = 2\frac{\omega}{c} n_2, \tag{2.4}$$

in which $I(r)$ is the radiation intensity at depth r under the sample surface, $I(0)$ is the radiation intensity at zero depth under the sample surface, and c is the speed of light. This formula is also known as the Beer's Law. [21]

2.2 Infrared spectroscopy

Infrared spectroscopy uses radiation with wavenumbers within the interval $\nu = 10 - 12500$ cm^{-1}. Formally, this spectral range is still subdivided into a *near* infrared range ($\nu = 4000 - 12500$ cm^{-1}), a *middle* infrared (MIR) range ($\nu = 400 - 4000$ cm^{-1}) and a *far* infrared (FIR) range ($\nu = 10 - 400$ cm^{-1}) that already overlaps with a region termed terahertz radiation (typically $\nu = 3 - 100$ cm^{-1}). Infrared spectral regions have gained their names by the magnitude of the separation from the visible light in the spectrum of electromagnetic waves. [44]

Infrared (IR) radiation has wavelength which is compatible with the frequencies of the vibrations of the molecules or with the frequencies of phonons and magnons (magnetic excitation) in solids. Therefore, infrared spectroscopy is a powerful tool for classifying physical phenomena and studying their dynamics, for detecting the force interactions and the existence of chemical bonds in solids, liquids and gases without reference to its organic or inorganic origin. [44]

Older dispersion spectrometers used for measurement gradual decomposition of radiation to individual wavelengths through monochromator. These monochromatic components were then separately recorded. However, the above-mentioned detection method is time consuming because of gradual measuring of the intensity of the individual radiation components. Moreover, for less stable and less intense sources of IR radiation (especially in the far infrared region), the measurements made in this way are slow and not very precise due to high noise. This led to development of other types of spectrometers (mainly Fourier transform), which are able to eliminate these problems. [44]

2.2.1 Fourier Transform Infrared Spectrometers

The time of spectra acquisition has been substantially reduced through the development of spectrometers using Fourier signal transformation (FTIR – *Fourier Transform Infrared* Spectrometers). In these spectrometers, the polychromatic beam intensity is detected and decomposed in the spectrum using Fourier Transform, while in the dispersive spectrometers the spectrum is measured frequency by frequency, which is very slow process and signal to noise ratio is rather low. Measured signal is then significantly stronger and hence less noisy in FTIR. Conducting an experiment is thus greatly accelerated. The FTIR spectrometer *Bruker IFS 113v* is used for measurements at the Institute of Physics of the Czech Academy of Sciences and therefore, the operation of these spectrometers will be briefly explained in the following paragraphs. [26]

FTIR spectrometers operate on the basis of the phase shift achieved using the Michelson interferometer (the simplest construction shown in Fig. 2.1). IR beams impact at an angle of 45° on the beamsplitter (half-transparent mirror), from which the passed and reflected beam is aimed at the mirrors. One of the mirrors is fixed, while the other is adjustable. From the mirrors, the rays are reflected back to the beamsplitter, where they are reflected (transmitted) and interfere. The reassembled beam continues in the direction of the sample (or to the mirror in the reference reflectivity measurement) and to the detector that records the intensity of the incident radiation. Owing to the positioning of one of the mirrors, it is possible to create a certain path difference between the two interfering beams, and thus affect the inten-

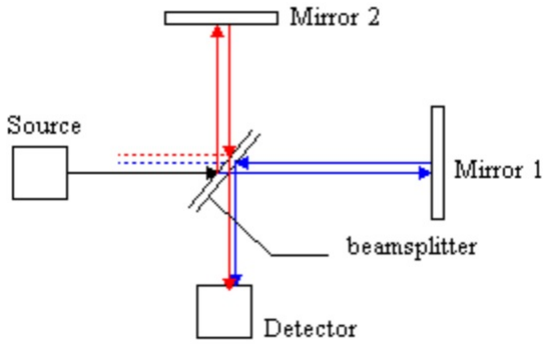

Figure 2.1: The diagram of the Michelson interferometer. (figure taken from [45])

sity of the interference. In the case of monochromatic wave of the initial intensity I_0 and the frequency ν, the intensity I of the detected beam depends on the path difference δ of the beams and it can be described by the relation [44]

$$I(\delta) = \frac{I_0}{2}[1 + \cos(2\pi\nu\delta)]. \tag{2.5}$$

The intensity $I_0(\nu)$ of polychromatic radiation generated by the source (or intensity of radiation after interaction with the sample) is frequency dependent. The equation (2.5) is then formally transformed into form

$$I(\delta, \nu) = S(\nu)[1 + \cos(2\pi\nu\delta)], \tag{2.6}$$

in which $S(\nu) = \frac{I_0(\nu)}{2}$ is the so-called spectral intensity. The total intensity of the detected polychromatic radiation is then a sum of all its components, so this intensity depends only on the path difference between interfering beams, namely as follows:

$$I(\delta) = \int_0^{+\infty} S(\nu)[1 + \cos(2\pi\nu\delta)]\mathrm{d}\nu. \tag{2.7}$$

The last equation, is an expression of a fact, that the intensity of the detected radiation is the Fourier transform of the spectral intensity. Then it is clear, that by using an inverse Fourier transform, the spectral intensity of the beam can be calculated as [44]

$$S(\nu) = \int_0^{+\infty} \left[I(\delta) - \frac{1}{2} I(0) \right] \cos(2\pi\nu\delta)\mathrm{d}\delta. \tag{2.8}$$

The last two relations show the meaning of a Fourier transform spectrometer. From the measured total radiation intensity as a function of the path difference (so-called *interferogram*) between the rays in the Michelson interferometer, it is possible to obtain complete information about the spectral composition of the detected beam performing the Inverted Fourier Transform. From the experiment, of course, we are able to gain path differences only up to a certain maximum and not to infinite values (as required by the equation (2.8)), nevertheless this difficulty can be mathematically treated with the so-called apodization function. [44] The integral is then calculated numerically through an algorithm called the *Fast Fourier Transform*. [26]

The scheme of the Bruker spectrometer is illustrated in Fig. 2.2. The radiation travels from the source (a), which is in our case the mercury lamp for the far IR or the Globar for the middle IR region, then through the Michelson interferometer (b), where the path difference of interfering beams is created

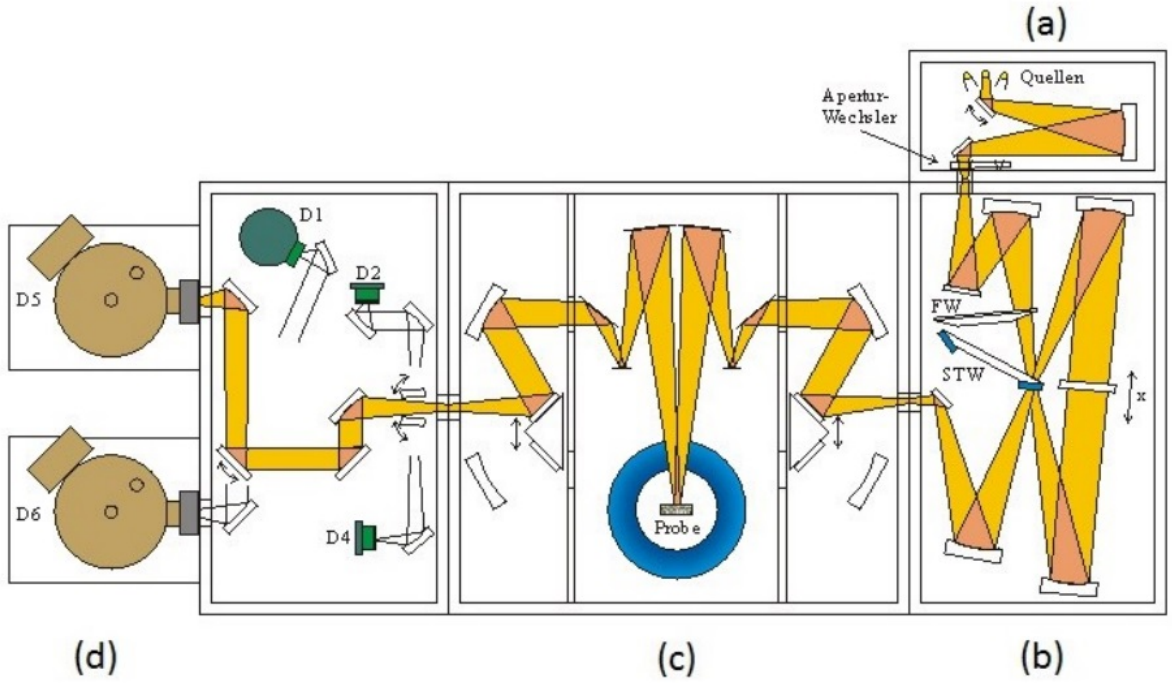

Figure 2.2: FTIR spectrometer BRUKER IFS 113v. (a) chamber with sources of the IR beams, (b) Michelson interferometer, (c) sample chamber, (d) detectors. (figure taken from [46])

and both beams interfere, through the sample chamber (c) in which, the beam is directed through a mirror set to the sample. After transmission or reflection (reflection variant is depicted on the scheme in the Fig. 2.2) of the beam from the sample, the beam comes to detectors (part d). In the FIR and MIR regions we use a pyroelectric detectors made of deuterated triglycine sulfate. For low-temperature FIR studies we use higly sensitive liquid-helium-cooled silicon sensor (bolometer), because optical windows in cryostat strongly reduce the intensity of the IR beam. The difference between the Michelson interferometer in our spectrometer and the scheme in the Fig. 2.1 is that we use the Genzel version of the interferometer where the moving mirror (with amplitude of movement x) is bilateral. In this case, both interferometer arms generate a larger optical path difference, which has a positive effect on the higher spectral resolution of the spectrometer. Also, the beam splitter (beamsplitter - labeled STW in Fig. 2.2) is unique in that way, that it is automatically changeable (6 positions in total). This makes it possible to cover the entire broad IR region. It should also be emphasized that the whole spectrometer is evacuated to a pressure of 10 mbar, because IR radiation is absorbed by water vapour in the air and due to this a noise can appear at vibration frequencies of water vapour. [26]

In our experiment, we used an experimental setup suitable for the determination of the sample reflectivity. To do this, it is necessary to measure the interferogram $S_0(\nu)$ after reflection from the reference mirror instead of the sample (assuming 100 % reflectivity of the metal mirrors) to determine the spectral intensity of the lamp $S_0(\nu)$ and then to measure the interferogram $S_R(\nu)$ after reflection from the sample. The sample reflectivity is then determined as a fraction

$$R(\nu) = \frac{S_R(\nu)}{S_0(\nu)}. \tag{2.9}$$

In the reflectivity measurement configuration, our apparatus allows the sample placement in a cryostat

into which fluid helium or helium vapor flows from the reservoir during the experiment and thus allows the sample cooling down to temperature of approximately 7 K.

2.3 Terahertz spectroscopy

Terahertz (THz) spectroscopy uses radiation with wavenumbers within the interval $\nu = 3 - 100\check{\mathrm{c}}\mathrm{m}^{-1}$. The development of THz measurement methods has been delayed due to the lack (compared to IR spectroscopy) of strong natural sources of THz radiation. The first artificial sources appeared in the beginning of the sixties of the last century and they were based on Backward-Wave oscillators. [28] In recent years, great expansion of the THz spectroscopy was registered as the new measuring technique called *Terahertz time-domain spectroscopy* was invented. The method is characterized by its high phase sensitivity, where the time dependence of the electric component of the THz pulse $E(t)$ can be directly measured using a synchronized optical laser pulse (see more details below). From the $E(t)$, the transmittance spectrum of the material can be obtained directly by Fourier Transform. From this spectrum and the phase shift, both components of the complex refractive index of the sample can be obtained [47], and consequently also complex permittivity and permeability of the sample can be calculated. Unlike the evaluation of IR reflectivity spectra, where we cannot measure the phase shift of the electric component of the puls (beam), the complex spectroscopic quantities can be calculated directly from the measured THz transmittance spectrum. All experiments as well as spectra calculations are performed by home-made software *PK Graph*. [28], [26]

2.3.1 Terahertz pulse generation

Nowadays, several types of THz radiation sources are used in practice. In our experiments we use a source called a photoconductive switch or also a photoconductive antenna whose principle of functioning is captured in the simplified scheme in Fig. 2.3.

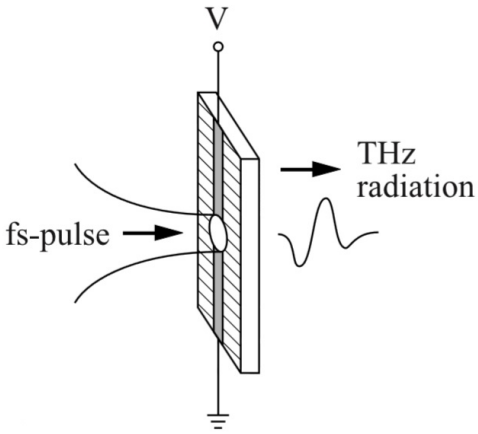

Figure 2.3: Terahertz radiation emitter made from GaAs plate. (figure taken from [28])

The switch made from GaAs is exposed to a linearly polarized, 50 fs long laser pulse. The titanium sapphire laser, we are using, produces pulses (wave packets) with frequency 76 MHz and these are composed of wavelengths from the interval (790; 810) nm. The laser pulse incident to the switch generates free electric charge carriers in it. A DC voltage of 1 kV / cm (actually, rectangular voltage pulses,

the duration of which is 10^6 times greater than the duration of the laser pulse) is connected to the switch and this voltage is oriented perpendicularly to the direction of laser pulse propagation. Voltage begins to accelerate the free charge carriers and generates electrical current in the switch. Gradually, however, the charge carriers are recombined and the current dampened. During the recombination, surplus energy from accelerated carriers radiates in the form of linearly polarized THz radiation. The direction of radiation is identical to the incoming laser pulse. The amplitude of the electrical component of the generated radiation is proportional to the time change of the current density in the GaAs emitter: $\boldsymbol{E}(t) \propto \frac{\partial \boldsymbol{j}}{\partial t}$. As can be seen from Fig. 2.3, the terahertz pulse is a single oscillation. It follows that the wave spectrum composing such a compact wave packet, which is actually only about 1 ps long, is quite wide. The spectrum of the generated THz pulse approximately covers the range of 0.1 – 3.0 THz. [48]

2.3.2 Detection of terahertz puls

At the current stage of development, several accurate methods of THz radiation detection are developed. We use a technique called electro-optic sampling, which is based on the linear electro-optic Pockels effect. In principle, the task of measuring the amplitude of the electric field of the THz pulse is converted to measuring the change of polarization of the laser pulse. It means the determination of the laser intensity in two directions.

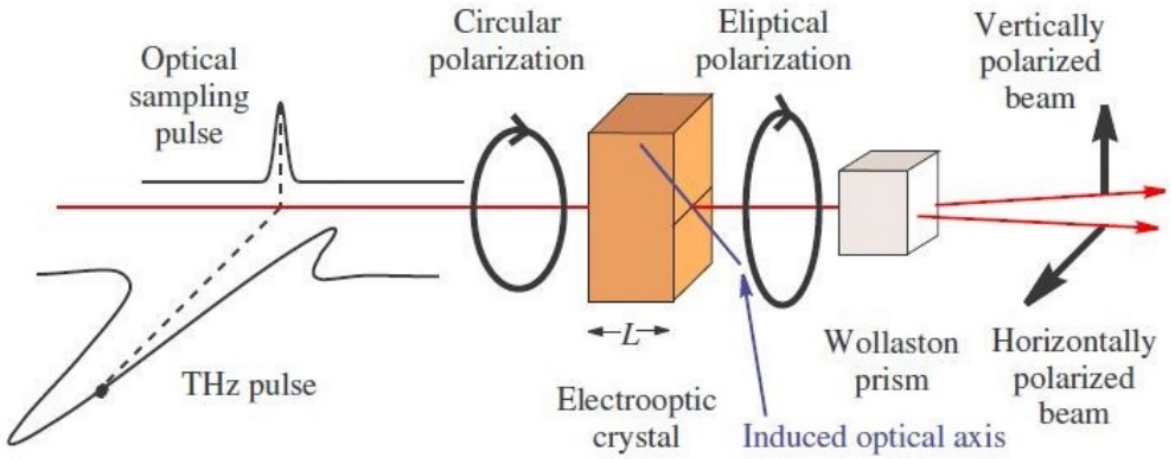

Figure 2.4: Detection of the THz radiation by electro-optic sampling. (figure taken from [26])

The detection scheme is summarized in Fig. 2.4. The linearly polarized laser puls can be converted in the first step to a circularly polarized ray (this step is missing in Fig. 2.4) due to the passage through the quarter-wavelength plate. Change of the polarization from approximately circularly to elliptically polarized ray is more easily detectable than change of the polarization from linear to elliptic. So this step is used for the increase of the detection sensitivity, and therefore we implement it in our experimental setup. Thus prepared laser beam then travels together with (and parallel to) the THz pulse, which is approximately twenty times longer. Both of them go through an electro-optic ZnTe crystal, where the electric field of the pulse causes the birefringence of the laser beam and so changes its polarization to the elliptic. The ellipticity is then determined by separating the component with the vertical and horizontal polarization in the Wollaston prism and by measuring intensities of these components using the photodiode. [26]

In the above mentioned manner, the average magnitude of an electric field of approximately one twentieth of the THz pulse (the laser beam is about twenty times shorter than the THz pulse) is determined. Through a different delaying of the laser beam, it is then possible to reconstruct the shape of the whole THz pulse. The name terahertz time-domain spectroscopy emerged just because of the laser beam delaying. [26]

2.3.3 Transmission measurement using terahertz spectrometer

Our home-made apparatus, which is designed to measure THz radiation after passing through the sample, is schematically captured in Fig. 2.5. Approximately 96 % of the laser beam intensity is used to generate the THz pulse, the remaining part of the laser beam is used as a mediator in the THz pulse detection after passing through the sample. The emitter bias oscillates with frequency of approximately 100 kHz. Terahertz radiation, whose area of occurrence between the emitter and the sensor S is depicted in grey in the diagram, has to pass through a vacuum since the rotational modes of the water vapor contained in the atmosphere lie in the THz range and therefore water vapor absorbs this radiation and causes noise in the spectrum. The sample is placed in the Oxford Instrument Optistat cryostat with a helium atmosphere and mylar windows. Our cryostat allows measurements in the temperature range $5 - 300$ K. Another helium cryostat (Oxford Instrument Spectromag) is additionally equipped with a superconducting magnet, so that in the low temperature measurements (down to 2 K) a homogeneous magnetic field is available up to 7 T. This field may be set either in the direction parallel or perpendicular to the polarization of the THz pulse (Voigt arrangement) or parallel to the direction of the pulse propagation (Faraday arrangement). We have always used Voigt arrangement. [26]

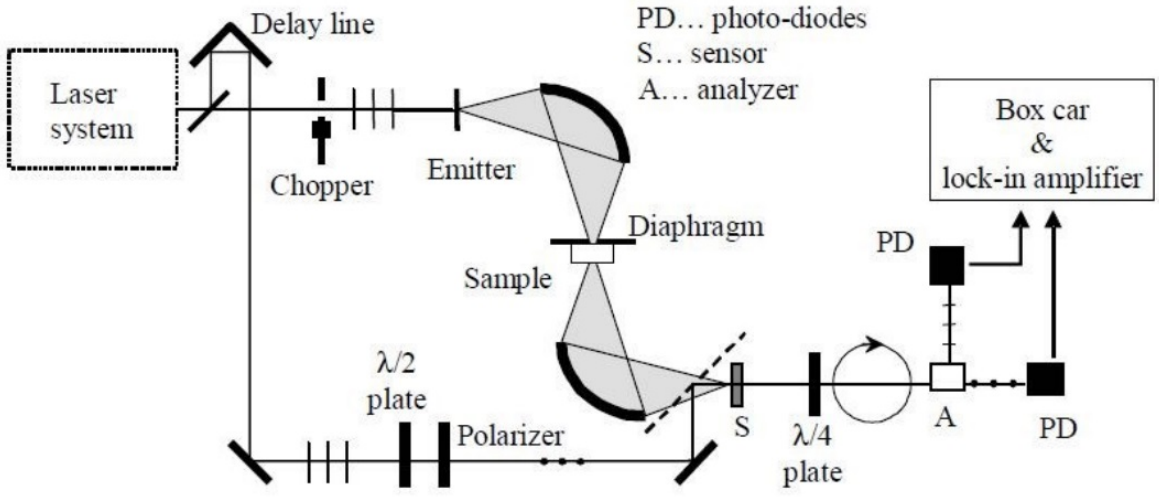

Figure 2.5: Scheme of the THz spectrometer in the transmission mode. (figure taken from [48])

The output of the measurement is the time dependence (otherwise, also the spatial shape) of the THz pulse electric field. This output is then decomposed by inverse Fourier transform into the transmittance spectrum. Sample transmittance, which is determined by the ratio of the signal passing through the sample and the signal passing through the reference hole, and its thickness are subsequently used in the calculation of the complex refractive index, complex permittivity, complex permeability or complex conductivity of the material under investigation. [47], [49]

2.4 Infrared spectra evaluation

When evaluating the measured IR spectra, we use the relation (2.2) for non-magnetic substances, i.e. $\mu_1 = 1$ and $\mu_2 = 0$, which is usually well satisfied in the phonon frequency range. It is clear from this relation that the reflectivity provides only information about the magnitude of complex permittivity and the values of its components ε_1 and ε_2 are obtained only by applying a suitable physical model. Infrared response (permittivity $\varepsilon(\omega)$) can be described by the sum of *Lorentz oscillators* [24], [44]

$$\varepsilon(\omega) = \varepsilon_\infty + \sum_{j=1}^{n} \frac{\Delta\varepsilon_j \omega_{TO_j}^2}{\omega_{TO_j}^2 - \omega^2 - i\gamma_{TO_j}\omega}, \tag{2.10}$$

where three parameters - frequency of IR active TO phonon ω_{TO_j}, its damping γ_{TO_j} and its oscillator strength $\Delta\varepsilon_j\omega_{TO_j}^2$ (here *dielectric strength* $\Delta\varepsilon_j = \varepsilon(0)_j - \varepsilon_\infty$ is contribution of the j-th mode to the static permittivity) - describe each oscillator. Nevertheless, we evaluate data using *four-parameter model* for each oscillator. [50] The reason for this choice is significant frequency splitting between ω_{TO_j} and its corresponding longitudinal mode frequency ω_{LO_j} in $EuTiO_3$. The four-parameter model is more suitable for description of broad reflection bands with large TO-LO splitting. The fitting was performed using the home-made *Wasf* software.

The frequency (ω) dependence of the dielectric complex permittivity can be expressed using a four-parameter model in a form [50]

$$\varepsilon(\omega) = \varepsilon_\infty \prod_{j=1}^{n} \frac{\omega_{LO_j}^2 - \omega^2 - i\gamma_{LO_j}\omega}{\omega_{TO_j}^2 - \omega^2 - i\gamma_{TO_j}\omega}, \tag{2.11}$$

where ε_∞ is the temperature-independent high-frequency permittivity given by the electron transitions, ω_{TO_j} and γ_{TO_j} are the frequencies and damping of the j-th transverse phonon, ω_{LO_j} and γ_{LO_j} mark the frequency and damping of the j-th longitudinal phonon corresponding to the j-th transverse mode. ω_{TO_j} and ω_{LO_j} fulfill inequality $\omega_{TO_j} < \omega_{LO_j}$. In addition, the prescription of the function $\varepsilon(\omega)$ tells us, that for frequencies equal to ω_{TO_j} the dielectric losses curve $\varepsilon_2(\omega)$ has local maxima and the real permittivity curve $\varepsilon_1(\omega)$ inflection points. The curve $\varepsilon_1(\omega)$ has zero values at points ω_{LO_j}. [50], [44], [23]

By setting the frequency $\omega = 0$ in equation (2.11), the complex permittivity becomes only real (ε_∞ is also a real number), and this equation transforms into the Lyddane-Sachs-Teller relation (Eq. (1.6)). Furthermore, the contributions of the j-modes to static permittivity $\Delta\varepsilon_j$ (where $\Delta\varepsilon_j = \varepsilon(0)_j - \varepsilon_\infty$) is restricted by the sum rule

$$\sum_{j=1}^{n} \Delta\varepsilon_j \omega_{TO_j}^2 = konst., \tag{2.12}$$

which describes the force equilibrium in the crystal and is fulfilled at each temperature. [50], [51] The $\Delta\varepsilon_j$ contributions can be calculated using LO_j and TO_j frequencies through the formula [50]

$$\Delta\varepsilon_j = \varepsilon_\infty \omega_{TO_j}^{-2} \frac{\prod_k \left(\omega_{LO_k}^2 - \omega_{TO_j}^2\right)}{\prod_{k\neq j} \left(\omega_{TO_k}^2 - \omega_{TO_j}^2\right)}. \tag{2.13}$$

If the material is not a good dielectric and shows a nonnegligible conductivity, the free carriers of the electric charge contribute to the dielectric function (i.e. to the relation (2.11)) through the Drude term

[52]

$$\varepsilon_D(\omega) = \frac{\omega_p^2}{-\omega^2 + i\omega\gamma_0}, \tag{2.14}$$

where ω_p is the plasma frequency of the free carriers and γ_0 is the plasma damping. ω_p is proportional to the free-carrier density n and inverse-proportional to free-carrier effective mass m^* using relation $\frac{4\pi ne^2}{m^*}$.

2.5 Radio-frequency dielectric spectroscopy

Radio-frequency spectroscopy serves as a sample characterizing method for low frequency dielectric permitivity and conductivity. This technique measures the impedance (or capacity) of the sample, which is shaped to the form of a thin plate with elecrodes (the thickness of the sample is typically from 100 μm to 1 mm), and subsequently the real and imaginary component of permitivity or conductivity is calculated from the determined impedance. With our experimental setup produced by Cryogenic company [53], we are able to determine low-frequency dielectric properties of the sample in magnetic field up to (theoretically) 20 T and simultaneously in the low-temperature regime with the lowest temperature of 0.3 – 0.4 K (this requires ^{3}He cooling system). The frequency range of our impedance analyzer (Alpha-AN from Novocontrol company) is from 0.001 Hz to 1 MHz. In this frequency domain, there are no optical phonon excitations in the sample, but the radio-frequency electric field influences the polarization of the atoms or molecules inside the substance. Under assumption that the polarization (in this case the translational polarization caused by the translation of the whole atoms) of the substance decreases after turning off the outer field exponentially as $e^{-\frac{t}{\tau}}$ (polarization behaves as a displacement of the damped oscillator), where τ is the so-called relaxation time, it is possible to express the sample permittivity dependence on a frequency of the applied electric field by the Debye's relaxator [23], [54]

$$\varepsilon(\omega) = \varepsilon_\infty + \frac{\varepsilon(0) - \varepsilon_\infty}{1 + i\omega\tau}, \tag{2.15}$$

in which ε_∞ is the high-frequency permittivity, i.e. permittivity caused by effects at far higher frequencies than is the frequency range of radio waves (ε_∞ is in this case the sum of electron and phonon contributions to permittivity) and $\varepsilon(0)$ is static permittivity. The previous relation can be generalized to the sum of any number of relaxators (when the polarization of different atoms or molecules in a substance is characterized by different relaxation times) simply by adding a summation over all τ_j before a fraction or by transition to integration over a possible interval of the relaxation times. Debye's relaxator is used as a model for fitting radio-frequency spectra.

2.6 Capacitance dilatometry

Dilatometry includes measurement methods that focus on detecting sample sizes and their changes under varying external conditions. The dimensions of the sample typically change due to thermal expansion, magnetostriction, electrostriction etc. To determine the magnetostriction in $EuTiO_3$ we choose the so-called capacitance dilatometry based on the principle of capacity measurement of the the sample holding device whose dimension is proportional to sample dimension change. The holder, which is called microdilatometric cell, used in our experiments is schematically shown in Fig. 2.6. This particular cell was primarily designed for the study of magnetic phase and magnetic phase transitions. The author of the cell is Jan Prokleška from the FMP CU, who also performed magnetostrictive experiments, namely in the joint magnetic laboratory of Physical Institute and Charles University in Prague-Troja. [55]

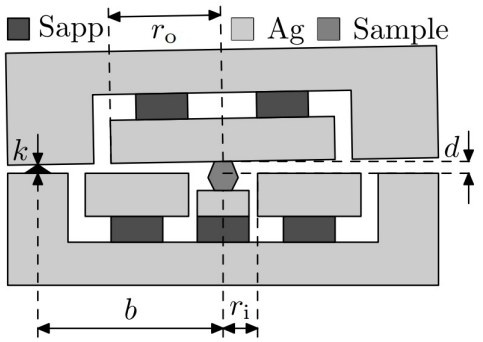

Figure 2.6: Schematic diagram of the used dilatometric cell. (figure taken from [55])

Dilatometric cell is almost entirely made of silver due to its use in experiments with magnetic field. The main advantage of silver is its diamagnetic nature, but it has also lower heat capacity than copper, and it is characterized by zero nuclear magnetic contribution at low temperatures and high magnetic fields. The sample is placed in the internal cavity of the cell with dimensions of about $3 \times 3 \times 3$ mm. The cell is constructed in the so-called tilted-plate arrangement, where the sample pushes on a plate that is fixed on one side and loose on the other. The dilatation or contraction of the sample then causes the plate rotation around the fixed point k and thereby a change of the cell opening magnitude (see Fig. 2.6). The cell opening change has a direct effect on a change of the system capacity C. The capacity of the used dilatometer cell is given by relation [55]

$$C(T,H) = \frac{2\varepsilon_0}{d(T,H)} \left(A_o(T) \frac{1 - \sqrt{1-\gamma_o^2(T,H)}}{\gamma_o^2(T,H)} - A_i(T) \frac{1 - \sqrt{1-\gamma_i^2(T,H)}}{\gamma_i^2(T,H)} \right), \tag{2.16}$$

where $A(T)$ and $\gamma(T,H)$ are functions of the cell's geometric parameters (the indices o and i express the relation to the parameters r_i and r_o in Fig. 2.6), ε_0 marks the vacuum permittivity and $d(T,H)$ marks the dimension of that part of the sample that protrudes from the sample cavity and so pushes to the revolving plate. However, it is appropriate to add that $\gamma(T,H)$ function is also a function of $d(T,H)$, so it is necessary to solve the equation (2.16) with respect to $d(T,H)$ numerically (after the measurement of the capacity C). Once the size of the protruding part of sample $d(T,H)$ as the function of temperature and magnetic field is determined, it is necessary to calculate the actual relative change of the sample size $\left(\frac{\Delta l}{l}\right)_s$ in the given direction with respect to the expansion of the dilatometric cell itself. The recalculation is performed according to the formula [55]

$$\left(\frac{\Delta l}{l}\right)_s = \frac{1}{l_s}\left(\Delta d_s + \Delta d_{\mathrm{Ag}\ s}\right) + \left(\frac{\Delta l}{l}\right)_{\mathrm{Ag}}, \tag{2.17}$$

in which $\left(\frac{\Delta l}{l}\right)_{\mathrm{Ag}}$ represents the silver expansion, and term $\frac{\Delta d_{\mathrm{Ag}\ s}}{l_s}$ indicates the expansion of the silver sample in the calibration measurement. The calibration of the apparatus using a silver sample, whose size exactly corresponds to the size of the sample cavity, allows the construction aspects of the dilatometric cell to be taken into account (for example, the fact that the cell is not entirely made from pure silver). [55]

The arrangement of the inclined plate is particularly advantageous when measuring irregular samples, its disadvantages are complicated data evaluation and difficult calibration of the apparatus. Used apparatus allows simultaneous measurement of cell temperature and capacity. Sample dimensions can be

measured in two orientations with respect to the magnetic field, namely perpendicular and parallel to it. Cell capacity is measured by the Andean-Hagerling AH2500A capacitive bridge. The physical conditions of the sample environment (temperature, pressure, magnetic field) are fully controlled by the PPMS (*Physical Property Measurement System*) from Quantum Design [56] company. The lowest achievable temperature in this device is about 1.9 K and the highest possible magnetic field is approximately 9 T. [55]

2.7 Magnetic properties measurement

For determination of the induced magnetization in our $EuTiO_3$ samples also PPMS was used. PPMS device determines the magnetization of the material using measuring technique based on electromagnetic induction. In such an arrangement, the induced voltage in the coils through which the sample is moved is registered. Practically, the movement of the sample can be either periodic or simple - away from the coils. The movement of the sample is periodic in PPMS apparatus, so it is a so-called *vibrating sample magnetometer*. The magnetisation is calculated from the proportionality equation between the induced voltage U on the pickup coils and the change of the magnetic flux density B [55]

$$U = -\frac{\mathrm{d}\Phi}{\mathrm{d}t} \approx \frac{\mathrm{d}B}{\mathrm{d}t}. \tag{2.18}$$

Here Φ stands for magnetic flux and t for time. Magnetization M is calculated from the measured B and known magnetic field strength H using relation [55]

$$B = \mu_0(M + H), \tag{2.19}$$

where μ_0 denotes the permeability of vacuum.

In the PPMS apparatus the housing consisting of the drive and detection coils, thermometer and standard electrical interface is placed inside the PPMS chamber allowing usual field and temperature control. The sample itself is fixed to a long thin rigid rod connected to a DC servo motor outside the sample chamber. This setup allows longitudinal movements through the pick-up coils. The sample translation is synchronised with data acquisition. The magnetic moment is obtained by numerical integration of the measured voltage profile and fitting of the obtained waveform to the known data for a dipole moving through the detection coils. The homogeneity of the magnetic field across the measuring region is achieved with an accuracy of 0.01 %. Samples were carefully fixed in order to avoid possible rotation or undesirable displacement due to the magnetic forces acting during the experiment. [55]

Chapter 3

Measurement results

3.1 Preparation of the samples

All measurements were performed on $EuTiO_3$ ceramics, i.e. samples with a polycrystalline structure. A typical feature of polycrystalline samples is their macroscopic (both dielectric and optical) isotropic behavior. This is due to the fact that the individual crystallites are randomly oriented in space and, moreover, their dimensions are much smaller (in the order of tenths of a μm in our samples [57]) than the total probed volume of the sample (diameter of incident beam is typically in the order of millimeters). Then, in the case of spectroscopic experiment, the incident beam strikes a statistically sufficient amount of grains to make all directions in the sample structurally equivalent. The disadvantage of polycrystalline structures over single crystals is the presence of a considerable amount of structural defects (mainly at grain boundaries) and open and also closed pores, which then affect the macroscopic properties of the sample. Relevant parameters in determining the quality of ceramics are relative density, porosity, amount of oxygen vacancies, and purity (to what extent it is a single phase ceramics). The infrared reflectivity of ceramics increases with its increasing density (the sample contains less pores and thinner grain boundaries, i.e. less structural defects), therefore it is desirable to produce as dense as possible ceramics, whose physical properties are close to those of single crystals.

Preparation of samples was provided by M. Kachlík from the Brno University of Technology, who has several years of experience with the synthesis of $EuTiO_3$ ceramics. The $EuTiO_3$ ceramics were prepared from two commercially available powders - Eu_2O_3 (99, 99 % purity, 100 nm grain size) and anatase A-TiO_2 (99, 99 % purity, 100 nm grain size). The aim was to produce $EuTiO_3$ according to the chemical equation

$$Eu_2O_3 + 2TiO_2 + H_2 \longrightarrow 2EuTiO_3 + H_2O.$$

Unfortunately, thermodynamic data are not yet available to calculate the Gibbs free energy of the above mentioned chemical reaction. Thus, the ideal reaction conditions are not known and, moreover, the most suitable way of post-treatment of $EuTiO_3$ powder is also not known. Therefore, preparation of the densest and purest $EuTiO_3$ ceramics is more or less based on experience and synthesis under various reaction conditions. [57]

The ceramics preparation itself begins with the homogenization of the reactants mixture. This homogenization was performed either in a so-called *planetary mill* (for 30 minutes) or in a so-called *ball mill* in polypropylene bottles (for 48 hours). Ethanol is added to the mixture as a medium during homogenization. The difference between these two grinding techniques is in the grinding energy. The planetary

mill operates faster and at very high grinding energy. Consequently, the resulting mixture can be contaminated by a trace amount of the substances the mill is made of (ZrO_2, MgO etc.). On the other hand, the polypropylene bottles can contamine the mixture even at low-energy grinding performed in the ball mill. The mixture used for the preparation of the sample #1 was homogenized in planetar mill, whereas the mixture for the sample #2 and #3 preparation was homogenized in the ball mill. The resulting homogeneous suspension is subsequently dried and triturated in a ceramic mortar. The resulting powder is annealed in a 99, 9 % hydrogen atmosphere (pressure 95 kPa) at 1100 °C for three hours with a gas flow of 5 l/min (heating speed 20 °C/min; cooling speed 20 °C/min). Subsequently, the preparation procedures of individual ceramics differ.

Further preparation of samples #1 and #3 differed very little. Both were sintered at SPS (Spark Plasma Sintering) device. Sintering was carried out in the vacuum (with multiple nitrogen washing) at 1300 °C with a duration of 5 min (heating speed 100 °C/min; cooling speed about 50 °C/min was managed by manual power control). Sample shapes were formed during the sintering. At this stage, the annealed powder was placed in a piston that compressed it, and electrical discharges resulting from the applied electrical voltage sintered the powder into a compact polycrystalline body. Preparation of the sample #2 differed significantly. The powder was first compressed in a piston using a 10 MPa uniaxial pressure and then subjected to cold isostatic pressing at 1 GPa. Subsequently, so prepared "green body" was placed in a hydrogen furnace, where was "baked" 120 min in 99, 99 % argon atmosphere at 1400 °C (heating and cooling speed 10 °C/min). Thus prepared disc-shaped samples were then sandblasted and ground to remove surface admixtures and impurities (especially graphite).

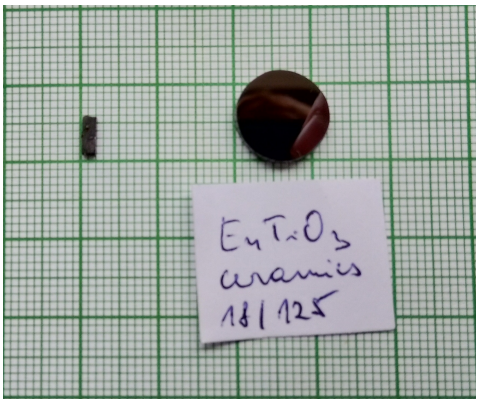

Figure 3.1: **Left sample:** The 1.5 × 1.5 × 5 mm big cuboid cut out of the original sample #2 and intended for magnetization measurement. **Right sample:** The polished disc-shaped sample #3 used in IR experiments (laboratory designation 18/125).

The prepared samples were opaque, dark gray to black in color and cylindrical (disc-shaped) with diameter of ∼ 7 – 14 mm and with thickness of ∼ 4 mm (see rigth sample in the Fig. 3.1). Each sample was cut into pieces of the desired thickness for experimental purposes, and some of them were then carefully polished in the optical workshop to avoid the scattering of incident radiation on their surfaces during spectroscopic measurements. In all the IR experiments, several milimeters thick polished disc-shaped samples were used (right sample in the Fig. 3.1). For the THz experiments, 100 μm thick (transmission type of spectroscopic measurement) disc- (sample #1) or half-disc-shaped (sample #2) samples were cut and subsequently also polished. From the sample #1, a 1 × 1 × 2 mm big cuboid, which was used in the magnetostrictive measurement, was cut out. Significantly more elongated cuboid (1.5×1.5×5 mm)

was also cut out of the sample #2. This cuboid is caught in the Fig. 3.1 and was used for the magnetization measurement. In all the radio-frequency measurements, approximately 1 mm thick half-disc-shaped samples were used. These were also cut out of the original thick discs and then were provided by circular golden electric contacts (prepared through deposition) with $\sim$ 5 mm diameter.

The density of the samples was calculated by the Archimedes method. Relative densities were calculated using the theoretical density (TD) of $EuTiO_3$ ceramics 6.91 g·cm^{-3}. Thus performed calculations of relative densities of our ceramics gave values 98.0 %, 93.2 % and 98.9 %, respectively. The phase composition of the samples was determined by X-ray diffraction (XRD) analysis using a cobalt radiation source ($Co_{K\alpha 1}$, λ = 1.78892 Å). [57] XRD analysis showed single phase $EuTiO_3$ samples (no secondary phases were detected). As a supplementary measurement was performed coarse determination of sample #1 resistance. Manual measurement of surface resistance using a multimeter gave values in kΩ region.

3.2 Sample characterization

3.2.1 Structural characteristics

At first, we intented to perform X-ray texture analysis on sample #1. The measurement was kindly carried out by Jan Drahokoupil on the X'Pert PRO diffractometer from PANalytical company. However, due to the relatively small size of the sample, it was necessary to use a point focus with the $0,25 \times 1$ mm slit. It turned out, that only a small number of crystallites were present in the irradiated volume due to the use of a small aperture, and therefore the texture analysis could not be reliably performed. The considerable coarseness of the sample is well documented by the backscatter diffraction image (Fig. 3.3), on which the discontinuity of the diffraction lines is clearly visible (the size of line trace of the incident beam on the sample was approximately $2 - 3$ mm). The size of the grains was roughly estimated in the order of tens of μm. For the verification of the estimation, a microscope photograph of the sample #3 polished surface was taken. The photograph is depicted in Fig. 3.2. There are clearly visible grain boundraies (the black traces) which contain microscopic cavities. It seems that the biggest grains reach the size of approximately 100 μm, while the approximate grain size average moves around 50 μm. A rough estimation emerging from X-ray analysis is thus in agreement with Fig. 3.2.

It seems, that the image 3.3 does not indicate the presence of any texture (traces in diffraction lines are practically dots and randomly situated). However, due to the coarseness of the sample, the quantitative texture analysis is not possible. Therefore, we have evaluated the diffraction data of sample 17/13, which was measured within my Bachelor thesis and whose dimensions allow the use of 15 mm long and 1° wide line aperture [11] (corresponds to 2 mm wide trace on the sample). The texture of this sample was estimated by calculating the texture index $T(h_i)$ for each reflection h_i according to relation [58]

$$T(h_i) = \frac{\frac{I(h_i)}{R(h_i)}}{\frac{1}{n}\sum_{j=1}^{n}\frac{I(h_j)}{R(h_j)}}, \tag{3.1}$$

which can be used for slightly textured polycrystalline materials. In this formula, n represents the total number of diffraction lines, $I(h_i)$ stands for the measured intensity of the line h_i and $R(h_i)$ is the theoretically calculated intensity of this line in a perfectly non-textured polycrystalline sample. The calculation of $R(h_i)$ is based on the $EuTiO_3$ lattice parameters, which are, for example, included in the X'Pert PRO diffractometer software. The calculated $T(h_i)$ values of sample 17/13 are for all reflections h_i more or less distributed around the value 1, which indicates a completely non-textured sample. [58] The most distant

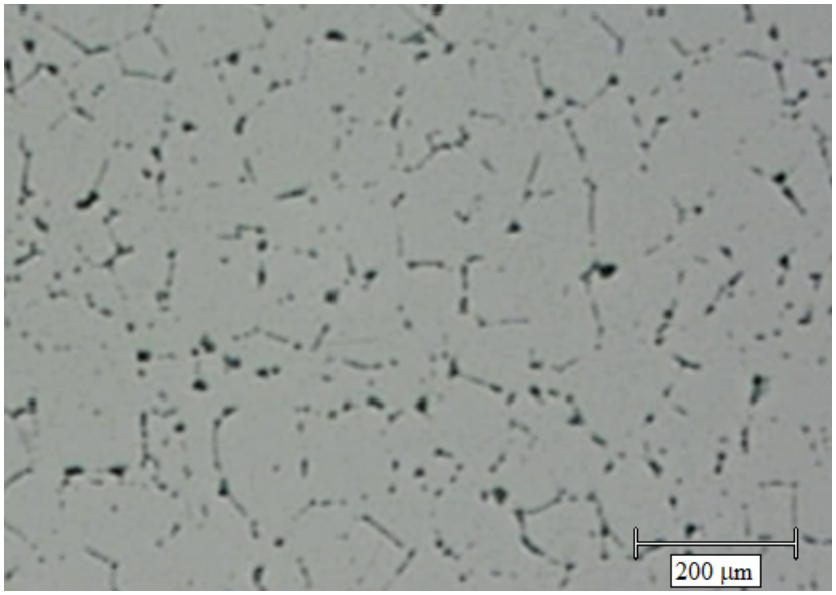

Figure 3.2: The magnified photograph of the sample #3 polished surface taken by an optical microscope. The black traces indicate grain boundaries, which often contain large defects leading to a creation of small cavities (porosity).

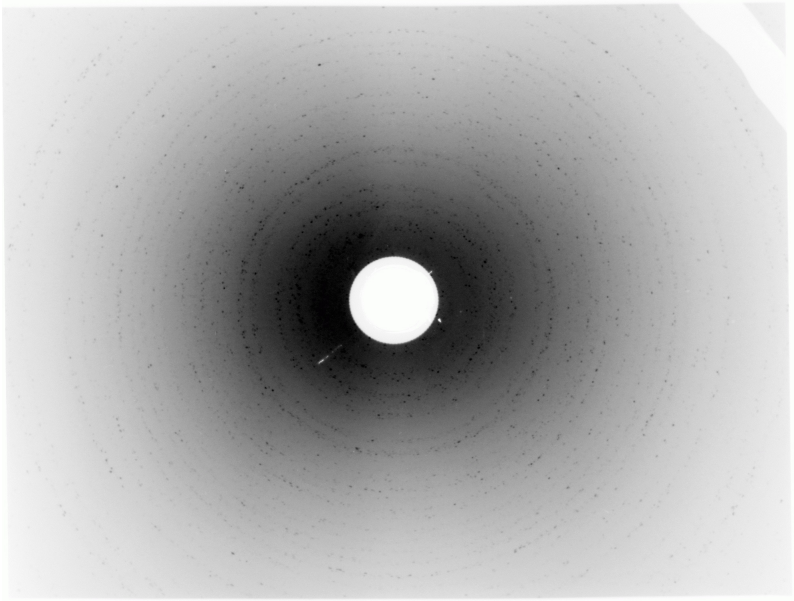

Figure 3.3: Diffraction backscatter image of the sample #1 taken using a 55 kV and 30 mA molybdenum lamp (λ = 0.7107 Å). The sample - film distance was set to 40 mm and the exposure took 150 s. A collimator with 1 mm diameter was used.

values of $T(h_i)$ from 1 are numbers 1.28 corresponding to the reflections on the planes (2 2 2), (0 0 4), and 0.72 corresponding to the reflections on the planes (2 2 1), (0 0 3). Typical $T(h_i)$ values for textured materials are numbers greater than 3. Then the calculation indicates that the sample 17/13, which was subjected to uniaxial 20 MPa pressure during the fabrication, is apparently non-textured. Small devia-

tions of the texture indexes from 1 are probably caused by the coarseness of the sample (despite the usage of line focus). We can also conclude, that other samples, which were made using a comparable uniaxial pressure, are also non-textured, and thus isotropic.

The coarseness of the sample forces to reflect on the legitimacy of using an approximation of polycrystalline sample. We conclude, that several mm^3 big ceramics (as is typically used in magnetization and magnetostriction measurements) consists of more than 10^4 grains even in the case of 50 μm (estimated average) large grains. At the same time, 10^4 grains is affected in spectroscopic measurements (when approximately 5 mm aperture is used) and this is also true for measurements in the radio-frequency range. It follows that the ceramics used in our experiments can be considered (from the structural point of view) as isotropic.

3.2.2 Electric conductivity

One of the most common and major deficiencies of $EuTiO_3$ ceramics is their various electric conductivity. It is a consequence of the sample preparation process and is likely and predominantly caused by the formation of oxygen vacancies either within individual grains of the ceramics or most probably at the grain boundaries. So actually $EuTiO_{3-x}$ is synthesized during sample preparation, instead of pure $EuTiO_3$. $EuTiO_{3-x}$ then contains excess of only weakly bound electrons causing the enhanced conductivity. Couple of years ago, Dr. Jiříček from the Physical Institute investigated three various $EuTiO_3$ ceramics (namely those characterized within my Bachelor thesis) with small, medium and high conductivity and found that the conductivity is proportional to concentration of oxygen vacancies. Simultaneously, the oxygen vacancies are responsible for change of Eu^{2+} to Eu^{3+} and Ti^{4+} to $Ti3+^{3+}$. Therefore, it is important to work with the most dense ceramics with a minimum of structural defects and thus the lowest conductivity. The enhanced low-frequency conductivity of ceramics is unpleasant for several reasons. In the IR region, the free carrier plasma partially screens the phonon response and therefore the fitting of the measured spectra is complicated. In the THz transmission experiment, the free carrier plasma significantly reduces the intensity of the transmitted signal and thus increases the experimental error. Moreover, in the radio-frequency region it even contributes to the effective permittivity of the sample. Hence, we subject each ceramic to radio-frequency experiments without magnetic field to determine the conductivity and thus the quality of the ceramics. Over the past couple of years, our $EuTiO_3$ ceramics have undergone significant decrease in conductivity. Even within my Bachelor thesis [11] we measured samples, where we identified significantly enhanced conductivity, which made it impossible to correctly evaluate the phonons from the measured IR spectra.

The radio-frequency measurement results of the sample #1 are captured on the right side of Fig. 3.4. For comparison, the radio-frequency conductivity of sample #17/13 (this number comes from my Bachelor thesis [11]) is captured on the left side of the same image. This sample was the most promising ceramic measured within my Bachelor thesis, because it was well transparent in THz region. Obviously, there is a qualitative difference in the temperature dependence of the low-frequency conductivity σ_1 between the two samples. While the sample #17/13 conductivity exhibits metallic behavior, i.e. it increses on cooling, sample #1 behaves as a dielectric with decreasing conductivity on cooling. Interestingly, the sample #1 is more conductive at room temperature, but its conductivity is about three orders of magnitude smaller at 10 K (measured below 10 kHz). We consider this to be a huge forward shift, as we are particularly interested in the low temperature region below 10 K.

Although the conductivity of the sample #1 was reduced by several orders of magnitude compared to the sample 17/13, its behaviour still cannot be considered as of an ideal insulator. The enhanced

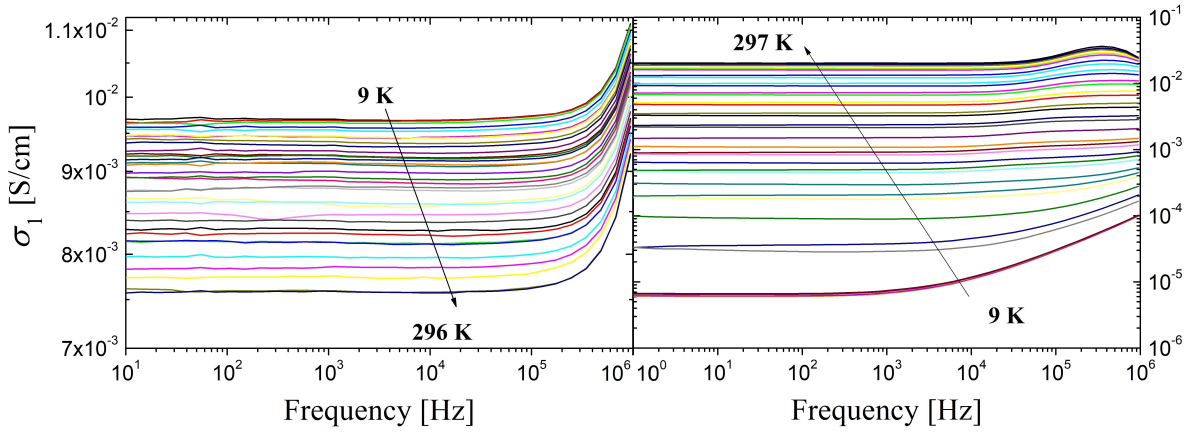

Figure 3.4: **Left:** Frequency dependencies of the electric conductivity σ_1 (calculated from equation (1.13)) of the sample #17/13 and **Right:** the conductivity of the sample #1 in radio-frequency range. Frequency dependencies were obtained in temperature interval 9 – 297 K.

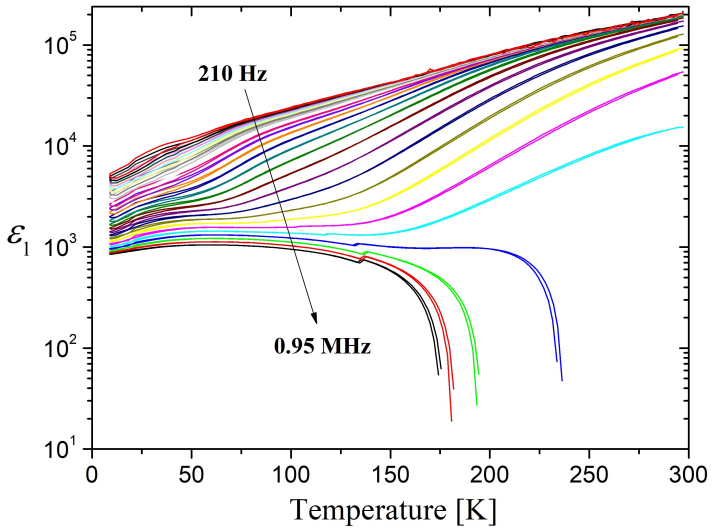

Figure 3.5: Temperature dependences of the sample #1 permittivity ε_1 measured from 210 Hz to 0.95 MHz. All lines are doubled as one always corresponds to data collection during cooling and the other during heating.

conductivity of the sample still manifests itself at very low frequencies of the electric field even at low temperatures below 10 K. This is illustrated by the temperature and frequency dependence of the permittivity at frequencies below 1 MHz (see Fig. 3.5). The data was obtained by radio-frequency spectroscopy. In the case of a good non-conductive $EuTiO_3$ sample, the permittivity should decrease with increasing temperature (up to about 80 K) according to the data shown in Fig. 1.11 and as it has been shown by Katsufuji and Takagi on $EuTiO_3$ single crystal [3]). The permittivity increase at low frequencies (see Fig. 3.5) is caused by the finite conductivity of the sample (the abrupt decrease of the permittivity seen above 150 K at freqencies near 1 MHz is probably only an artifact of the measurement). Due to the conductivity, Maxwell-Wagner polarization occurs and it is manifested by a dielectric relaxation in radio-frequency region. [59], [60]

Relaxation is ensured by free electrons that move (when the electric field is applied) to the positive electrode, resulting in a charge depletion layer near the negative electrode. Thickness d^* of the depletion region is significantly smaller than the thickness of the entire sample d. Then only this layer effectively contributes to the permittivity of the sample, resulting in an increase of the sample capacity (capacity is calculated using the relation for plate capacitor $C = \frac{\varepsilon_0 \varepsilon_1 S}{d}$ and substituing d^* instead of d). [59] However, the experimental setup assumes a contribution to permittivity from the entire sample volume, and therefore an increase in the sample capacity is interpreted as an increase in its permittivity. Above mentioned mechanism dominates in slightly conducting single crystals. In ceramics, additional contribution to capacity comes from interlayer capacitors present at the grain boundaries. [60] For that reason, in ceramics both depletion layers near electrodes and grain boundaries enhance electric capacity of the samples and cause huge effective dielectric permittivity at low frequencies.

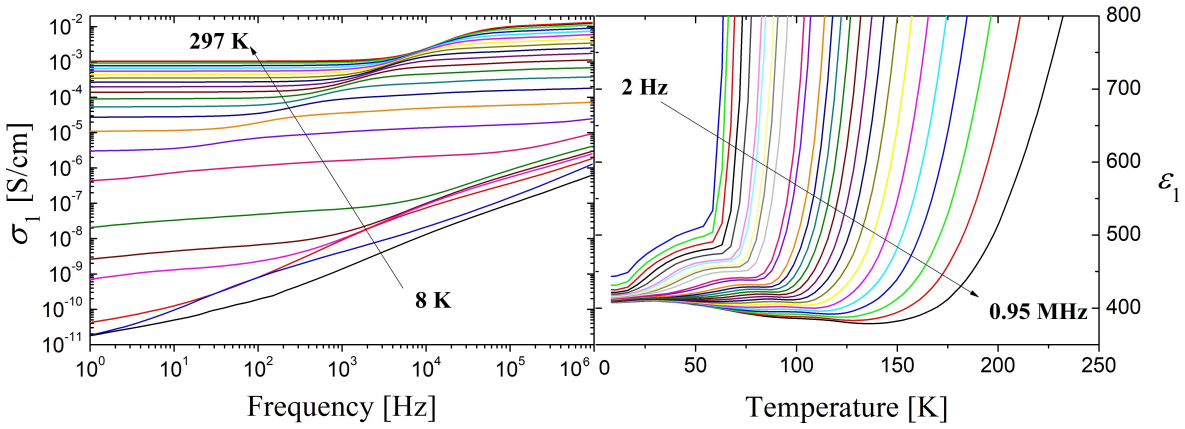

Figure 3.6: **Left:** Radio-frequency electric conductivity σ_1 (calculated from equation (1.13)) of the sample #2 in temperature interval 8 – 297 K. **Right:** Temperature dependencies of the permittivity ε_1 measured at frequencies from 2 Hz to 0.95 MHz.

As shown in Fig. 3.6 and 3.7, samples #2 and #3 are even few orders of magnitude less conductive than ceramics #1. Sample #2 conductivity contribution to its low-frequency permittivity (at temperatures below 10 K) is within the range of 2 Hz - 0.95 MHz only about 10 %. This is again one order of magnitude shift in comparison with the ceramics #1, whose permittivity rises five times at the lower limit of the 210 Hz - 0.95 MHz interval. It is clearly visible, that the preparation of the samples is extremely sensitive to the each step of the procedure. Although the sample #1 and #3 preparations are almost identical (differ only in the reactant mixture homogenization), their conductivities differ significantly.

From the permittivity of ceramics #2 in Fig. 3.6 we can assume that if we measure low-frequency permittivity on this sample in an external magnetic field and for electric field frequencies higher than 1 kHz, then the conductivity contribution can be considered negligible, and therefore sample #2 could be reliably used to this type of experiment. However, ceramics #1 and #3 could be used without much difficulty in THz and IR measurements where the conductivity contribution is significantly lower. The temperature dependencies of the permittivity in the Fig. 3.5 and 3.7 deserve a small comment. Anomalous decreases in permittivity for the highest measured frequencies compared with curves measured at lower frequencies are likely only consequencies of measurement inaccuracies.

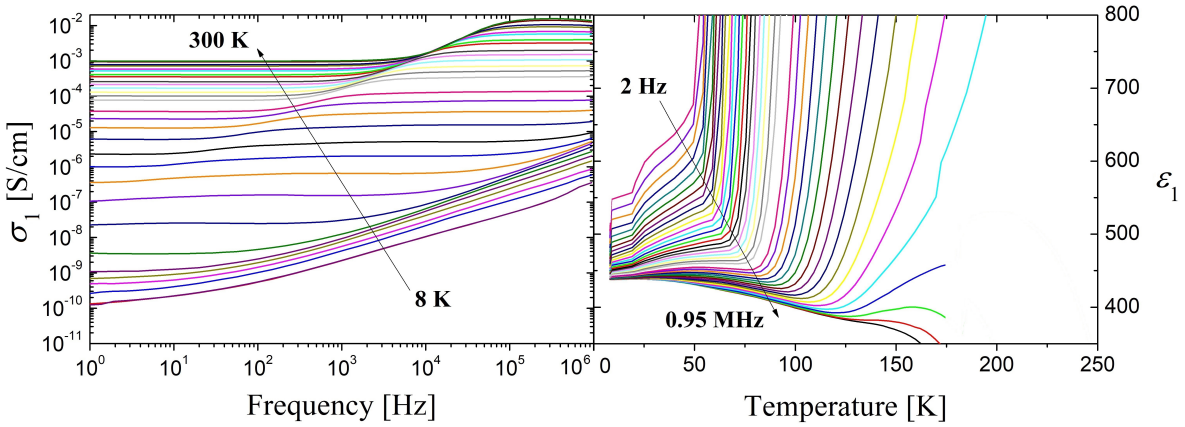

Figure 3.7: **Left:** Radio-frequency electric conductivity σ_1 (calculated from equation (1.13)) of the sample #3 in temperature interval 8 – 300 K. **Right:** Temperature dependencies of the permittivity ε_1 measured at frequencies from 2 Hz to 0.95 MHz.

As illustrated above, our samples have undergone enormous improvements. The question is whether there is still a space for conductivity reduction. We can see that with increasing temperature (above 10 K) the permittivity starts to rise steadily due to the enhanced conductivity and the rise is even much steeper above 50 K. Thus, the conductivity is still not negligible when comparing, for example, Fig. 3.6 with the results in Fig. 1.11 or with the results of $EuTiO_3$ single crystal [3]. Differencies likely spring from different types of $EuTiO_3$ samples. Polycrystalline samples are always more conductive than monocrystals due to the high amount of grain boundaries that work as conductive channels. Ceramics are then more conductive than large grain polycrystalline materials for the same reason. Our ceramics, although very dense (over 93 %), still contain only several tens of micrometers big grains (see Fig. 3.2) and therefore also a large amount of their boundaries, which are highly conductive. This is also the reason why the polycrystalline sample in Fig. 1.11 shows a much smaller conductivity contribution (at higher temperatures - above 10 K) to permittivity than our ceramics. Thus, although the $EuTiO_3$ ceramics production process has been significantly improved and the conductivity caused by the oxygen vacancies within the individual grains has been likely almost eliminated, a further significant improvement of the dielectric properties of $EuTiO_3$ ceramics will be very difficult due to the ceramic character of the samples alone.

3.3 THz and IR spectroscopy

Our effort to observe the anisotropy of permittivity in $EuTiO_3$ ceramics was started by THz measurement of complex permittivity down to helium temperatures and with zero external magnetic field. The obtained spectra shown in Fig. 3.8 and 3.9 give information about the quality of the samples and also serve (as will be shown later) as a basis for IR spectra normalization. In all THz experiments, thin disc- or half-disc-shaped samples (about 100 μm thick) cut from the original several mm thick discs were used (see Preparation of the samples).

It can be seen from the data in Fig. 3.8 and 3.9 that the permittivity ε_1 and also the dielectric losses ε_2 increase with cooling. The increase in ε_1 is due to soft mode softening, as discussed previously. Note that the absolute value of ε_1 of sample #1 is generally a few tens of percent greater than the permittivity ε_1 of the sample #2. This is caused by a unequal density of both ceramics (about 5 % difference), but the main reason is different electric conductivity of both samples. As discussed in the section Electric

conductivity, sample #1 has several orders of magnitude higher conductivity than the other two ceramics, and this conductivity contributes to permittivity ε_1 through dielectric relaxation. Obviously, increased conductivity influences ε_1 and ε_2 also in the THz region. Furthermore, it can be seen that the spectra of the sample #1 were measured in the broader frequency region (at higher temperatures) than spectra of the sample #2. It is caused only by the experimental conditions, namely by the intensity of the detected signal, which decreases significantly just at frequencies above 30 cm^{-1}, when the $EuTiO_3$ is measured. In the case of sample #1, the measuring apparatus was adjusted good enough, so that the signal was strong even above this threshold.

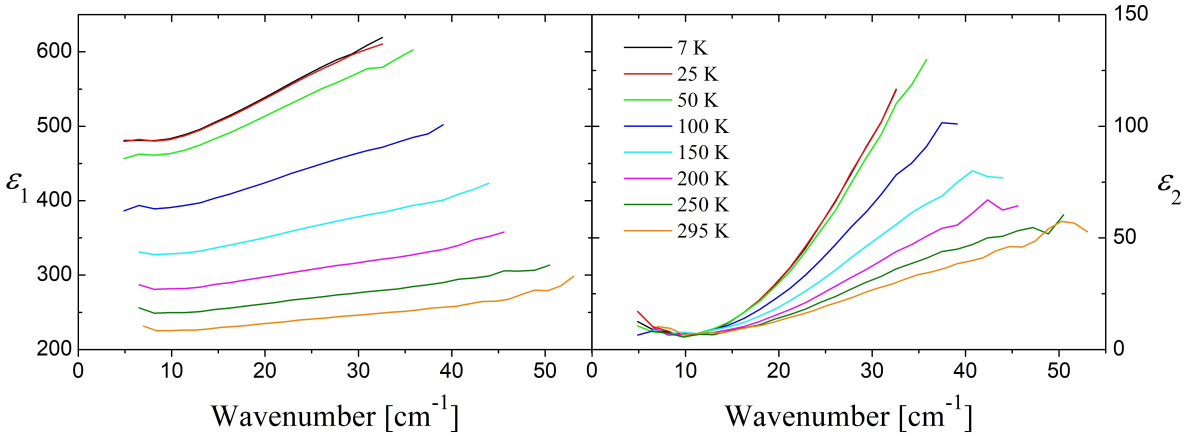

Figure 3.8: THz permittivity spectra of the sample #1 in temperature range 7 – 295 K and zero external magnetic field. **Left:** Real part ε_1 of the complex permittivity. **Right:** Imaginary part ε_2 of the complex permittivity.

Due to limited experimental time with magnetic cryostat, we measured magnetic-field dependence of THz spectra only on the sample #1, although it would be more appropriate to seek for the anisotropy of THz permittivity ε_1 in the less conductive sample #2. This time press emerged from the lengthy technical problems that accompanied reconstruction of the THz experimental apparatus. It should be also pointed out that samples #2 and #3 can be considered to be identical within the THz and IR experiments due to their similar conductivity, and therefore experiments in the THz region were performed on sample #2, while in the IR region on sample #3. Moreover, data measured on samples #2 and #3 were not further quantitatively evaluated due to missing magnetic field measurements. Thus, the quantitative analysis was performed on sample #1 only.

The aim of the THz measurement was observation of the permittivity ε_1 (and its possible anisotropy), its extrapolation to low frequencies and the subsequent comparison with the directly measured low-frequency data. To be able to quantitatively evaluate the THz data, i.e. to fit the permittivity ε_1 spectra measured in an external magnetic field and to extrapolate the values of static (low-frequency) permittivity, it is necessary to know the frequencies of phonons that contribute to the permittivity. These frequencies, however, lie in the IR region, which therefore has to be measured. Several mm thick, disc-shaped and optically polished samples were used in all IR experiments (see section Preparation of the samples). Room-temperature IR reflectivity spectrum of $EuTiO_3$ ceramics (sample #3) is shown in Fig. 3.10. In the figure, the frequencies of the transverse ω_{TO_j} and longitudinal ω_{LO_j} modes (as they were determined from the fit of this spectrum) are approximately marked. It is known (see section Electric and magnetic properties), that the frequency of the low-frequency transverse mode ω_{TO_1} (soft mode)

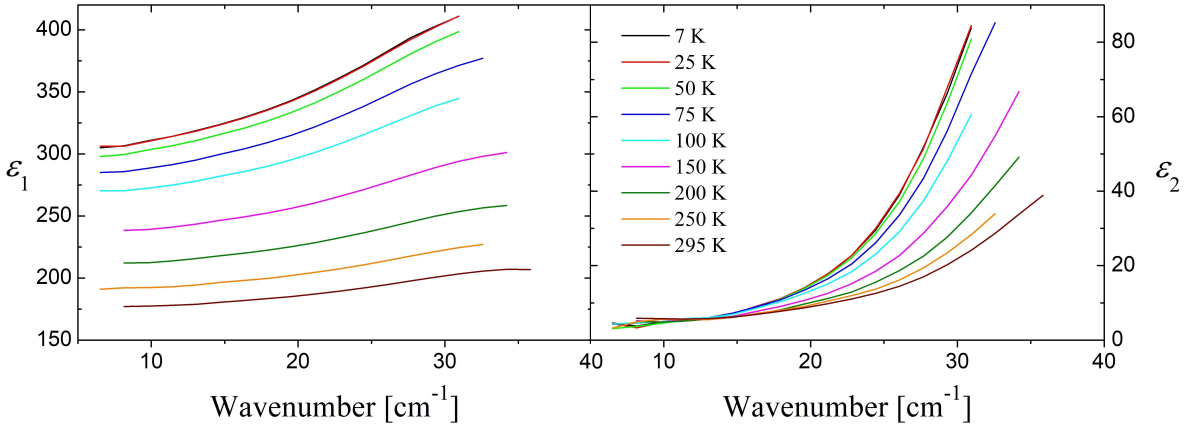

Figure 3.9: THz permittivity spectra of the sample #2 in temperature range 7 – 295 K and zero external magnetic field. **Left:** Real part ε_1 of the complex permittivity. **Right:** Imaginary part ε_2 of the complex permittivity.

actually softens on cooling and splits into two phonons below temperature of the transition from cubic to tetragonal symmetry (i.e. below 282 K). Determination of the detail temperature dependence of the soft mode frequencies was, however, a part of my Bachelor thesis [11] and will not be repeated here.

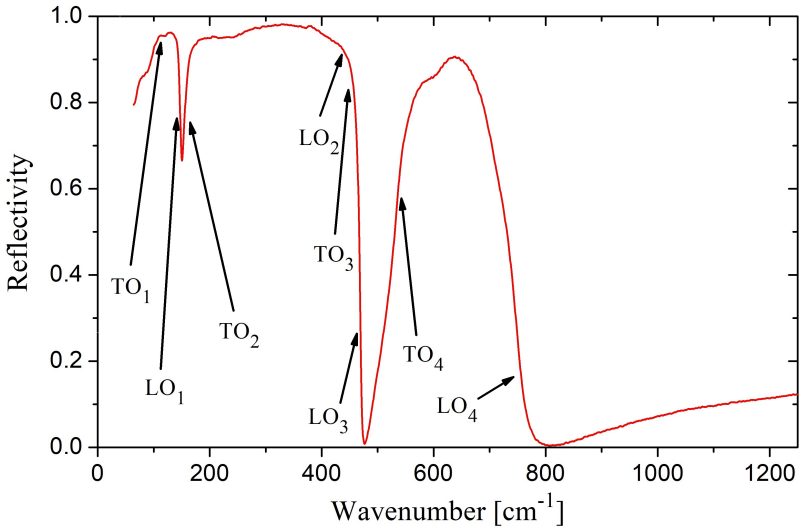

Figure 3.10: The entire IR reflectivity spectrum of the $EuTiO_3$ ceramic sample #3 measured at room temperature. Such a spectra are fitted using the formula (2.11). The four-parameter oscillators' frequencies ω_{TO_j} and ω_{LO_j} are approximately marked by black arrows.

IR reflectivity of samples #1 and #3 was measured at room temperature, 250 K, 200 K, 150 K, 100 K, 75 K, 50 K, 25 K and the lowest achievable temperature. The lowest temperature for samples #1 (7 K) and #3 (12 K) was different due to the leaking windows of the cryostat. The measured and normalized data are summarized in Fig. 3.11. In this figure, only selected spectra, covering approximately uniformly the entire temperature interval, are captured for clarity. There is a noticeable increase in reflectivity on cool-

ing in the frequency range up to about 100 cm^{-1}. The increase is just caused by the softening of the low-frequency TO_1 phonon. Its frequency position is roughly marked by arrow. The noise in the spectra of sample #1 is slightly higher than the spectra of sample #3. This is caused by different polyethylen windows used in the cryostat.

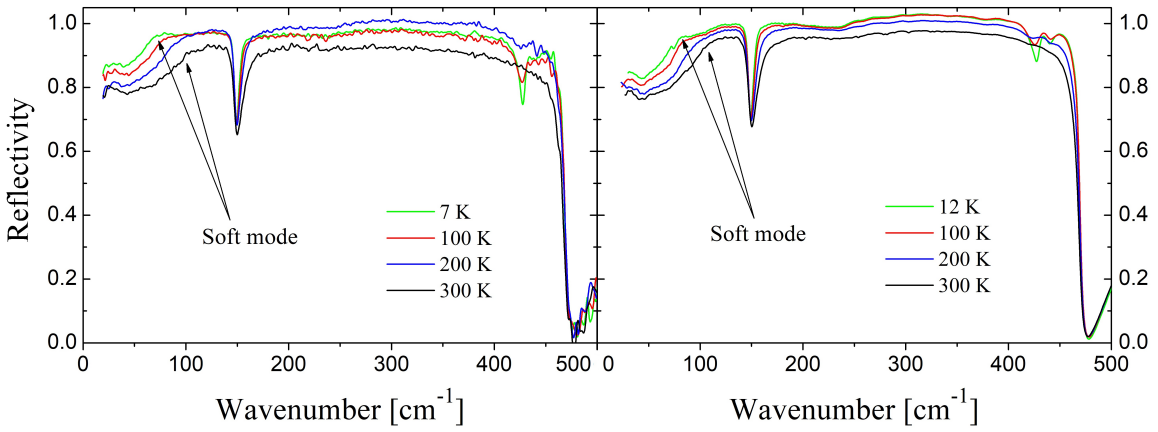

Figure 3.11: **Left:** IR reflectivity spectra of the sample #1 in temperature range 7 – 300 K and zero external magnetic field. **Right:** IR reflectivity spectra of the sample #3 in temperature range 12 – 300 K and zero external magnetic field. The soft mode frequency is approximately marked by black arrows.

Our IR spectrometers measure with deviation approximately up to 5 %. Although the measured spectra have correct trends, the absolute reflectivity value may be influenced by imperfect reference mirror and small misalignment of the sample and reference mirror positions in the cryostat. Small IR sensor in bolometer is extremaly sensitive on small misalignment. To refine the measured IR spectra, the normalization to THz data is used. The normalization is possible, because IR and THz ranges are adjacent to each other and may slightly overlap. From the known courses of THz ε_1 and ε_2 in Fig. 3.8 and 3.9, THz reflectivity is calculated using the formula (2.3) (samples can be considered with good accuracy to be non-magnetic, $\mu_1 = 1$ and $\mu_2 = 0$, in THz region). IR reflectivity is then normalized through a single constant so that the IR spectrum is connected as smoothly as possible to the THz reflectivity spectrum. Still, thus normalized spectra are to some extent burdened with error. This is obvious from the Fig. 3.11 in the frequency range 250 – 400 cm^{-1}, where the reflectivity reaches even unphysical 102 %. However, phonons from this region affect the THz komplex permittivity very little, and therefore it is sufficient to fit the reflectivity in this interval only approximately.

For further investigations of the THz permittivity ε_1 in the magnetic field, it was necessary to analyze only the IR reflectivity spectrum at the lowest temperature. THz measurements with the magnetic field were carried out at 2 K. Such low temperatures are not reachable in cryostat used during IR measurement. Fortunately, the reflectivity of $EuTiO_3$ ceramics varies very little at so low temperatures, so that IR spectrum measured at 7 K can be reliably considered to be identical within the experimental accuracy to the spectrum measured at 2 K. The 7 K reflectivity spectrum was fitted by the curve based on the four parameter model (2.11). The parameters of the fitting curve are listed in the Tab. 3.1. These parameters were then used as the basis for fitting of the THz spectra measured at 2 K and in the presence of an external magnetic field. The parameters of the oscillators 2 – 6 were fixed for these purposes on the values given in the table, as these oscillators contribute very little to the permittivity in the THz region. On the contrary, the transverse mode frequency ω_{TO_1} characterizing the oscillator No. 1 was a free parameter

that allowed the THz spectra fitting.

par. /oscillator No.	1	2	3	4	5	6
ω_{TO} [cm^{-1}]	63	111	153	247	429	539
γ_{TO} [cm^{-1}]	17	99	3,4	135	11	8,4
ω_{LO} [cm^{-1}]	98	149	244	427	471	746
γ_{LO} [cm^{-1}]	89	2,9	141	12	3,1	13

Table 3.1: Fit parameters of the reflectivity spectrum measured at 7 K and $B = 0$ T. The fit is based on the four parameter model of permittivity and is described by the equations 2.2 and 2.11 at $\mu_1 = 1$, $\mu_2 = 0$. The fitting curve consists in total of six four-parameter oscillators, where ω_{TO} and γ_{TO} are frequency and damping of the transverse phonon, ω_{LO} and γ_{LO} are frequency and damping of the longitudinal phonon. The last parameter is high-frequency permittivity $\varepsilon_\infty = 6,1$.

The results of THz measurement of sample #1 in the magnetic field are captured in Fig. 3.12 and 3.13. One should be aware of the fact that there are depicted spectra of the complex refractive index instead of complex permittivity. The reason for this change will be explained in the next paragraph. We can see immediately that the imaginary part n_2 of the refractive index does not show any remarkable dependence with respect to the external magnetic field strength. Slight deviations from a single curve are due to a measurement error that is bigger in the case of n_2 than in the case of a real refractive index n_1. The increase of n_1 with the increasing magnetic field is clearly visible in Fig. 3.12. This behavior is consistent with data of 1 kHz permittivity (see 1.8) since in the first approximation, n_1 depends on ε_1 as $\sqrt{\varepsilon_1}$.

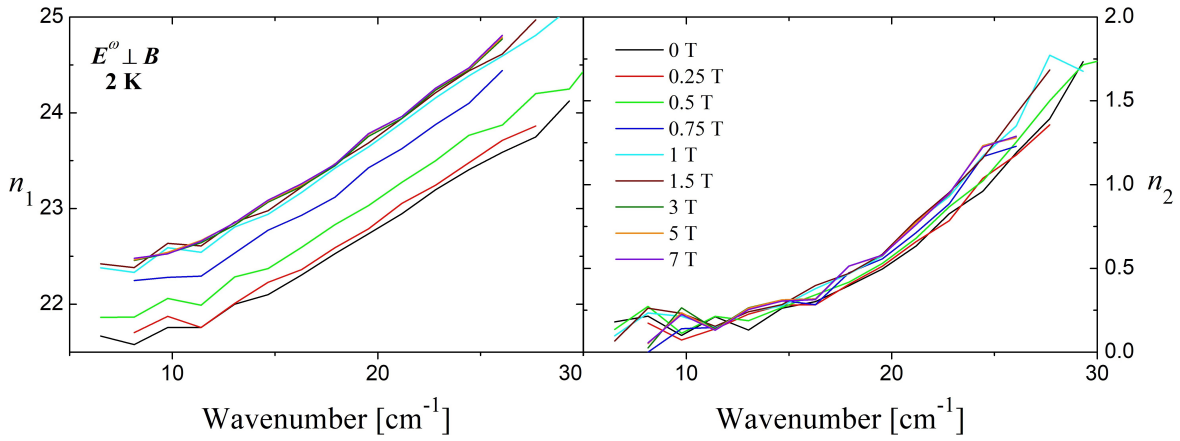

Figure 3.12: THz refractive index spectra of the sample #1 measured at temperature 2 K and in external magnetic field $\boldsymbol{B}$ perpendicular to the THz pulse polarization $\boldsymbol{E}^\omega$. **Left:** Real part n_1 of the complex refractive index. **Right:** Imaginary part n_2 of the complex refractive index.

However, spectra of the real index of refraction n_1 show unexpected course in a magnetic field parallel to the THz pulse polarization (Fig. 3.13). At higher frequencies of the THz interval, n_1 increases quite normally with the magnetic field strength as in the case of perpendicular configuration (Fig. 3.12), but at lower frequencies there is an anomalous decrease of n_1, particularly visible at strong magnetic field. However, this decrease is not a sign of the sought anisotropy of permittivity, but it indicates the presence of resonance, whose frequency approaches the lower border of the measured interval with increasing magnetic field. The strong dependence on the magnetic field and the rather low characteristic

frequency of this resonance, which is around 5 cm^{-1}, reveal that it is not a phonon, whose typical frequencies are above 50 cm^{-1}, but a magnon. The sample is thus significantly magnetically active in the THz region and interacts with the magnetic component of the electromagnetic radiation. Therefore, it is necessary to drop the assumption of a non-magnetic sample ($\mu_1 = 1, \mu_2 = 0$) when the magnetic field is applied. Then, it is not possible to simply calculate the complex permittivity from the measured complex refractive index N, because both the permittivity and the permeability of the material contribute to the N (see equation (1.10)). Therefore, the real and imaginary part of the complex refractive index are shown in Fig. 3.12 and 3.13 instead of the real and imaginary part of the complex permittivity.

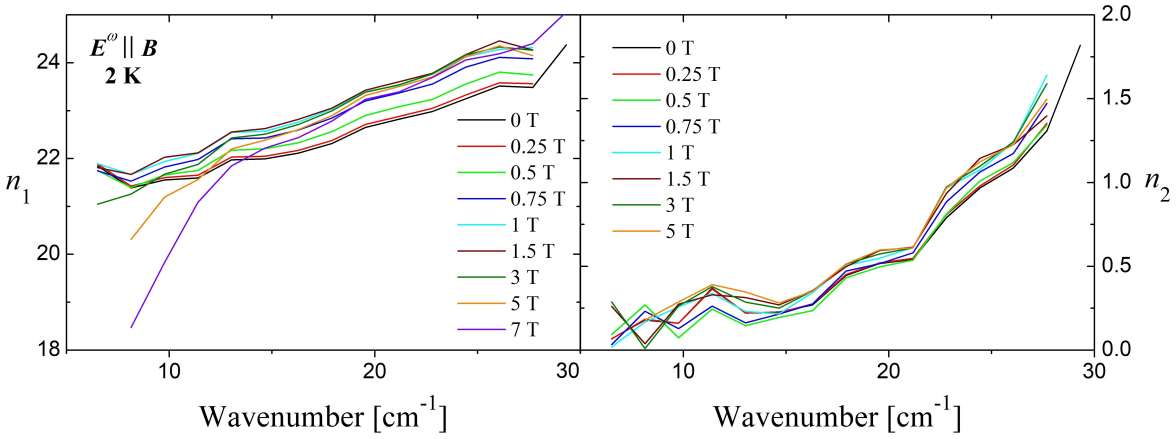

Figure 3.13: THz refractive index spectra of the sample #1 measured at temperature 2 K and in external magnetic field $\boldsymbol{B}$ parallel to the THz pulse polarization $\boldsymbol{E}^{\omega}$. **Left:** Real part n_1 of the complex refractive index. **Right:** Imaginary part n_2 of the complex refractive index.

The selected spectra of n_1 from Fig. 3.12 and 3.13 are shown in Fig. 3.14 for comparison. Magnon is not induced by magnetic field but is an intrinsic property of the material. However, in a weak magnetic field, its characteristic frequency ω_m lies in the microwave region so that the complex refractive index is not affected in the THz region. As the magnetic field is amplified, the magnon frequency ω_m increases (hardens) and the magnon more and more influences the THz spectrum. Let us emphasize, that the magnon contribution to the refractive index n_1 is observed only in external magnetic field $\boldsymbol{B}$ oriented parallel to the electric component $\boldsymbol{E}^{\omega}$ of the linearly polarized THz radiation. This means that the magnon contribution is observed when $\boldsymbol{B}$ and the magnetic component of terahertz radiation are perpendicular to each other. More generally, ω_m is noticeably influenced by $\boldsymbol{B}$ only if there is a nonzero component of the THz radiation magnetic field $\boldsymbol{H}^{\omega}$ which is perpendicular to the $\boldsymbol{B}$. It remains to be noted that the radio-frequency spectroscopy (unlike the THz spectroscopy) measures the permittivity of a magnetic sample directly, so there is no need to deal with magnons in its spectra. It is a consequence of the fact that the radio-frequency experiment determines the capacity of the sample, which is proportional to its permittivity and is not influenced by its magnetic permeability.

Another view of the THz data from Fig. 3.14 provides a graph in Fig. 3.15. This representation is analogous to the right part of the Fig. 1.11. We can see that the influence of magnon truly weakens at higher frequencies of the THz range since the "anisotropy" of refractive index n_1 caused by magnon is less than 2 % at the frequency 24 cm^{-1}. We can judge that if there is no magnon contribution, then no anisotropy in the refractive index n_1 and thus in the permittivity ε_1 is observed. A more precise conclusion can be formulated after the exact fitting of the two components of the complex refractive

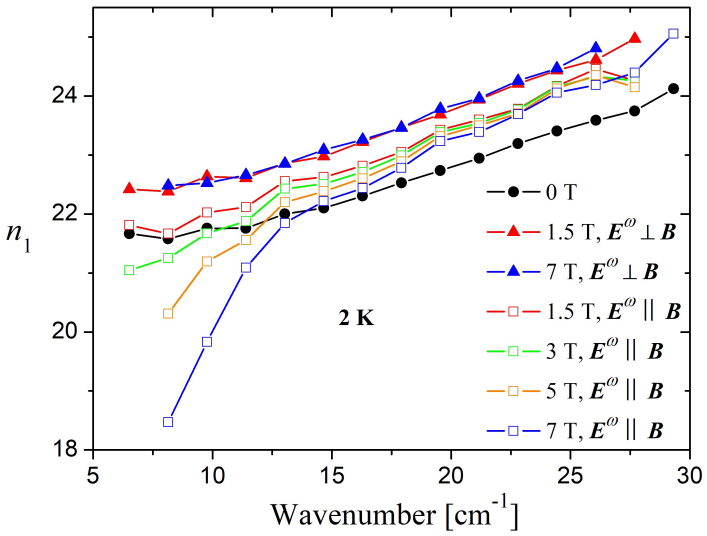

Figure 3.14: THz spectra of the sample #1 real refractive index n_1 measured at temperature 2 K and in external magnetic field $\boldsymbol{B}$ either perpendicular or parallel to the THz pulse polarization $\boldsymbol{E}^\omega$.

index. The procedure is such that the complex permittivity and permeability in relation (1.10) are fitted by oscillator models and thus are separated from each other. The permittivity of the sample in external magnetic field is fitted by the classical four-parameter model (2.11) and the values of the fitting parameters of each curve are always based on the parameters in Tab. 3.1, which were obtained by fitting the reflectivity spectra measured in zero external magnetic field. Since the high-frequency phonons have only very small contribution to THz complex permittivity, it is reasonable to fix the parameters of oscillators No. 2 – 6 for easier fitting.

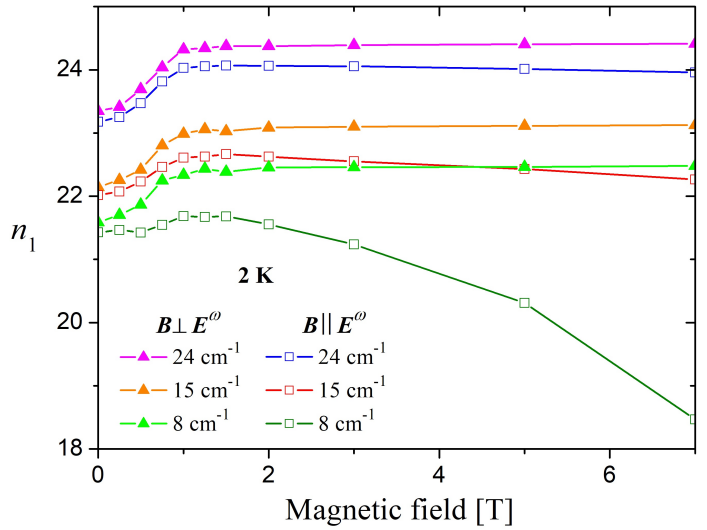

Figure 3.15: Magnetic field $\boldsymbol{B}$ dependences of the real refractive index n_1 in the sample #1 measured at temperature 2 K, for several THz radiation frequencies and in external magnetic field either perpendicular or parallel to the THz pulse polarization $\boldsymbol{E}^\omega$.

In contrast, the complex permeability is fitted with a Lorentz three-parameter model which is analogous to the formula (3.2). Furthermore, we assume that the permeability of the material is influenced only by a single magnon, and thus only one magnetic oscillator describes the THz spectra. This is a reasonable assumption, since the Eu^{2+} ion is the only magnetic moment in $EuTiO_3$. Moreover, its magnetic moments are turned into a ferromagnetic arrangement in the external field. According to the theory (see section Magnons), such a system is characterized by a single magnon branch. Relation expressing the permeability can be thus written in the form

$$\mu(\omega) = \mu_\infty + \frac{\Delta\mu\omega_m^2}{\omega_m^2 - \omega^2 - i\gamma_m\omega}, \tag{3.2}$$

where μ_∞ is temperature-independent high-frequency permeability (in our case equal to 1), $\Delta\mu$ marks magnon contribution to static permeability ($\mu(0) - \mu_\infty$), ω represents frequency, ω_m the magnon frequency and γ_m its damping.

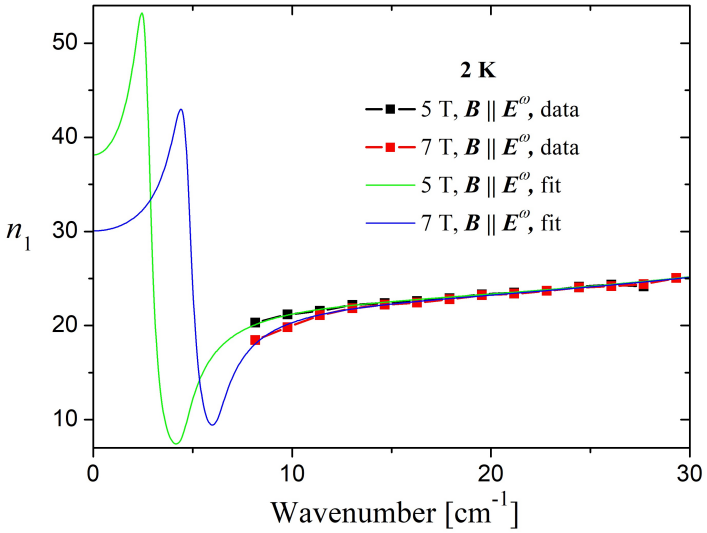

Figure 3.16: Fitted spectra of the sample #1 real refractive index n_1 measured at temperature 2 K and in 5 and 7 T strong magnetic field $\boldsymbol{B}$ oriented in parallel to the THz pulse polarization $\boldsymbol{E}^\omega$.

Using the six phonon oscillators and one magnon oscillator, the complex refractive index spectra measured in the magnetic field of strength 3, 5 and 7 T were fitted. The spectra measured at magnetic fields weaker than 3 T did not show the presence of the magnon (within the measurement error) and phonons were sufficient for the spectra description. The fitting curves and the measured real refractive index data n_1 for magnetic fields 5 and 7 T are depicted in Fig. 3.16. The course of the fit in the displayed frequency domain is primarily defined by magnetic oscillation. One can see that the frequency of the magnon (maximum of the curve) is in the range of cm^{-1} and its frequency actually rises with increasing magnetic field strength. At the same time, $\Delta\mu = \mu(0) - \mu_\infty$ decreases with increasing magnon frequency. In magnetic fields weaker than 3 T, the magnon frequency is so low that the magnon practically does not affect the THz refractive index.

The complex permittivity and permeability of the sample #1 were separated by the fitting of the complex refractive index. By extrapolation from the fitting curve, static permittivity $\varepsilon_1(0)$ values were obtained for both magnetic field orientations with respect to polarization of THz radiation. The results

are summarized in Fig. 3.17. One can see that $\varepsilon_1(0)$ clearly rises up to magnetic field strength of around 1 T, i.e. until the magnetization of the ceramics grows. Steep increase in $\varepsilon_1(0)$ is governed by the soft-mode frequency ω_{TO_1} decrease from original frequency 63 cm^{-1} (in zero external magnetic field) to approximately 60 cm^{-1} (in 1.5 T). Above 1 T, the magnetization saturates (see Fig. 1.12). No indication of anisotropy in the permittivity ε_1 of ceramics #1 is apparent from the data in Fig. 3.17. This result could already have been expected from Fig. 3.14, which indicates that the disproportion in the refractive index between the two significant field orientations is caused by the presence of the magnon only. However, it should be noted that the measurement error of the extrapolated permittivity can be quite large. The simple and very narrow THz frequency spectra of the real n_1 and imaginary n_2 part of complex permittivity are fitted with sofisticated, multi-parameter curves, so there are many similar possibilities to fit these spectra. In order to get accurate fitting curves, it would be necessary to measure much broader frequency spectra. In the best case, broad IR reflectivity spectra of the sample in magnetic field should be measured. However, this is not possible to realize in our IR laboratory. Kamba et al. performed such kind of measurement in High-magnetic field lab in Grenoble, [24] but the measurement was very noisy and did not reveal any expected shift of soft phonon frequency with $\boldsymbol{B}$.

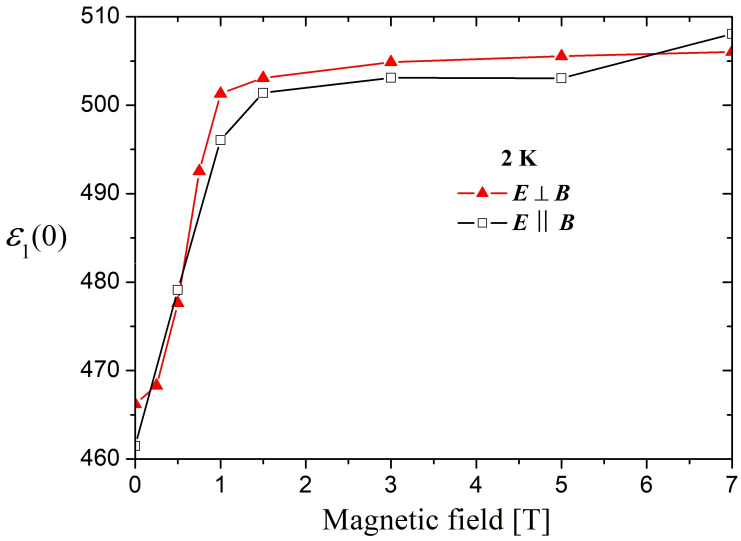

Figure 3.17: Dependence of the calculated static permittivity $\varepsilon_1(0)$ on external magnetic field. $\varepsilon_1(0)$ are extrapolated from the permittivity fitting curves described by six four-parameter oscillators. These fits are based on THz experimental data presented above.

Overall, the anisotropy of permittivity ε_1 of $EuTiO_3$ ceramics in THz region was not observed. All measurements were made on sample #1, which is not the best $EuTiO_3$ ceramics we have (it is more conductive than samples #2 and #3), but is more than sufficient for THz and IR experiments. Nevertheless, the determination of permittivity anisotropy is not affected by the conductivity. The negative result of anisotropy in the THz region supports the the theory of demagnetizing field as an explanation of the possible low-frequency low-field permittivity anisotropy. In fact, the ceramics #1 has an almost circular cross-section and the applied magnetic field together with electric field of the THz radiation always lie in the plane of the disc-shaped sample. The symmetry of the sample then implies that demagnetizing field is the same in both mutual configurations of applied magnetic field and THz electric field (see section Demagnetizing field), and thus the anisotropy of the permittivity (if we assume that it is caused by the demagnetizing field) does not occur in such shaped samples.

3.4 Magnetostrictive measurement

Magnetostrictive measurements were motivated by getting the complete picture of the behaviour of our $EuTiO_3$ ceramics. Although magnetostriction does not cause anisotropy of 1 kHz permittivity, we wanted to build the arguments presented in the section Magnetostriction and Magnetization on our own experimental data. Unfortunately, due to technical reasons, magnetostrictive measurements performed on sample #1 were unreliable. Capacitance dilatometry is an extremely sensitive method that requires precise adjustment and can be fatally affected by even very weak influences of surroundings. During the temperature measurements of magnetostriction, the specimen (a cuboid shape, volume of about 2 mm^3) was displaced in the dilatometric cell and the whole experiment was thereby devalued. Therefore, to illustrate the behaviour of our $EuTiO_3$ ceramics, I present the magnetostrictive data of the older ceramics in the figure 3.18. These data were measured by the collaborators of S. Kamba several years ago, but were not published. [41]

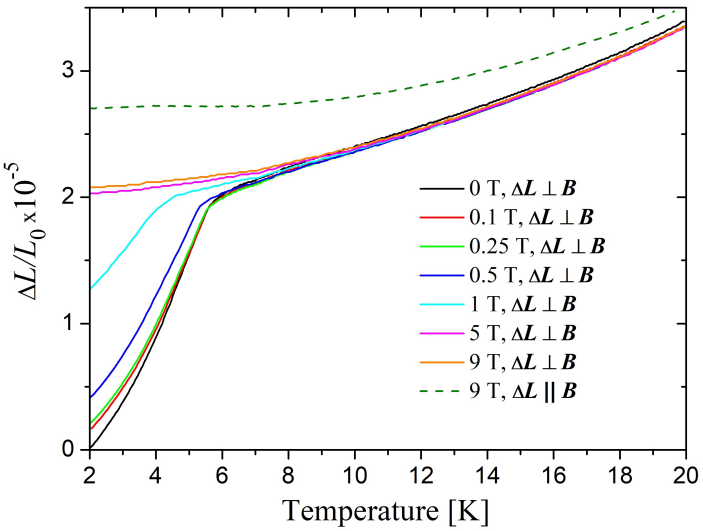

Figure 3.18: Relative change in length $\frac{\Delta L}{L_0}$ of $EuTiO_3$ ceramic sample as a function of temperature and magnetic field B. The change is related to the reference length L_0 measured at 2 K and zero field. The magnetic field was applied in a direction perpendicular and parallel to the measurement direction of $\frac{\Delta L}{L_0}$. The data were measured several years ago by a group around S. Kamba and have not been published yet. [41]

Let us notice a few important things in Fig. 3.18. Firstly, magnetostriction reaches values of the same order of magnitude as in paper [42] (see also Fig. 1.12). Secondly, the data displayed in Fig. 3.18 and 1.12 are qualitatively very similar, but the y-axis scaling in both pictures does not correspond to each other due to the normalization of the measured data to reference lengths obtained at different temperatures. And thirdly, note the curves measured at 9 T. These curves are qualitatively identical but differ quantitatively due to anisotropic magnetostriction (the isotropic contribution is the same for both curves as they were measured in the magnetic field of the same strength).

3.5 Low-frequency permittivity

As it was mentioned in the section 3.1, in all the radio-frequency measurements, approximately 1 mm thick half-disc-shaped samples were used. The golden electric contacts (~ 5 mm diameter) were then deposited on each side of the half-disc. Thus, the sample is considered as a dielectric in the capacitor and the electric field $\boldsymbol{E}^{\omega}$ is always perpendicular to the plane of the half-disc sample (parallel to the short dimension of the sample). For measurement of the radio-frequency permittivity in the magnetic field, the highest quality sample #2 (whose conductivity contribution to the low frequency permittivity is small) was chosen. The magnetic field $\boldsymbol{B}$ was either perpendicular or parallel to the electric field $\boldsymbol{E}^{\omega}$. This means that, unlike the measurements in the THz region, the magnetic field was either parallel or perpendicular to the plane of the half-disc sample.

The measured radio-frequency permittivity as a function of temperature, direction and strength of the external magnetic field and frequency is depicted in Fig. 3.19 and 3.20. We consider the measured data to be very accurate, as all the measurements were carried out on the same sample and without external interference (e.g. during the change of the applied magnetic field orientation). For the sake of clarity, only those measured data, which are relevant for the subsequent discussion, are presented. These graphs are equivalent to those shown in Fig. 1.11. Let us first comment on the data in Fig. 3.19. The captured trends of permittivity are very similar to those on the left side of the Fig. 1.11. Even the absolute change in permittivity with the magnetic field is roughly the same. We can clearly see, that the sample behaves anisotropically with respect to the direction of the external magnetic field $\boldsymbol{B}$ mainly under the antiferromagnetic phase transition (T_N = 5.3 K). Anisotropy grows with increasing $\boldsymbol{B}$ up to 1 T, but with further increase of $\boldsymbol{B}$, the anisotropy gradually disappears. No anisotropy is then observed at 10 T (neither at 5 T). A slight mismatch between the pair of curves represents a measurement error. The relatively high frequency (105 kHz) of the electric field was chosen to minimize the conductivity contribution to dielectric permittivity (see section Electric conductivity).

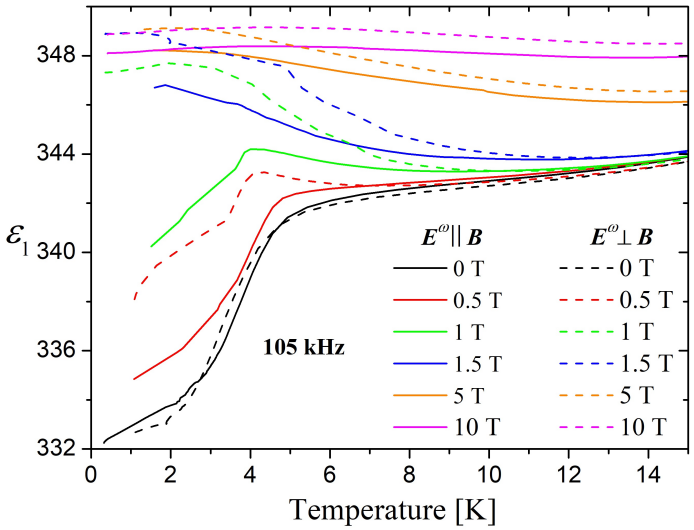

Figure 3.19: Temperature dependence of the dielectric permittivity of the sample #2 in the magnetic field. The spectra were measured in the external magnetic field $\boldsymbol{B}$ applied either perpendicular or parallel to the electric field $\boldsymbol{E}^{\omega}$. Electric field with frequency 105 kHz was always applied perpendicularly to the plane of the half-disc sample.

The low-frequency permittivity anisotropy is also evident from the data in Fig. 3.20. Here, the permittivity was measured for the electric field frequencies 1 Hz, 10 Hz, 100 Hz, 1 kHz, 10 kHz a 100 kHz. Obviously, the permittivity in both magnetic field orientations increases slightly with decreasing frequency. This is probably due to the contribution of the conductivity to the permittivity. A weak noise present in all curves (mainly between 2 T and 4.5 T) is caused by temperature instability in the vicinity of the sample. The temperature more or less oscillated during the whole measurement within the interval 0.3 – 0.4 K. One can conclude that in the magnetic field above 2 T the anisotropy of permittivity is not visible (in contrast to dependences in the right side of the Fig. 1.11). A small difference between red and black curves is probably due to a measurement error. However, the anisotropy is undoubtedly registered in the magnetic field weaker than 2 T. The slope of the permittivity increase is apparently different for both magnetic field orientations. The newly measured data thus refines the ideas based on the data in Fig. 1.11.

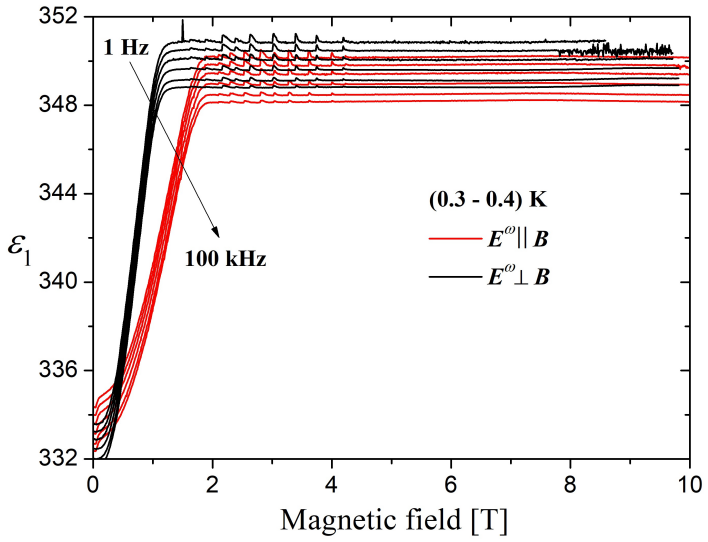

Figure 3.20: Magnetic field dependence of the sample #2 permittivity measured at 1 Hz, 10 Hz, 100 Hz, 1 kHz, 10 kHz and 100 kHz. During the measurement, temperature varied within the interval 0.3 – 0.4 K. Small bumps seen above 2 T are caused by small temperature fluctuations.

The measured data indicates the anisotropy of the permittivity below 2 T caused by the demagnetizing field of the sample, which influences real magnetic field in the sample. 2 T roughly corresponds to the strength of the field in which the magnetization reaches its maximum, respectively slowly saturate itself (see Fig. 1.12). After the magnetization saturation, the spin correlation function reaches its maximum and thus the permittivity is saturated according to equation (1.24). In addition, the strength of the magnetic field required for saturation of the permittivity is different in both directions. According to results captured in Fig. 3.20, the saturation magnetic field is larger in the $\boldsymbol{B}$ direction perpendicular to the sample plane. This exactly corresponds to the prediction given by the demagnetizing field of the sample. If we approximate our half-disc-shaped sample as a very flattened ellipsoid, then we know (see section 1.7) that the elements of demagnetization factor of such a body fulfill $N_x = N_y \doteq 0$ and $N_z \doteq 1$. Thus, the demagnetizing field is unambiguously the largest in the direction perpendicular to the plane of the sample (z direction), and therefore the inner magnetic field of the sample is most weakened for $\boldsymbol{E}^{\omega} \parallel \boldsymbol{B}$. Therefore, the saturation of the sample magnetization (and thus saturation of the permittivity) occurs

at the 50 % higher magnetic field for $\boldsymbol{E}^{\omega} \parallel \boldsymbol{B}$ than for $\boldsymbol{E}^{\omega} \perp \boldsymbol{B}$.

It means, that the anisotropy of permittivity in the weak magnetic fields is only apparent. If we have a sample of irregular shape, then in different orientations of the external magnetic field, the magnetic field strength (and also magnetization) inside the sample may not be the same in all cases. Since the permittivity of $EuTiO_3$ below $T_N = 5.3$ K is strongly dependent on the magnetic field strength inside the sample, it may seem to be anisotropic with respect to the orientation of the external magnetic field. The demagnetizing field as an explanation of the permittivity anisotropy is also supported by the fact that we do not observe anisotropy of a thin disk sample in the THz field. In these experiments, the magnetic field is always applied in the plane of the thin sample, where all the directions are equivalent in terms of the demagnetization factor ($N_x = N_y \doteq 0$).

3.6 Sample magnetization

As it was explained, the probable candidate for explanation of the $EuTiO_3$ ceramics permittivity anisotropy and different critical saturation magnetic field is the phenomenon associated with the shape of the samples themselves. The general principles of the demagnetizing field have already been outlined in the section 1.7. The demagnetizing field is the stronger the higher is sample magnetization (see equation (1.18)). The $EuTiO_3$ ceramics fulfill key requirements needed for the creation of the sufficiently strong (and thus detectable) demagnetizing field. Firstly, Eu^{2+} ions carry an extremely large magnetic moment of 7 μ_B. And secondly, although the AFM arrangement of $EuTiO_3$ under $T_N = 5.3$ K means total zero magnetization, the magnetic moments of Eu^{2+} ions can be oriented more or less parallel already in the external magnetic field around 1 T (see Fig. 1.12).

We wanted to refine the approximate image of the demagnetizing field effect on the permittivity of the $EuTiO_3$ ceramics using the measured data. Therefore we resorted to the measurement of the ceramics magnetization. In order to at least estimate the strength of the demagnetizing field, it was necessary to measure the data on a sample that could be well approximated by a body whose demagnetization factor is analytically countable. Therefore, an elongated cuboid ($1.5 \times 1.5 \times 5$ mm) was cut out of the sample #2 for the purposes of the magnetization experiment. It is then possible to substitute the cuboid with an elongated ellipsoid of revolution (prolate spheroid) with **the long axis in the z direction**. Its demagnetization factors are approximately equal to $N_x = N_y \doteq \frac{1}{2}$ and $N_z \doteq 0$ (see section 1.7).

The measured magnetization data are shown in Fig. 3.21. First, let us note that we do not observe any magnetic hysteresis and, moreover, magnetization depends on the applied magnetic field linearly practically until its saturation. This is usual behaviour of antiferromagnetic materials. It can be seen that the displayed dependencies correspond exactly to the permittivity data shown in Fig. 3.20. The rise of the magnetization in the $\boldsymbol{B} \perp z$ direction is slower (in accordance with theory, where $N_x = N_y \doteq \frac{1}{2}$ and $N_z \doteq 0$) than in the $\boldsymbol{B} \parallel z$ direction since the total magnetic field inside the sample in configuration $\boldsymbol{B} \perp z$ is governed by the equations (1.22). In the $\boldsymbol{B} \parallel z$ direction, no demagnetizing field is created and only the sample permeability determines the magnetic field strength inside the sample.

If the value of saturated magnetization is taken as 0.5 MA/m, then the demagnetizing field calculated from the factor $N_x = N_y \doteq \frac{1}{2}$ is about 0.3 T. This is also the approximate difference of the external magnetic fields $\boldsymbol{B}$ needed for the magnetization saturation in the $\boldsymbol{B} \parallel z$ and $\boldsymbol{B} \perp z$ orientation (see Fig. 3.21). Let us now consider the approximate saturated magnetization value 0.5 MA / m and assume that the magnetization in the sample #2, which we used for the the low-frequency permittivity measurement,

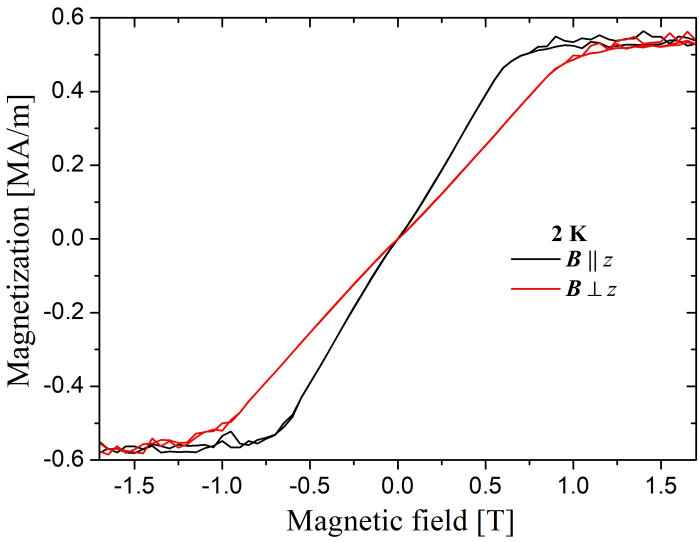

Figure 3.21: Magnetic field dependence of the sample #2 magnetization. The magnetization was measured in the external magnetic field $\boldsymbol{B}$ applied either perpendicular or parallel to the long dimension (z direction) of the elongated cuboid.

is saturated at the same value. This sample can be approximated by a very flattened ellipsoid, which is described by the demagnetization factor $N_x = N_y \doteq 0$ and $N_z \doteq 1$. Therefore, the demagnetizing field is two times stronger in the z direction than in the previous case in the x or y direction. The demagnetizing field of 0.6 T is again in accordance with the experiment in Fig. 3.20. The external magnetic fields needed for permittivity saturation differ between the both field configurations just by this approximate value. This implies the result, that the coarse approximation of our samples using ellipsoids is sufficient to confirm the role of the demagnetizing field of the sample as the cause of the permittivity anisotropy in the weak external magnetic field.

We conclude that the demagnetizing field of the ceramics themselves is the cause of the permittivity anisotropy in the low-frequency data. Firstly, it very well predicts weakening of the magnetic field within the sample oriented perpendicularly to the sample plane. This is evidenced by the calculation of a shift of the magnetic field strength that is needed to saturate the magnetization and thus the permittivity of the sample. Secondly, it explains why anisotropy disappears in strong magnetic fields. This is due to the fact, that from a certain magnetic field strength, the magnetization is saturated independently of the orientation of the applied magnetic field relative to the sample. And thirdly, it is consistent with the isotropy of the ceramics permittivity in the THz experiment. In fact, in this measurement, very thin ceramics (with almost circular cross-section) is always exposed to the external magnetic field lying in its plane. These directions are practically equivalent in terms of the demagnetization factors, and thus the resulting demagnetizing field is almost the same in all these directions within the sample plane.

Conclusion

This Master's degree project deals with a possible permittivity anisotropy of the $EuTiO_3$ ceramics with respect to a mutual orientation of electric and external magnetic field. The first challenge in experiment is the preparation of the $EuTiO_3$ ceramics itself. From the physically-chemical point of view, the proces, that would guarantee the production of high-quality, dense and insulating ceramics, is not known yet. Over the last three years of work, the $EuTiO_3$ ceramics preparation process has been greatly improved. Now we have very dense (significantly over 90 %) ceramics in which an undesirable conductivity has been reduced even by several orders of magnitude. As a result, the spectra of the low-frequency permittivity, which are only little burdened by the conductivity contribution, could be obtained. Despite this significant advancement, the quality of the $EuTiO_3$ ceramics is still very sensitive to every step of the preparation proces. The individual ceramics may thus slightly differ (e.g. in the absolute values of the permittivity spectra), although they were prepared according to an almost identical scenario. At present, we are (mainly due to effort of Dr. M. Kachlík from CEITEC Brno) perhaps close to the maximum quality of the $EuTiO_3$ ceramics. It is true, that they are still more conductive than single crystals, but this is due to the nature of the ceramics themselves as they contain grain boundaries and defects within the individual grains that support the conductivity of the ceramic samples.

In addition to the conductivity of the ceramics, their structure was also examined. Using an optical microscope, the average grain size was estimated to be about 50 μm and the isotropic character of our ceramics (i.e. their non-texturated structure) was confirmed by X-ray diffraction. Thus, the presence of anisotropy as an intrinsic property of the $EuTiO_3$ ceramics could be rejected, and it was clear that the possible anisotropy of the permittivity is actually caused by the application of the external magnetic field. Then we could proceed to the main goals of this work, namely to the observation of the permittivity anisotropy in the terahertz and radio-frequency region and to the subsequent anisotropy justification. In particular, three possible explanations of the permittivity anisotropy with respect to the mutual orientation of the electric and magnetic field have been theoretically investigated. These explanations were sample magnetostriction, morphic effects and the demagnetizing field of the sample.

The permittivity of the $EuTiO_3$ ceramics was experimentally determined by the infrared reflection spectroscopy, terahertz time-domain transmission spectroscopy and the radio-frequency dielectric spectroscopy. The dielectric spectroscopy measurements were performed in frequency range 1 Hz-1 MHz, temperature range $0.3 - 297$ K and in the external static magnetic field up to 15 T (either perpendicular or parallel to the electric field). In the terahertz and infrared region, experiments were performed within the temperature interval $2 - 300$ K and $7 - 300$ K, respectively. In addition, terahertz experiments were also realized in the external magnetic field up to 7 T. This field was also either parallel or perpendicular to the electric component of the linearly polarized terahertz pulse. Furthermore, the magnetostriction of the ceramics (in magnetic field up to 9 T and at low temperatures down to 2 K) was investigated by means of the capacitive dilatometry. Also the magnetization dependence of the cuboid-shaped ce-

ramics on the external magnetic field was determined in two significant directions of the magnetic field considering the dimensions of the cuboid-shaped sample.

Although the temperature dependences of the low-frequency permittivity of the $EuTiO_3$ ceramics (in the external magnetic field) behave similarly to the magnetostrictive dilatation of this ceramics, there is no causality between them. Both quantities depend on the spin correlation function independently. It appears, that the magnetostriction cannot directly influence the radio-frequency permittivity of the $EuTiO_3$ ceramics, since the magnetostriction is three orders of magnitude weaker than the permittivity anisotropy. Similarly, even morphic effects do not cause permittivity anisotropy, as in our experimental arrangement they cannot in principle affect the properties of the isotropic ceramic samples. Significant attention is therefore devoted to the demagnetizing field of our $EuTiO_3$ ceramics.

The measurement results in the THz region revealed an unexpected magnon contribution to the complex refractive index of our ceramics. This contribution was observed only for the external magnetic field parallel to the THz pulse electric field. In order to obtain information about the permittivity of the ceramics from the measured refractive index, it was necessary to fit the measured data with one magnon and six phonon oscillators. The fit revealed the rise of the magnon frequency with increasing external magnetic field strength. After the fitting of all the refractive index spectra we can declare that we do not observe the permittivity anisotropy in the THz range. However, a seemingly negative result supports the theory of the demagnetizing field. In fact, a thin sample of a circular cross section was used for THz experiments and the magnetic field was always applied in the direction lying in the plane of the sample. In terms of the demagnetizing field, these directions are equivalent, so the anisotropy of the permittivity cannot be expected.

Conversely, measurement results of the low-frequency permittivity clearly show the presence of the permittivity anisotropy in magnetic field up to 2 T (above 2 T anisotropy disappears). The magnetic field was applied either in a direction perpendicular or parallel to the half-disc-shaped sample plane. In order to approximately quantify the effect of the demagnetizing field, the magnetization of an enlongated cuboid sample was measured. This time was the magnetic field applied in the perpendicular and parallel direction to the long dimension of the cuboid sample. The magnetization dependences on the external magnetic field coincide with the the low-frequency permittivity dependences. Furthermore, the maximal demagnetizing field of our ceramics was calculated from the measured value of saturated magnetization (the calculation was simplified using analytical results for a very flattened and very elongated ellipsoid). The calculations give surprisingly accurate demagnetizing field strengths for both samples, namely the cuboid one (0.3 T) and the half-disc sample (0.6 T). These numbers correspond to the measured data very well. The demagnetizing field thus reduces the internal magnetic field of the sample when the external magnetic field is applied in short direction of the sample (i.e. for the disc perpedicularly to the sample plane).

All the experimental results (and calculations) mark the demagnetizing field as the cause of the permittivity anisotropy in the external magnetic field up to 2 T. In a number of materials, the demagnetizing field has only weak or even negligible influence. The $EuTiO_3$ is specific due to the large magnetic moments that are carried by Eu^{2+} ions, which are bound by a very weak exchange interaction. Thus, the magnetization of the $EuTiO_3$ ceramics increases sharply in the external magnetic field, resulting in the strong demagnetizing field depending on the sample shape and direction of the sample magnetization. The apparent permittivity anisotropy fades away when the demagnetizing field is overcome by a sufficiently strong external magnetic field.

Bibliography

[1] H. Schmid et al.: Ferroelectrics **162** (1994) 317-338.

[2] M. Fiebig et al.: Nature Reviews Materials **1** (2016) 16046.

[3] T. Katsufuji, H. Takagi: Phys. Rev. B **64** (2001) 054415.

[4] V. V. Shvartsman et al.: Phys. Rev. B **81** (2010) 064426.

[5] Team of authors, editor: É. d. T. d. Lacheisserie: Magnetism I - Fundamentals, University Joseph Fourier, 2002 Edition.

[6] E. Anastassakis, E. Burstein: J. Phys. Chem. Solids **32** (1971) 313-326.

[7] E. Anastassakis, E. Burstein: J. Phys. Chem. Solids **32** (1971) 563-570.

[8] E. Anastassakis, E. Burstein and A. A. Maradudin, R. Minnick: J. Phys. Chem. Solids **33** (1972) 519-531.

[9] E. Anastassakis, E. Burstein and A. A. Maradudin, R. Minnick: J. Phys. Chem. Solids **33** (1972) 1091-1103.

[10] E. Anastassakis, E. Burstein: J. Phys. C: Solid State Phys. **5** (1972) 2468.

[11] D. Repček: Magnetodielectric coupling in $EuTiO_3$, Bachelor's Degree Project, FNSPE CTU, Prague, 2017.

[12] J. Šternberk: Úvod do magnetismu pevných látek, Státní pedagogické nakladatelství, Prague, 1979.

[13] S. Skiadopoulou: Spin and Lattice Excitations in Multiferroics, Doctoral thesis, Institute of Physics of the CAS and Faculty of Mathematics and Physics of the CU, Prague, 2017.

[14] N. A. Spaldin, M. Fiebig: Science **309** (2005) 391-392.

[15] M. Gajek et al.: Nature Materials **6** (2007) 296-302.

[16] A. P. Pyatakov: Physica B: Condensed Matter **542** (2018) 59-62.

[17] D. Khomskii: Physics **2** (2009) 20.

[18] W. Eerenstein, N. D. Mathur & J. F. Scott: Nature **442** (2006) 759-765.

[19] C. Kittel: Úvod do fyziky pevných látek, Academia, Prague, 1985.

[20] D. L. Rousseau et al.: J. Raman Spectr. **10** (1981) 253-290.

[21] P. Brüesch: Phonons, theory and experiments II, Springer-Verlag, New York, 1986.

[22] W. Cochran: Advances in Physics **9** (1960) 387-423.

[23] Z. Bryknar: Fyzika dielektrik, CTU in Prague, 1983.

[24] S. Kamba et al.: EPL **80** (2007) 27002.

[25] T. Holstein, H. Primakoff: Phys. Rev. Lett. **58** (1940) 1098-1113.

[26] J. Vít: Study of multiferroics with hexaferrite crystal structure, Master's Degree Project, FNSPE CTU, Prague, 2015.

[27] G. Schaack: Sol. State Commun. **17** (1975) 505-509.

[28] M. Dressel, G. Grüner: Electrodynamics of Solids, Stuttgart, Los Angeles, 2001.

[29] Bedřich Sedlák, Ivan Štoll: Elektřina a magnetismus, Karolinum, Prague, 2012.

[30] Wikipedia.org, cited 18. 7. 2018, available online. https://en.wikipedia.org/wiki/Perovskite_(structure)

[31] I. Kraus: Struktura a vlastnosti krystalů, Academia, Prague, 1993.

[32] K. A. Müller, H. Burkard: Phys. Rev. B **19** (1979) 3593-3602.

[33] J. Brous, I. Fankuchen, E. Banks: Acta Cryst. **6** (1953) 67-70.

[34] A. Bussmann-Holder, J. Köhler, R. K. Kremer, J. M. Law: Phys. Rev. B **83** (2011) 212102.

[35] J. Köhler et al.: Phase Transitions **85** (2012) 949-955.

[36] V. Goian et al.: Phys. Rev. B **86** (2012) 054112.

[37] A. M. Glazer: Phase Transitions **84** (2011) 405-420.

[38] N. Setter: Ferroelectrics **500** (2016) 164-182.

[39] T. R. McGuire et al.: J. Appl. Phys. **37** (1966) 981-982.

[40] S. Kamba et al.: Phys. Rev. B **85** (2012) 094435.

[41] S. Kamba: private communication.

[42] P. G. Reuvekamp, R. K. Kremer, J. Köhler, A. Bussmann-Holder: Phys. Rev. B **90** (2014) 094420.

[43] A. A. Mukhin, A. Yu. Pronin et al.: Phys. lett. A **153** (1991) 499-504.

[44] P. R. Griffiths, J. A. de Haseth: Fourier Transform Infrared Spectrometry, Hoboken, New Jersey, 2007.

[45] Sparknotes.com, cited 18. 7. 2018, available online. http://www.sparknotes.com/physics/optics/phenom/section1.rhtml

[46] Institut für Physik, Universität Augsburg, cited 18. 7. 2018, available online. http://www-4.physik.uni-augsburg.de/exp5/research/ftir.shtml.en

[47] P. Kužel, H. Němec, F. Kadlec, and C. Kadlec: Optics Express **15** (2010) 15338.

[48] J. Petzelt, P. Kužel et al.: Ferroelectrics **288** (2003) 169-185.

[49] V. Skoromets, C. Kadlec, H. Němec, D. Fattakhova-Rohlfing, P. Kužel: J. Phys. D: Appl. Phys. **49** (2016) 065306.

[50] R. P. Lowndes: Phys. Rev. B **1** (1970) 2754-2763.

[51] E.D. Palik, E.J. Prucha: Handbook of optical constants of solids, p. 35, Academic Press, Boston, MA, 1997.

[52] F. Wooten: Optical properties of solids, Academic Press, New York, 1972.

[53] Cryogenic, cited 27. 4. 2019, available online. `http://www.cryogenic.co.uk/products`

[54] I. Kraus, H. Frank, I. Kratochvílová: Úvod do fyziky pevných látek, CTU press, Prague, 2009.

[55] J. Prokleška: Cohesive and magnetoelastic properties of materials with strongly correlated electrons, Doctoral thesis, Faculty of Mathematics and Physics of the CU, Prague, 2008.

[56] Quantum Design, cited 26. 3. 2019, available online. `https://www.qdusa.com/products/ppms.html`

[57] M. Kachlík et al.: Material Letters **74** (2012) 16-18.

[58] V. Valvoda, M. Järvinen: Powder Diffraction **4** (1990) 200-203.

[59] D. A. Crandles et al.: Journal of Applied Physics **119** (2016) 154105.

[60] P. Lunkenheimer, S. Krohns, S. Riegg, S. G. Ebbinghaus, A. Reller, A. Loidl: Eur. Phys. J. Special Topics **180** (2010) 61-89.